2013

Assessing Variability in Microstructural Influence on Fatigue Crack Growth Behavior

Matthew James Durbin
Purdue University, matthew.durbin1@gmail.com

PURDUE UNIVERSITY
GRADUATE SCHOOL
Thesis/Dissertation Acceptance

This is to certify that the thesis/dissertation prepared

By Matthew James Durbin

Entitled

Assessing Variability in Microstructural Influence on Fatigue Crack Growth Behavior

For the degree of Master of Science in Aeronautics and Astronautics

Is approved by the final examining committee:

Prof. Michael Sangid
Chair

Prof. Alten Grandt

Prof. Weinong Chen

To the best of my knowledge and as understood by the student in the *Research Integrity and Copyright Disclaimer (Graduate School Form 20)*, this thesis/dissertation adheres to the provisions of Purdue University's "Policy on Integrity in Research" and the use of copyrighted material.

Approved by Major Professor(s): Prof. Michael Sangid

Approved by: Prof. Weinong Chen 11/22/2013
Head of the Graduate Program Date

ASSESSING VARIABILITY IN MICROSTRUCTURAL INFLUENCE OF FATIGUE CRACK GROWTH BEHAVIOR

A Thesis
Submitted to the Faculty
of
Purdue University
by
Matthew Durbin

In Partial Fulfillment of the
Requirements for the Degree
of
Masters of Science in Aeronautics and Astronautics

December 2013
Purdue University
West Lafayette, Indiana

ACKNOWLEDGEMENTS

It is only through the help of numerous individuals that this research and report has come to fruition. Firstly thanks to Dr. Kevin Walker, the second Royal Australian Air Force (RAAF) member to take part in the MSAAE program at Purdue University, not only for the challenge of this project and the supply of specimens, but his mentorship along the long road of becoming somewhat competent in the field of fatigue testing.

Secondly I must thank my Major Professor Dr. Michael Sangid for accepting me into his lab and providing this invaluable opportunity to learn and broaden my knowledge and experience in an ever-changing field. Professor's A.F. Grandt and J.C. Newman Jr also helped steer me in the right direction more than once with their wealth of experience, for that I am grateful.

Thanks must also go Mr. Dave Reagan of the AAE School, Mr. Rich Anderson of MTS and Mr. Randy Repogle of the Chemistry Machine Shop. With out the help, guidance, patience and professionalism of these people, this project would never have started. The members of the AAE Fatigue Lab (Javier Esquivel, Tony Favaloro, Megan Kinney, Saikumar Reddy and Andrea Rovinelli) must also be thanked for their help and as valuable sounding boards and muscle to get the project going.

A special mention must also go to the members of the US Coast Guard, US Army and the RAAF, Ashlie Christian, Troy Glendye, Hans Goverston, Jeff Graham, Chris Kourloufas, Mark Potoshnick, Ben Schluckbier, Todd Troup and Liam Weibler for their support during the trials and tribulations of the return to full time studies.

TABLE OF CONTENTS

Page

Page

Page

Page

LIST OF FIGURES

Figure Page

Figure Page

Figure Page

LIST OF TABLES

NOMENCLATURE

Noted in order of appearance in text.

DIC – Digital Image Correlation

EBSD – Electron Back Scatter Diffraction

SIF – Stress Intensity Factor

β – SIF Geometric Correction Factor

σ - Applied stress (in various forms, yield, ultimate etc)

a - Crack Length

ΔK – SIF range between P_{max} and P_{min} i.e. $K_{max} - K_{min}$

da/dN - Crack growth rate

C – Material constant from Paris' Law

m – Loading constant from Paris' Law

ΔK_{th} - Fatigue threshold value, below this SIF crack growth is assumed to be zero

K_{max} – SIF at P_{max}

K_{min} - SIF at P_{min}

LR – Load Reduction

R – Load Ratio

ΔK_{eff} - SIF range that has allowed for closure effects

K_{open} - SIF at P_{open} determined using compliance calculations

BFS – Back Face Strain

ESE(T) – Eccentrically Loaded Single Edge Tension

CPCA – Compression Pre-Cracking Constant Amplitude

CPLR – Compression Pre-Cracking Load Reduction

K_{cp} - SIF for compression loading case

E – Elastic Modulus

B - Thickness

W - Width

G – Effect of crack length in ESE(T) SIF calculations

P - Load

α - Normalized crack length i.e. crack length divided by specimen width

$k_0\ etc$ - Coefficients used for the calculation of ESE(T) SIF

P_{min} – Minimum Load

P_{max} - Maximum Load

Δa – Change in crack length

ρ_{cp} – Flow Stress (average of yield stress and ultimate tensile strength)

h_n - Notch height

$A_0\ etc$ - Coefficients used for the calculation of ESE(T) crack length

U – Strain/Compliance correction

A^* - Normalized Strain

ε - Applied strain

ABSTRACT

Durbin, Matthew J. M.S.A.A.E, Purdue University, December 2013. Assessing Variability in Microstructural Influence of Fatigue Crack Growth Behavor. Major Professor: Dr. Michael Sangid

The effect of microstructural variability has long been recognized as a major contributing factor in the scatter of published fatigue data. It is also acknowledged that these effects are generally more prevalent for short cracks and in the threshold region. A number of models exist to explain individual microstructural effects such as grain boundary influence, grain cluster, average grain size, porosity etc. It is the aim of the Aeronautics and Astronautics Fatigue Lab to develop an encompassing model that accurately predicts these effects.

In order to develop this model a range of material data will be required to inform and validate the model simulation. It is the aim of this thesis to develop the methods required to generate suitable fatigue crack data and also image the crack propagation and strain fields.

The methodology from ASTM E647 was used for the determination of crack growth data with the notable exception of the use of compression pre-cracking and relevant crack growth models for the ESE(T) specimen. Compression pre-cracking methods have been utilised as data have shown that standard pre-cracking methods may affect crack growth rate data and the determination of threshold values. High and low load ratio tests were conducted with closure accounted for, allowing for accurate determination of the fatigue crack growth threshold.

High resolution DIC imagery was captured for a range of loads over a range of crack lengths and enabled the visualization of material strain fields. The imagery also allowed correlation between fatigue crack growth variability, closure data and the tortuosity of the crack surface.

CHAPTER 1. INTRODUCTION

Metal fatigue has long been recognized as a phenomenon worthy of study, the first recorded investigations into failed mining equipment being published in the late 1830's [1]. Some 30 years later, Wöhler is attributed with making strides in the field, discussing and quantifying many basic concepts and developing basic design strategies to avoid fatigue [2]. Decades on, in 1903 Ewing and Humfrey made the fundamental discovery that fatigue nuclei start as micro-cracks in slip bands, still it wasn't until the second half of the 20th century that with the availability of increasing technology would research in the field explode [3].

Over the decades, despite the major contributions to the field by the likes or Paris, Irwin, Elber, Suresh, Pippan, Ritchie, Newman etc, research continues in earnest. The primary reason is, that despite our best efforts fatigue failures continue to contribute to an estimated 50% of engineering failures, equating to an estimated cost of 4% of the US GDP [4].

As our understanding of fatigue mechanisms has developed, the approach to component/structural design has changed considerably. The first and most rudimentary approach of designing against fatigue was what is often termed infinite life [5]. The method here was to simply ensure that the endurance limit (stress level under which cracks will not form/propagate) of the component/structure was never exceeded. The next approach to emerge was Safe-Life. The basis of this method is that the structure/component is given a safe-life in which fatigue failure should not to occur. This safe life is determined through extensive fatigue tests and applications of factors of safety. Despite this seemingly conservative approach there have been several infamous failures of components and structures utilising the safe life approach.

Born of these failures is what is now termed the damage tolerant approach to design, and has been used by the US Air Force since the 1970's [6]. This approach is a much more comprehensive and incorporates factors such as sources of initial damage, microstructural effects and residual strength, combined with extensive testing and increasingly, computer modeling. The development of these approaches has ultimately led to more effective design. In order to continue this trend of effective design, further understanding of the mechanisms of fatigue is required.

The life of a crack is generally divided into two phases, nucleation and propagation. It is also understood that, for nearly all engineering materials, a vast majority of the life of the crack is spent in the nucleation phase, especially when subjected to relatively low levels of stress. As a result of this simple fact, a large volume of research has been devoted to understanding the mechanics of crack nucleation and small crack propagation.

Inherent to all engineering materials are dislocations, or flaws, in the crystal structure of a material. These dislocations are generally responsible for many observable material properties. If a component were to remain unloaded there would be no dislocation movement. However, during the course of repeated loading and unloading cycles, these dislocations become mobile, multiply and accumulate [7]. This results in localized areas of high strain, leading to formation of slip bands, see Figure 1. As more and more cycles are accumulated, these slip bands widen and some eventually develop into small cracks [8].

Figure 1. Formation of slip bands in steel as captured by Ewing and Humfrey in 1903 [8].

The next consideration in crack growth analysis is the effect of the material microstructure. As discussed, fatigue cracks begin their life as slip bands in a single grain of the material. In this single grain, the slip band occurs in the most favorable slip system. The propagation of this slip band from one grain to the next is dependent upon there being another favorably orientated grain through which to propagate [9]. Of course grain orientation is a significant factor but other microstructural features such as inclusions, porosity, notches, grain clusters/neighbors, grain boundaries and average grain size can all contribute to the propagation of these small cracks.

With so many possible contributing factors, most research has sought to isolate, identify and characterize a single factor. As such there are myriad of models attempting to describe small crack growth. Most recently it is the aim of the Purdue Aeronautics and Astronautics Fatigue Lab to develop a new encompassing model utilising the crystal plasticity approach [10]. It is envisioned that the development of this model and verification with material testing data will provide an increased understanding of small crack growth and microstructural effects. With this information it is believed possible that some of the scatter so evident in fatigue results will be explained.

The key to the development and verification of such a model is the generation of sufficient material testing data with which to compare. As we have seen in previous discussion, fatigue, particularly at short crack lengths, is characterized by local build up of strain [11]. By visualizing this strain it will be possible to gain an understanding of how microstructural effects influence crack growth.

The visualization of this strain can be accomplished with the use of a recently developed technique termed Direct Image Correction (DIC). This is a revolutionary technique that enables full field strain measurements to be taken. Electron Back Scatter Diffraction (EBSD) can also be utilized to measure the spatial lattice orientations, which provides the grain structure of the material. Using a combination of DIC and EBSD the strain fields can be mapped to the microstructure.

In order to create the strain field, some cyclic load will need to be applied. Basic fatigue tests as outlined in ASTM E647 [12] provide the necessary guidance. The tests are generally broken into two phases (which are independent of each other), threshold testing

and steady state constant amplitude loading. The steady state constant amplitude testing is applicable to longer cracks and crack growth rates above 3.937×10^{-7} in/cycle [12]. Threshold testing is generally more applicable to the shorter cracks and for crack growth rates below 3.937×10^{-7} in/cycle [12].

The threshold test is used to determine the stress intensity factor below which crack extension will not occur. Although the threshold is arbitrarily defined as 3.937×10^{-9} in/cycle in ASTM E647 [12], it has been shown, most famously Pearson [13], that cracks can still propagate below this level. Small cracks in particular are observed to propagate at rates much faster than would be expected. This is generally attributed to a much higher local stress intensity factor due to the geometry of small cracks. The determination of a material fatigue threshold is essential for characterizing crack growth and also understanding microstructural effects.

Recently however, it has been shown that the procedures outlined in ASTM E647 for the determination of a material threshold may produce artificially high thresholds [14]. The basic mechanism often attributed to this phenomenon is load history. To save time when conducting fatigue experiments, samples are pre-cracked. The pre-cracking stage (completed in tension-tension loading in accordance with ASTM E647) induces a plastically affected zone in the material, which in turn affects the crack growth rate and may produce a higher threshold.

Experiments in the last two decades have shown that pre-cracking in compression-compression loading, may produce more realistic thresholds [14]. Application of cyclic loads will create a series of plastically affect zones as the crack propagates. This plastic zone may have an effect on crack growth. It is impossible to avoid this plastic zone as it small scale plastic yielding that is responsible for fatigue cracking. It is possible however to minimize the effects. The first cycle of compression-compression pre-cracking will induce a plastically affected zone. However, as the compression-compression cycles continue, the plastically affected zone becomes smaller and smaller up until a point where the crack arrests. That is, the magnitude of the load is insufficient to plastically yield material at the crack tip and crack growth ceases.

This method creates a much smaller plastically affected zone, which in turn reduces the effect of load history on subsequent testing. In some materials this compression-compression pre-cracking procedure has been shown to produce fatigue thresholds significantly lower than previously obtained. Although load history effects will never be able to be completed removed in testing, the compression pre-cracking method is believed to provide the best estimate of a “pristine” material.

It is a combination of these approaches, EBSD, DIC and compression-compression threshold testing that will allow the full characterization of the material microstructure and subsequent fatigue crack growth under cyclic loading.

It is the aim of this research to provide the initial set up, prove the feasibility of such a project, and if possible provide data for the ongoing development of the material microstructure based model.

CHAPTER 2. LITERATURE REVIEW

2.1 Fatigue Crack Growth

The most simplistic approach to fatigue crack growth and linear elastic fracture mechanics (LEFM) requires an understanding of the concept of the stress intensity factor (SIF). The current approach to the SIF is commonly attributed to Irwin [15], who expanded Griffith's [16] work on brittle materials (specifically glass) to incorporate ductile materials. This enabled a way in which the severity of the stress distribution around a crack tip could be determined [17].

A crack tip can be subjected to three basic loading types or modes, see Figure 2, each resulting in a different derivation of the SIF. Mode I (tensile opening) is the most frequent type of failure that engineers encounter and design against, it is also the mode for which the most data is available [19]. This research, testing will be confined to Mode I loading. In this type of loading the SIF relates remote load, crack size and component/structural geometry, and is commonly expressed in the following form:

$$K = \sigma\sqrt{\pi a}\beta \tag{1}$$

where σ is the applied stress, a is the crack length and β is a dimensionless factor that accounts for crack length and component geometry [5].

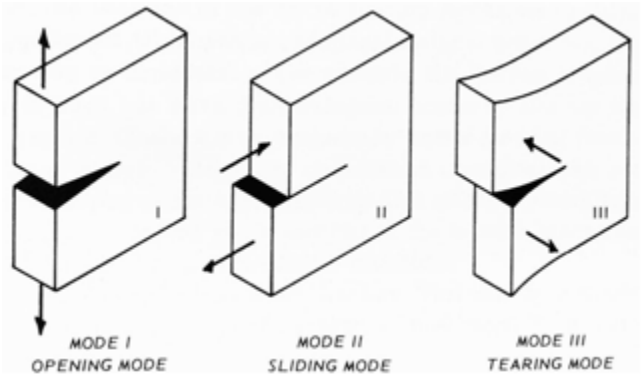

Figure 2. Modes of loading used for the derivation of the stress intensity factor [19].

In using the SIF and LEFM to describe fatigue crack growth, the following basic relationship is known.

$$\frac{\Delta a}{\Delta N} = f(\Delta K) \tag{2}$$

Where $\Delta a/\Delta N$ is the crack growth rate and ΔK is the stress intensity factor range. Paris and Erdogan [20] further defined this relationship and created what is now commonly termed Paris' Law.

$$\frac{da}{dN} = C(\Delta K)^m \tag{3}$$

Where C and m are material and loading constants. McEvily and Boettner [21] subsequently conducted a large number of experiments, thereby validating the relationship.

At this point it is relevant to briefly mention the concept of similitude, which forms the basis of the Paris' Law and related equations. This concept implies that, for two cracks of different sizes subjected to the same stress intensity (under small scale yielding) in a given material-microstructure-environment system, crack tip plastic zones are equal in size and the stress and strain distributions along the borders of these zones (ahead of the crack) are identical [22]. That is regardless of crack length, for a similar SIF, in the same

material we should expect a similar rate of crack growth rate. This can be seen in the Irwin description of plastic zone size [5].

$$r_p = \frac{1}{2\pi}\left(\frac{K_I}{\sigma_{Yield}}\right)^2 \quad (4)$$

Where r_p is the plastic zone radius, K_I is the stress intensity factor for Mode I loading and σ_{Yield} is the material yield stress. In Equation 4 we can see that the plastic zone size is dependent upon the SIF only, this concept is shown in Figure 3. It is also interesting to note that it is the concept of similitude that allows laboratory data (often obtained on small test specimens), to be transferred to real world components and loading situations with reasonable accuracy [4].

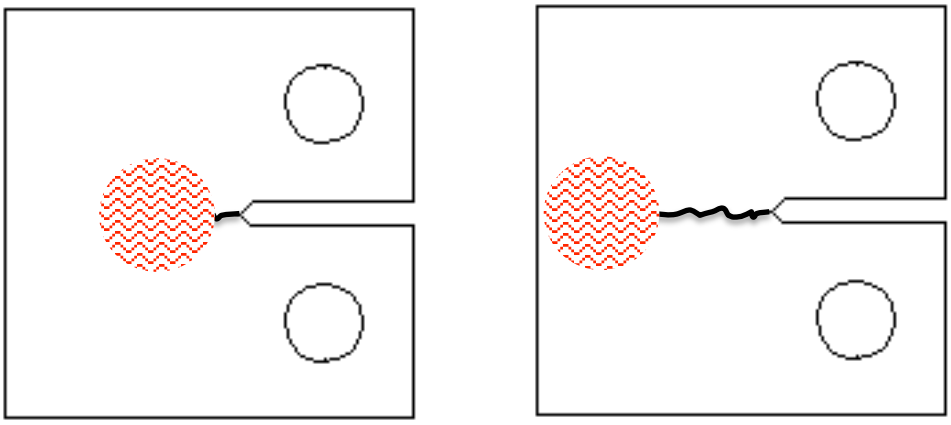

Figure 3. Illustration of the similitude concept, despite having different crack lengths, if the SIF is the same, we expect a similar size plastic zone (red hatched area) and hence a similar crack growth rate.

Paris' Law was revolutionary, as only a single fatigue crack test needs to be performed in order to determine the values of C and m. With this information it is then possible to determine the crack growth rate at any other SIF [1].

Although Paris' Law provided an easy way to correlate crack growth data, the ability to totally describe fatigue crack growth is limited. In its rather simplistic form, Paris' Law does not encompass the influence of mean stress, closure and threshold effects. This

however has not stopped its adoption the world over as a valuable means with which to describe crack growth.

When plotted on a log-log scale for any arbitrary material, the fatigue crack data, da/dN vs ΔK, takes on the characteristic form shown in Figure 4.

The data can generally be divided into three distinct regions as labeled. The limitation of Paris' Law is that it only adequately describes the center, linear portion of the curve (often termed the Paris Region). In this region the crack growth rate is fairly linear and stable and is thus relatively easy to model. The relationship breaks down in the non-linear areas of the curve at the crack growth threshold and in the fracture region. In these remaining two regions crack growth is generally faster, but also much more variable, due in part to microstructural features.

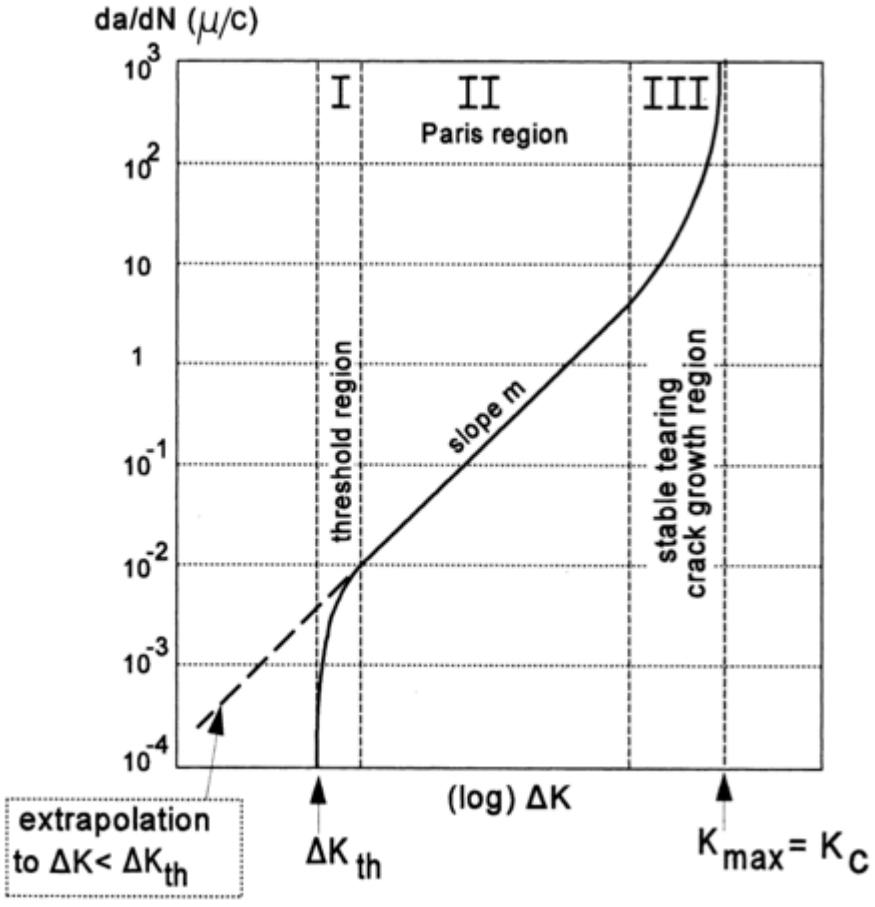

Figure 4. Representative da/dN vs $\boldsymbol{\Delta K}$ curve detailing three regions of crack growth [17].

The threshold region has been extensively studied particularly since the material spends a majority of its fatigue life in this region. This research will focus on the threshold regime since the variability of the material microstructure will have the most effect in this region. The threshold portion, and the remainder of the da/dN vs ΔK curve, is obtained through fatigue testing. This fatigue testing is largely governed by ASTM E647 [12], which provides recommendations and guidelines for all types of testing.

For threshold determination, ASTM E647 details two methods for threshold determination, ΔK-decreasing and constant-K_{max}. The constant-K_{max} procedure imposes a constant K_{max} and incrementally increases K_{min}. This method is not with out it flaws however, and is suited to high load ratio, R, situations [12]. For a majority of threshold testing the ASTM recommends the ΔK-decreasing (Load Reduction (LR)) method. This method sheds loads incrementally according to the following equation.

$$\Delta K = \Delta K_0 e^{C(a-a_0)} \tag{5}$$

Where ΔK_0 is the initial ΔK at the start of the test, a_0 is the corresponding crack size and C is the normalized K-gradient [12]. As loads are shed, ΔK reduces and a corresponding reduction in da/dN is achieved. Figure 5 shows the process of load shedding and reduction in ΔK of a typical LR test.

Once the threshold of the material in question has been determined the remainder of the curve can be determined in accordance with ASTM E647 using a Constant-Force-Amplitude test.

The description of fatigue crack growth determination and data above is rather simplistic. Whilst it can provide useful data for design, a more thorough understanding of crack growth mechanisms affecting this data is required for efficient design.

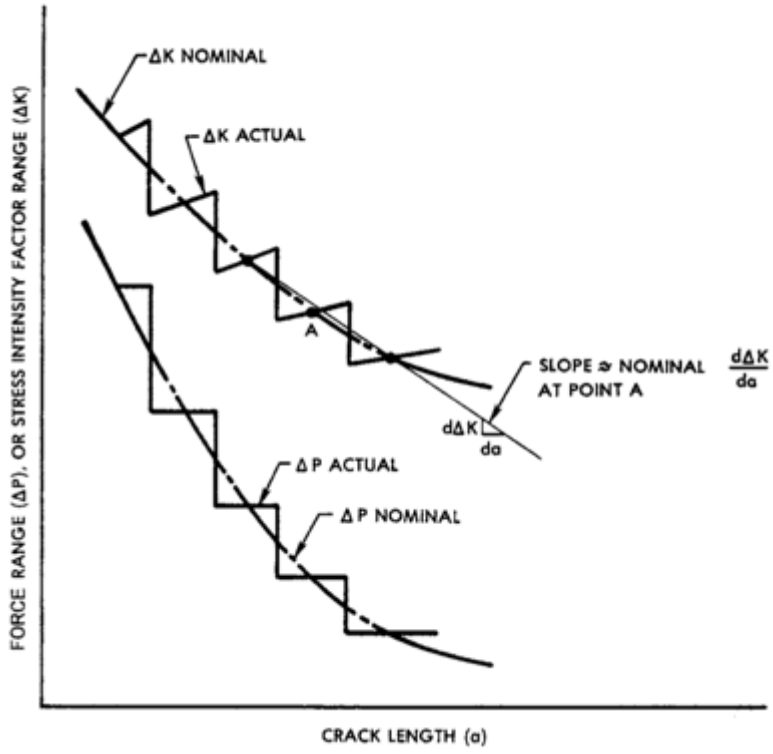

Figure 5. Typical load reduction test step-down procedure [12].

2.2 Load Ratio and Crack Closure Effects

The Load Ratio, R, defined as the ratio between the minimum and maximum load, has long been known to have a significant effect on the da/dN vs ΔK curve. As the load ratio increases, the mean stress increases which leads to a higher crack growth rate at the same stress intensity of a lower load ratio. Figure 6 contains experimental data showing this effect.

Many attempts have been made to incorporate the effects of load ratio into Paris' Law, so much so that many texts will feature Equation 2 in the form shown in Equation 6.

$$\frac{da}{dN} = f(\Delta K, R) \tag{6}$$

Of the more famous attempts to incorporate load ratio into Paris' Law are Walker's [24] formula which accounts for load ratio in the Paris region.

$$\frac{da}{dN} = C[(1-R)^m K_{max}]^P \tag{7}$$

Where C, p and m are obtained through experimental design. Forman's [25] accounts for load ratio in the Paris and Fracture regions.

$$\frac{da}{dN} = \frac{c(\Delta K)^n}{(1-R)K_c - \Delta K} \tag{8}$$

Where c and n can be obtained through experimental data. Using either of these approaches enables the "collapse" of the various load ratio data into a single da/dN vs ΔK curve.

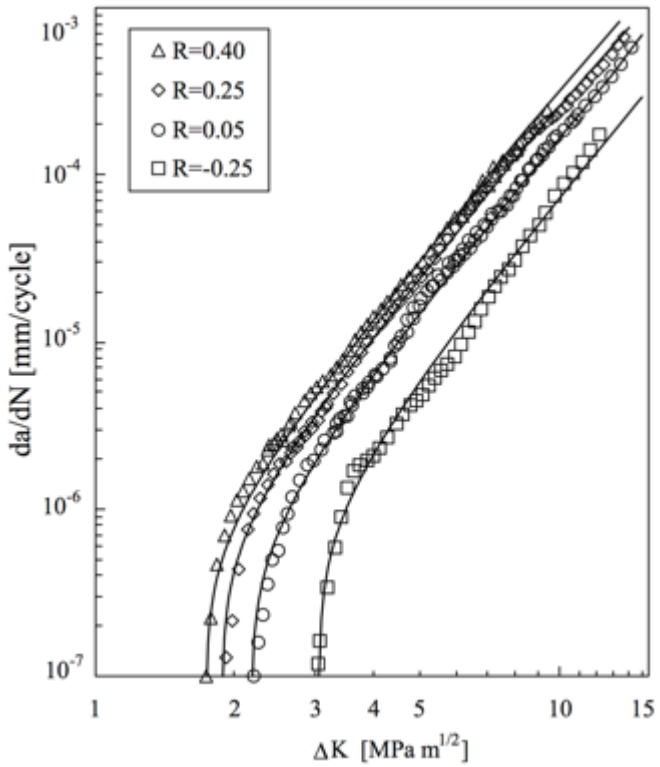

Figure 6. The effect of increasing load ratio on fatigue crack growth rate. As the load ratio increases the fatigue crack growth curve shifts to the left [25].

In the early 1960's and into the 1970's Elber [26] [27] discovered, and conducted a number of experiments to quantify, what is now known as crack closure. Prior to this time it was assumed that at zero load, any given crack was closed and that under the application of a tensile load the crack would fully open. Elber showed that this was incorrect and in fact a much larger tensile load needed to be applied in order to fully open the crack tip. The same was found true for the unloading, that is the crack would fully close prior to a zero tensile load being reached.

In his work, Elber [26] [27] was able to show that during constant amplitude loading the specimen underwent a change in compliance. This change in compliance could be related to the load required to fully open the crack tip. Although the fully open crack tip condition occurs gradually, see Figure 7, a definitive value for the crack tip opening load needs to be determined. This is generally taken as the crack tip fully open load (load P_1 in Figure 7), as it is believed that crack growth cannot occur below this load level [29].

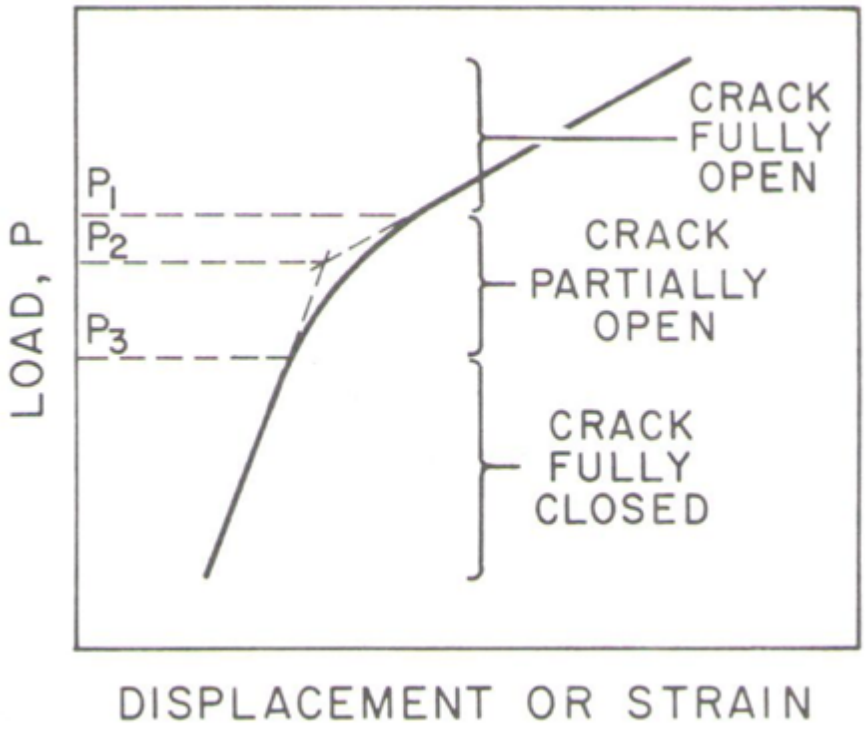

Figure 7. Typical load/displacement data obtained for the determination of fatigue crack closure, the gradient of this curve is the compliance. The crack opening load is often determined by a comparison of gradients at several points along the curve [29].

With this information Elber was able to modify Paris' Law and use an "effective ΔK", that is, only the portion of ΔK above the crack tip opening load is used:

$$\frac{da}{dN} = C(\Delta K_{eff})^m \quad (9)$$
$$where\ \Delta K_{eff} = K_{max} - K_{open}$$

Using ΔK_{eff} largely eliminates the direct dependence of crack growth rate on the load ratio such that one parameter, ΔK_{eff}, could be used instead of two (K and R), thereby demonstrating that crack closure was the mechanism responsible for the effect of load ratio on crack growth rates [29].

Many techniques have been developed in order to measure crack opening load, including eddy currents, electric potential drop, ultrasonic and high magnification photography to name a few [30] [12]. Despite the range of options available, the compliance method has become the most widely used approach, mainly due to its experimental simplicity. Back face strain (BFS) gages, crack mouth gages or clip gages are popular options that allow measurement of displacement and force values required for compliance calculations.

Although methods have been developed to determine the crack tip opening load it is important to understand the mechanisms that contribute to crack closure. McEvily [31] identifies and discusses six mechanisms contributing to crack closure:

- Plasticity Induced Closure;
- Roughness Induced Closure;
- Crack Filling Closure;
- Transitional Closure;
- Transformation Induced Closure; and
- Grain Boundary Induced Closure

It is important to note that with the exception of Grain Boundary Induced closure all of these contributing mechanisms are crack-wake related [31]. Many others have devoted time and effort to understanding each of these closure mechanisms [32]. However, in most

cases closure measurements will be a gross combination of the above mechanisms. Most commonly plasticity and roughness-induced closure are major contributors [29].

It is generally accepted that as fatigue crack growth rates approach threshold levels, the effects of closure generally become greater and can be in many cases used to explain crack propagation properties in the near-threshold region [32]. It is therefore an essential aim to control, minimize and monitor crack closure effects in the threshold region.

2.3 Short Crack Growth

Up until this point, the discussion of fatigue crack growth rates and closure has only considered what are commonly termed long cracks. Closely intertwined with the problems of determining crack growth rates in the threshold region is the problem of short crack growth. Short fatigue crack propagation is essentially when no unique relation exists between the crack growth rate and ΔK [33] unlike with long cracks in the Paris region. This is generally identified as variation in the crack growth properties of the short crack when compared to the long crack in the same material [34].

It is first necessary to define what is considered a small vs. long crack. In principle, a crack is considered small when it is smaller than 1-3mm (based upon metallurgical features), though physically the important characteristic is the break down of similitude [33]. Many tesxts delineate small cracks into two groups. The first is the microstructurally or microscopically short crack (MSC) in which the crack length is of the same order as metallurgical features [35]. The second is the physically small crack (PSC) in which the crack length is small compared to the scale of local plasticity [35]. Long cracks are cracks in which the conditions of LEFM are met and in which LEFM suitably describes their growth properties.

Local microstructure features can significantly affect cracks of in which the crack lengths are of the same order of magnitude as the plastic zone size. McEvily and Boettner [21] observed that short crack growth rate is dependent upon grain orientation. Yoder et al [36] demonstrated that variability in the threshold value was proportional to the square root of the average grain size. Navarro and de los Rios [37] have also suggested that growth rate of a short crack is a factor of the plastic zone size and the location of the nearest obstacle to

the crack tip. Several others [13] [38] have also shown and confirmed that short cracks can propagate at rates faster than long cracks subjected to the same ΔK.

This variation in behavior is often shown in a variation of Figure 8The solid curve is generally obtained from a typical constant amplitude-loading test performed in accordance with ASTM E647. Crack S1 represents a crack that begins to grow but eventually arrests. Crack S2 represents a small crack that experiences retardation before growing rapidly below the accepted threshold, eventually merging with the steady-state-long-crack curve. Crack S3 shows that the small crack may initially grow faster than the long crack at the same ΔK but does approach the steady-state-long-crack-curve.

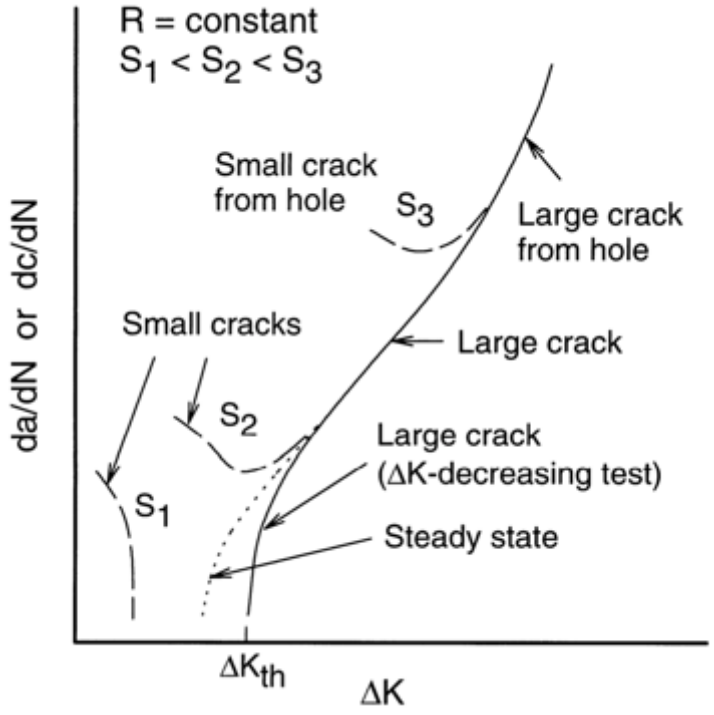

Figure 8. Representation of small crack growth compared to the idealized large crack growth curve [34].

Along with the microstructural features listed above, the variation in crack growth rates is often affected by a lack of closure [34]. A short crack is not influenced by a plastic wake [39] (as in the long crack), and therefore the local crack tip ΔK is higher.

The effective measurement of a material fatigue threshold and short crack growth properties is dependent upon minimizing the effects of closure and providing a "pristine" structure unaffected by previous loading.

2.4 Compression Pre Cracking

The ASTM methods for threshold determination described previously have been challenged as evidence [40] [41] [14] indicates that they may influence the data they produce. The LR method has been shown to induce high crack closure loads [42] [43] and remote crack-surface closure [43] [44], resulting in higher thresholds and lower crack growth rates in the near threshold region. The ASTM E647 LR method has also been shown to produce a fanning of the crack growth rate data in the threshold region for some materials (fanning gives more spread in the ΔK-rate data in the threshold hold region compared to the mid-rate region) [45].

It has become clear that the LR method does not necessarily generate steady state crack growth rate data, as was intended by the ASTM [45]. In an effort to combat the above issues and produce steady state crack growth rate data in the threshold and near threshold regions, with minimal load history effects, the compression-compression pre-cracking method has been developed by Hubbard, Topper and Au, Pippan, Forth and Newman [46].

Hubbard [46] proposed the basic mechanisms of crack growth in cycle compression in 1969, and further refined by James [47]. Upon the application of a compressive load the material yields in compression at the notch, resulting in compressive plastic zone. As the load is removed a monotonic tensile plastic zone is formed. As the cyclic loading is continued a cyclic plastic zone is formed inside the monotonic tensile plastic zone. This cyclic plastic zone is responsible for fatigue crack formation and growth. As the crack starts to propagate though the residual stress field the residual stresses relax, which in turn reduces the size of the cyclic plastic zone. This process continues until a threshold is reached. Figure 8 shows this process diagrammatically. It is evident from Figure 9 that there still exists a zone which as been plastically effected. James [47] demonstrated that crack growth rates reach a steady state (i.e. minimal crack starter notch and tensile residual stress effects, and stabilized crack closure behavior [14]) approximately two

plastic zone sizes past the crack tip, see Figure 10. It is therefore common practice to grow the crack two to three plastic zone sizes before crack data is considered valid [48].

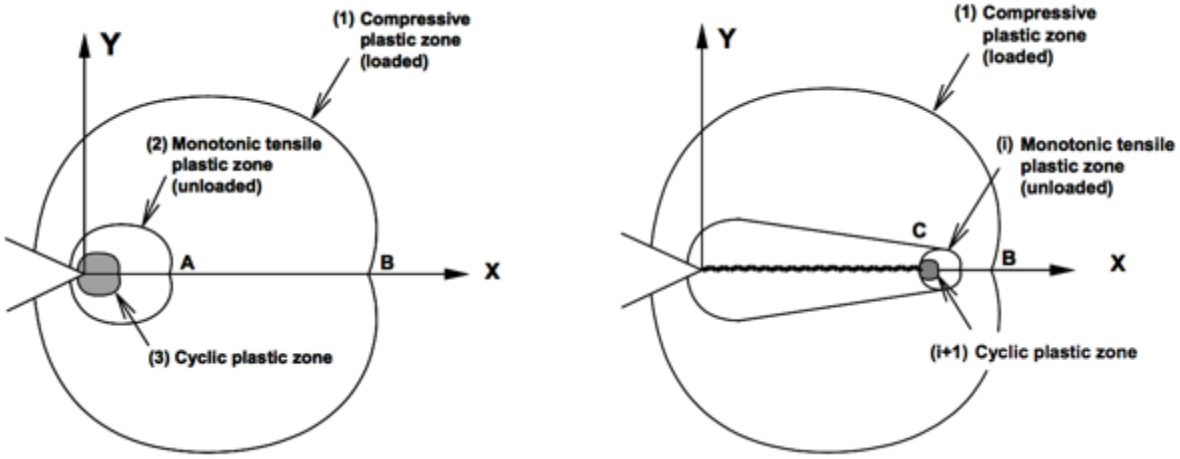

Figure 9. Compressive and tensile zones as a result of compression pre-cracking [48].

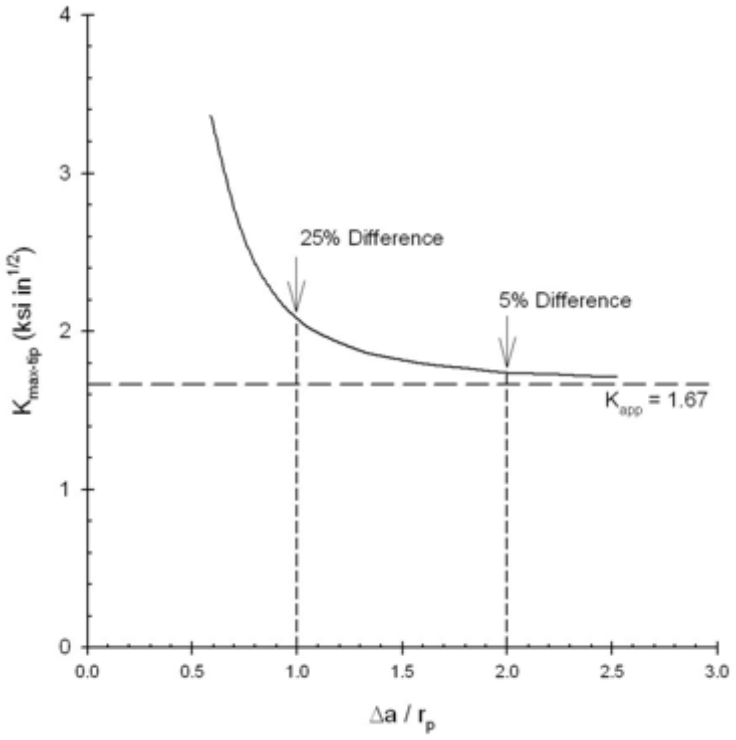

Figure 10. Convergence of applied and crack tip stresses past the crack tip [48].

Once the specimen has been pre-cracked the desired loading can be applied. This research will use the Compression Pre-Cracking Constant Amplitude (CPCA) and Compression Pre-Cracking Load Reduction (CPLR) loading methods as described by Newman [48]. The CPCA method involves pre-cracking in a compression-compression cycle until a small crack is evident and has arrested. An estimated constant amplitude tension-tension cycle is then applied. If no subsequent crack growth is observed after about 500,000 (i.e. crack S1 from Figure 7) the load is increased by 5-10%. This process is continued until crack growth is detected, from this point the applied load remains constant. Figure 11 contains a visual representation of this process.

The CPLR method involves pre-cracking in a compression-compression cycle until a small crack is evident and has arrested. The standard ASTM LR procedure is then followed. In this case an estimate for the starting applied load needs to be determined. This load generally based upon the ASTM E647 recommendation that the initial da/dN should be below 3.937×10^{-7}in/cycle. Figure 11 contains a visual representation of this process.

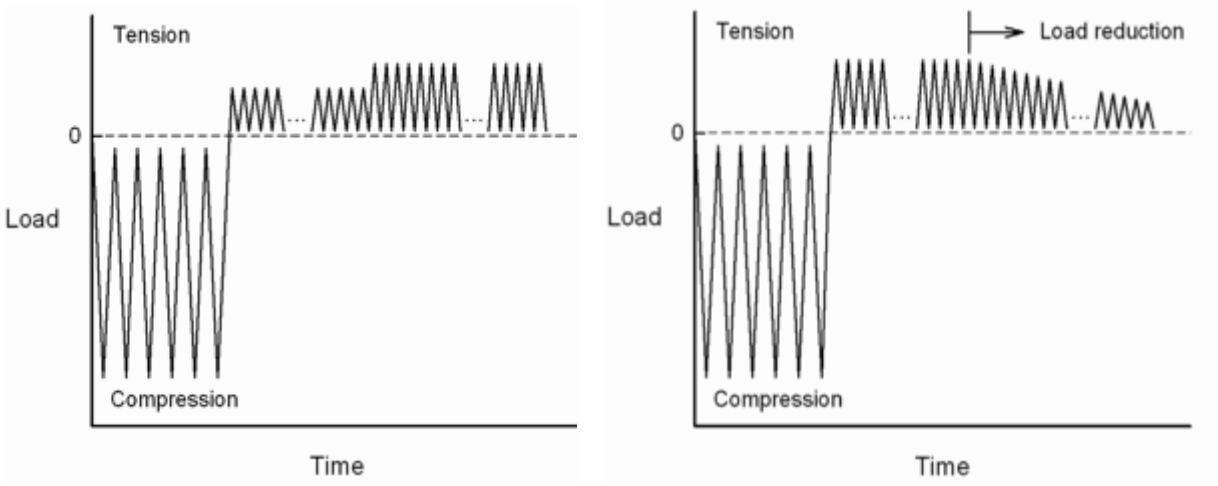

Figure 11. CPCA (left) and CPLR (right) loading sequences [45].

A range of materials have been tested using the compression-compression pre-cracking procedure [14]. These results have then been compared against baseline tests performed using the ASTM procedures. Some materials such as 4340 steel have not shown a

considerable difference in the threshold obtained, see Figure 12. Conversely other materials such as Ti-6Al-4V have shown the threshold obtained is sensitive to the type of method applied, see Figure 12. It is acknowledged that these are vastly different materials, even so, no definitive material property adequately explains these observed effects.

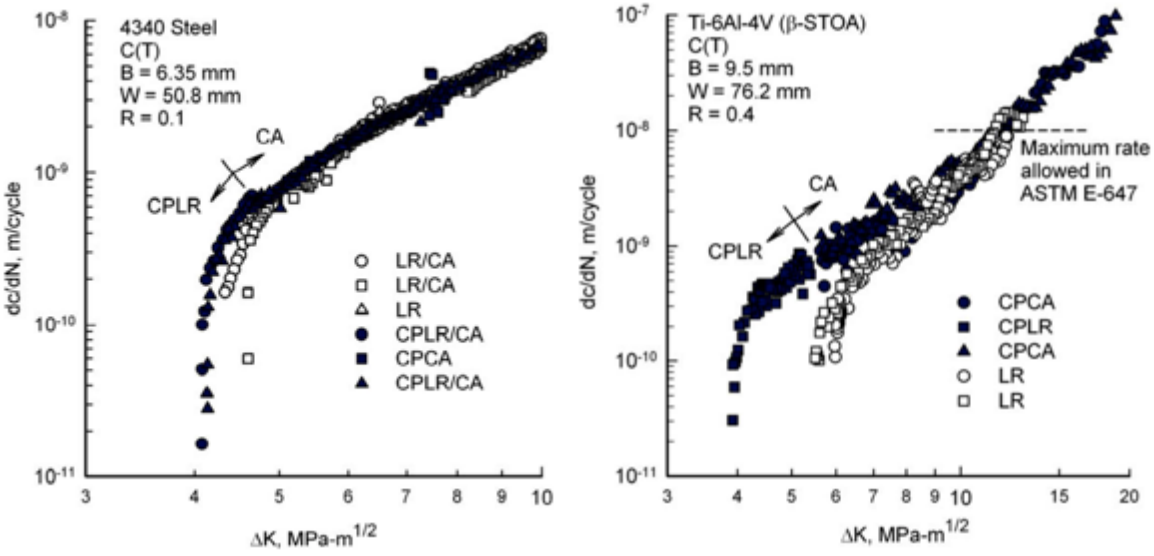

Figure 12. Results of ASTM load reduction and constant amplitude loading tests against the same tests but using a compression pre-cracking method [45].

CHAPTER 3. EXPERIMENTAL SETUP

3.1 Overview

This project utilises an MTS Fatigue Testing System, in order to apply a range of variable loading configurations, under a range of varying conditions. Monitoring of crack growth is achieved by use of a BFS gage. Monitoring of crack length and wide field strain is accomplished through the use of a high resolution-high magnification camera and Digital Image Correlation (DIC) software. This chapter details the appropriate set up and calibration of the equipment.

3.2 MTS Fatigue Testing System Setup

3.2.1 Actuator and Load Frame

The load frame used for these tests is a custom design built by the Purdue University Fatigue Lab in the School of Aeronautics and Astronautics. The actuator, actuator base-plate, upright columns and crosshead can be interchanged as required (individually or as a complete assembly). For these set of tests a MTS Model 244.12 5.5Kip Hydraulic Actuator was selected and installed. A 4-foot set of uprights and appropriate crosshead were selected and installed. Figure 13 depicts the]is general set up.

Figure 13. General MTS machine setup

3.2.2 Load Cell

Based upon the expected loads during the tests (Chapter 5, Section 2 for calculations), a MTS 1.1kip load cell was selected and installed. The maximum expected loads for the tests fall within 10-90% of the load cell range.

The selected MTS load frame and actuator are designed to be used primarily with 1-14 thread mounting hardware and grips. However the 1.1kip load cell is designed for use with ½-20 thread mounting hardware and grips.

As a result a 10kip load cell is mounted to the crosshead using the standard 1-14 thread hardware. The 1.1kip load cell is mounted to the 10kip load cell using a 1-14 to ½-20 adaptor. A ½-20 to 1-14 adaptor is used to mount the upper grip to the 1.1 kip load cell. Figure 14 displays a close up of the adaptor set up.

In this system with a lengthened load train (due to adaptors), stiffness was a concern. Mild steel was used for the adaptors, increasing mass and stiffness. Several lock nuts were installed to help achieve and maintain alignment and stiffness. See Chapter 3, Section 3 for a further discussion on alignment procedures.

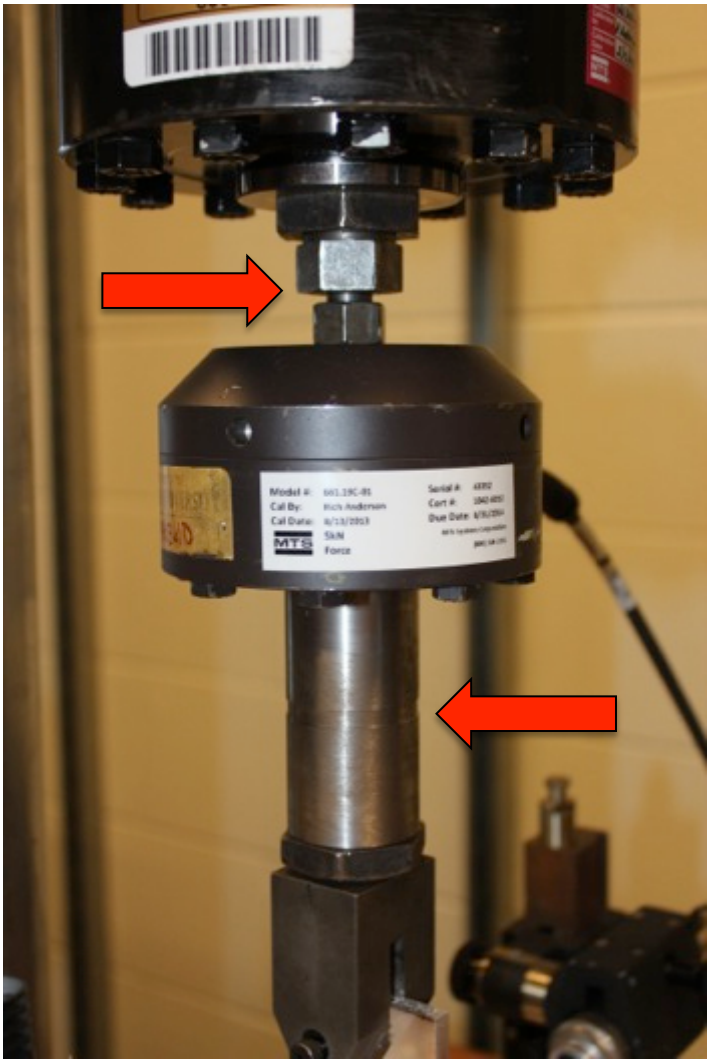

Figure 14. Close up image of the two adaptors (indicated with red arrows). Both adaptors have been precision machined from mild steel.

3.2.3 Controller and Calibration

A MTS FlexTest40 Controller was utilised for all testing. This controller provides real-time closed-loop control, with transducer conditioning and function generation to drive a servo hydraulic test system [50]. The system is based on the 494 hardware chassis and carrier boards.

The system uses the MTS 793 MultiPurpose Elite Software package. This software provides all user, tuning and calibration functions in a simple to navigate user interface.

The testing setup was fully tuned and calibrated by a MTS technician prior to the commencement of testing.

3.3.4 Clevis Grips

The grips used for testing are of the clevis type. They conform to the requirements of ASTM E647 for the ESE(T) type specimen being tested. The clevis pins being used are ¼" diameter, conforming to the size requirements of ASTM E647. The pins are rated for a 6000lb load. Figure 15 shows the pin and clevis grip utilised.

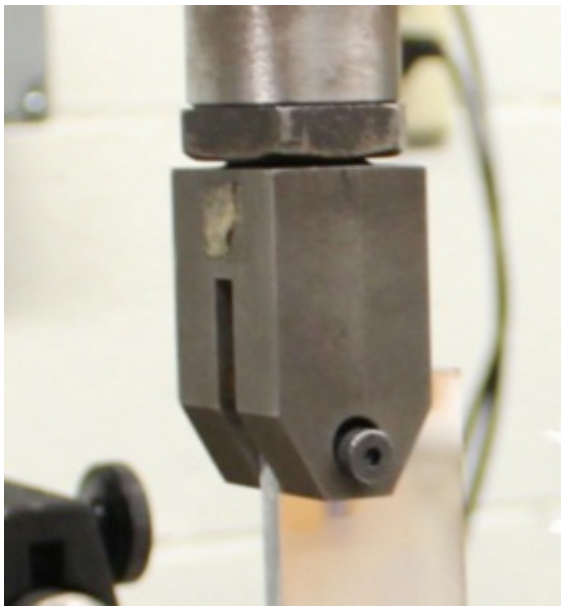

Figure 15. Clevis grip and pin that was utilized during testing.

3.3 Alignment of Load Train

3.3.1 Overview

The crosshead is fitted with a MTS 609.10 Alignment Fixture. The alignment fixture allows adjustments to be made in two dimensions to correct concentricity and angular misalignment through the load train [51]. Initial alignment of the load cell and actuator is achieved during calibration by the MTS technician. The actuator was aligned to the 10kip load cell base to an accuracy of 0.001" or better. This is achieved through use of the alignment fixture and a fine scale measurement gage.

With the addition of the thread adaptors and grips, the alignment of the lengthened load train was checked using a precision-machined 0.25" thick alignment sample. Use of the sample revealed misalignment that required correction. The alignment procedure was carried out using the MTS Alignment Fixture Manual [51] and ASTM E1012 [52].

The limit for bending strain in any sample is generally determined as a result of the type of testing and desired test outcomes. For basic crack growth testing ASTM E647 does not provide specific guidance for the ESE(T) specimen to be used in this research. ASTM E647 does however provide a 5% bending strain limit for the Middle Tension (M(T)) specimen. For the purposes of alignment this 5% limit was taken as a suitable level for the ESE(T) specimen.

3.3.1 Alignment Sample Construction

Correct alignment of the load train requires an instrumented sample to provide feedback during the alignment procedure. A sample such as this was unavailable and needed to be constructed.

A 5" x 1.5" x 0.25" sample was precision-machined from 6061 Aluminium. This sample was created to reflect the dimensions of the actual samples to be used in testing.

For the sample configuration being used (thin, flat sheet), it is recommended to have at least two rows of strain gages centered around the central axes of the large face (strain gages are placed on both the front and back surfaces in mirror locations).

A series of eight strain gages were installed in locations according to the MTS Series 609 Alignment Fixture Product Manual [51] and ASTM E1012 [52]. The strain gages were installed in accordance with the procedures outlined in Vishay Measurements Group Student Manual for Strain Gage Technology [53]. The strain gages and lead wires were mounted in a quarter-bridge setup. Figure 16 shows the rear face of the alignment sample with strain gages and lead wires connected.

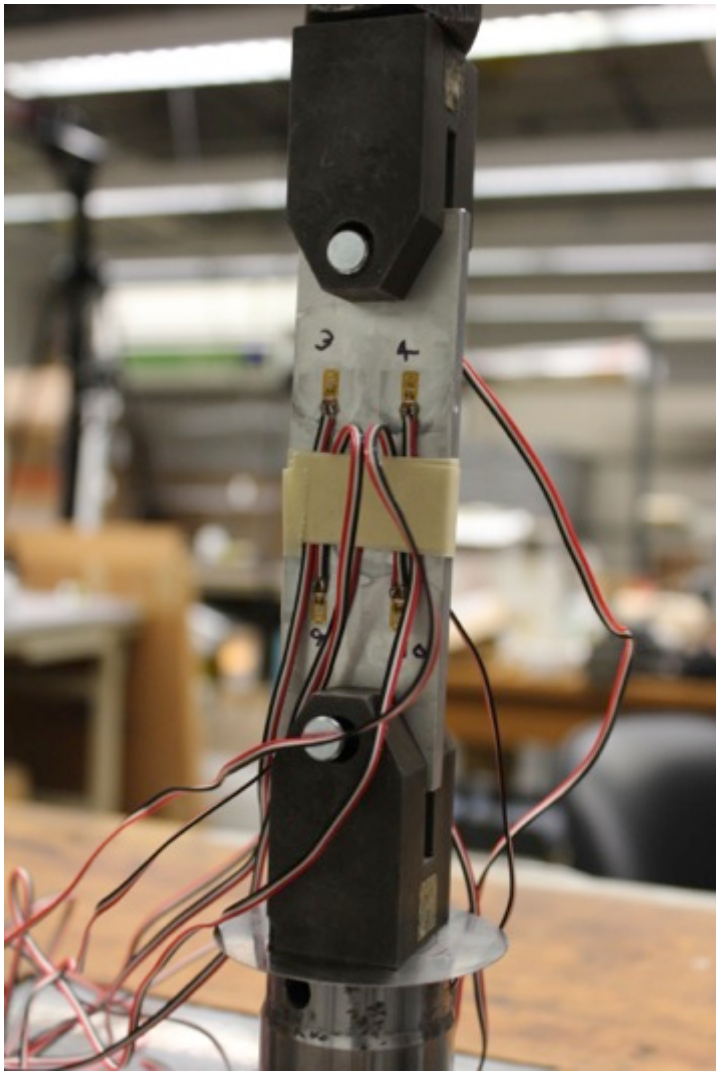

Figure 16. Image of the rear face of the alignment sample showing strain gage installation and location.

3.3.2 Alignment Procedure

In order to obtain strain readings, the eight strain gages were connected to a MicroMeasurements Switching and Balancing Unit (on loan from School of Civil Engineering) and a Model 3800 Strain Indicator. Figure 17 shows this set up.

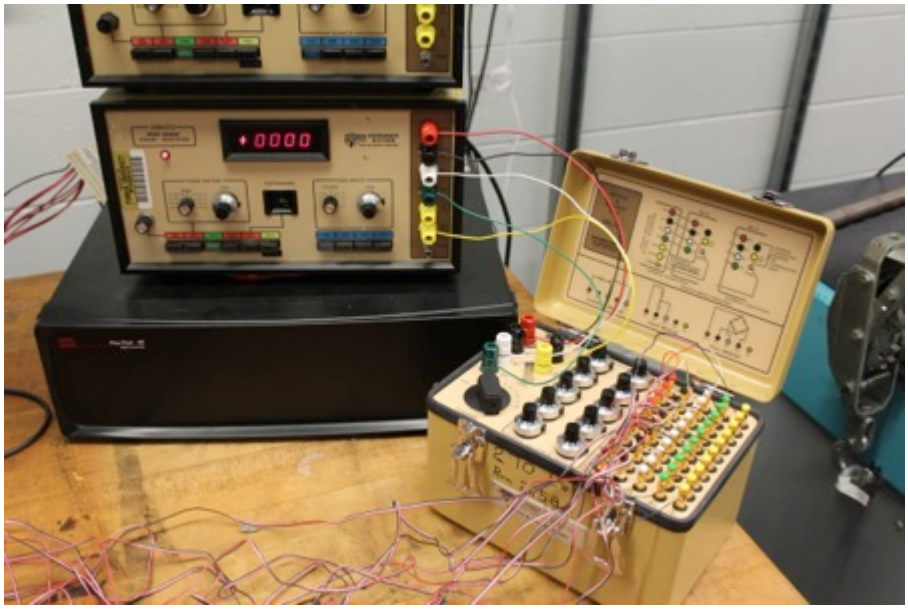

Figure 17. Micromeasurements 10 Channel Switching and Balancing Unit and Model 3800 Strain Indicator used to calibrate strain gages and obtain strain readings.

The strain gages were all balanced and zeroed before loads were applied. As specified in both alignment procedures, a number of loads that are representative of those applied to the specimen during the experiment are tested during the alignment procedure. The loads in this case were 200lbs, 400lbs, 600lbs and 800lbs. After an initial series of loading the baseline alignment was determined. The sample was then loaded to 600lbs to allow alignment adjustments. After each adjustment was made the load range was exercised a number of times before measurements were taken. This procedure was completed a number of times to ensure that all bending strains were within prescribed 5% bending strain limits.

3.3.3 MTS and ASTM Alignment Results

Each loading sequence was performed a number of times. The final loading sequence data and calculations can be found in Annex A. Calculations completed against the MTS Alignment Fixture Manual provide a maximum bending strain of approximately 3%. Calculations completed against the ASTM standard provide a maximum bending strain of approximately 4%.

3.4 ASTM E647 Compliance

As previously noted, ASTM E647 governs the conduct of fatigue testing. It contains a number of regulations, recommendations and guidelines for testing. Unless otherwise mentioned throughout the text, ASTM E647 was followed faithfully.

Prior to testing a number of trials were conducted on two dummy specimens to ensure ongoing compliance with the standard throughout the experiments. The first dummy specimen was a solid aluminum bar (representative of the real specimen but with out a notch). This dummy specimen was used to ensure that K_{max} control and ΔP control requirements were met consistently at a range of frequencies. Force compensator gain and hydraulic pump oil temperature and supply pressure were the variables modified in this testing. It was found that the maximum frequency that could be applied while remaining in the tolerances of ASTM E647 was 18Hz at an oil temperature of 117°F and supply pressure of 2800psi.

A second instrumented dummy specimen was utilised to ensure force shedding, crack measurement precision, da/dN rates and closure calculation requirements were all met. The software mostly performs the calculations as the test progresses.

3.5 DIC Imaging Setup

3.5.1 DIC Camera

The camera to be utilised for the DIC image capture is an Allied Vision Technologies Manta Model 210. This camera can be utilised with a range of objective lenses of varying magnification. For the purposes of the experiments the 10x and 20x

magnification are the most commonly used. The 10x lens is most often used for wide field strain field capture and the 20x lens for crack length measurement. The camera also utilizes a magnification adaptor that features a light source attachment. It was found that the provided light source (even though variable) was too intense due to the polished surface of the specimen. It was found that a white plastic bag (layered four times) diffused the light such that suitably imagery could be obtained. Figure 18 details the camera and lens setup.

Figure 18. Allied Vision Technologies Manta 210 camera setup.

3.5.2 DIC Mounting Hardware

The DIC camera is mounted to a 3 axis precision translation stage. This precision translation stage allows focusing adjustments and crack length measurements to be to an accuracy of 0.00004” (0.001mm). The stage is mounted on a roller-platform and high quality 3 axis adjustable tripod. Due to the sensitivity of the camera to vibration the

tripod is placed on granite blocks placed on high-density foam mats. See Figure 19 for imagery of the translation stage setup.

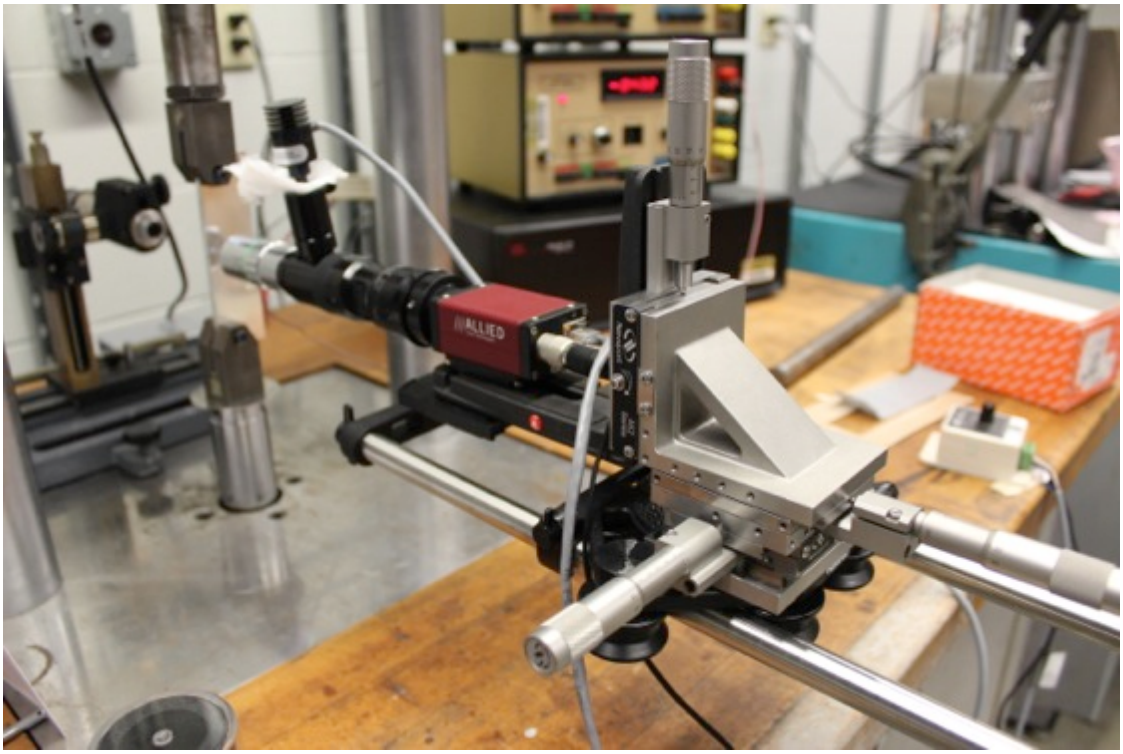

Figure 19. Camera translation stage.

3.5.3 DIC Software

Three software packages are used to capture and process the DIC imagery. Two of the software packages are for imaging and control of the camera. The first is an IP Configuration software that provides the link and interface from camera to computer. The second is the AVT Vimba Sample Viewer software (supplied by AVT with the camera) that provides image capture and manipulation capabilities. The third software package is VIC-2D from Correlated Solutions that provides the capability to perform the actual DIC.

3.6 Data Acquisition

3.6.1 Fatigue Data

Fatigue data acquisition, recording and analysis is largely performed automatically within the developed code. The exceptions to this are reverse face crack length measurements (obtained by a 10x travelling monocular telescope) and front face length measurements (obtained using the DIC camera). This allows correlation between the BFS data and to ensure a straight crack front.

The primary data recorded are crack length and cycle count. Applied force is also recorded to ensure force limits are being met and, along with the applied strain, which is recorded periodically for use in crack closure calculations. The crack growth rate and stress intensity are periodically calculated within the code and stored for later analysis

3.6.2 DIC Imagery

Due to DIC image frequency capture rates, specimen loading frequency and image focusing, it is very difficult to use automated image capture. Although an automated trigger device was developed, due to high zoom levels, sensitivity to vibration and variances in loading and image capture frequencies it is difficult to maintain focus. This is also compounded by the fact that to capture the full field strain zone a number of adjacent images are required; the translation stage is not mechanized in order to permit this. As a result the developed code enables the user to periodically pause the test in order to capture DIC imagery.

When it is desired to capture imagery the user will prompt the program to stop and they will manually move the translation stage to the required point. When the desired image has been focused and can be seen on screen the user simply needs to right-click to save the image. The user can then move the camera as desired to capture the next image.

3.7 Specimen Properties and Preparation

3.7.1 Material Overview and Properties

The material being tested in this series of experiments is 7085-T7452 Aluminium. This material is basically a high purity, high zinc content 7XXX Aluminium alloy. The chemical specification is shown in Table 1 below. This alloy has also been shown to have desirable thick section mechanical properties and also improved fracture toughness and fatigue properties over other more conventional alloys such as 7075 and 7050. Table 2 below details basic material properties.

Table 1. Aluminum 7085 Chemical Composition [54]

7085 Chemical Composition Specification Limits (wt.%)							
	Zn	Mg	Cu	Fe	Si	Zr	
Max	8.0	1.8	2.0	0.08	0.06	0.15	
Min	7.0	1.2	1.3	N/A	N/A	0.08	

Table 2. Aluminum 7085 Material Properties [54]

Basic Material Properties	
σ_{ult}	63 ksi
σ_{yield}	70 ksi
Elastic Modulus	10400 ksi
Density (ρ)	0.103 lb/in^3
K_{IC}	31 ksi$\sqrt{in}$
Coefficient of Thermal Expansion	$13.7\times10^{-6}\frac{in}{in}/°F$

3.7.2 Dimensions

Figure 20 details notch location, pin holes and pin hole counterbore dimensions along with the applicable tolerances. The specimens have counterbored pin holes as this has been shown to reduced in plane bending stresses and produces a more even crack front [55]. All specimens were within tolerances.

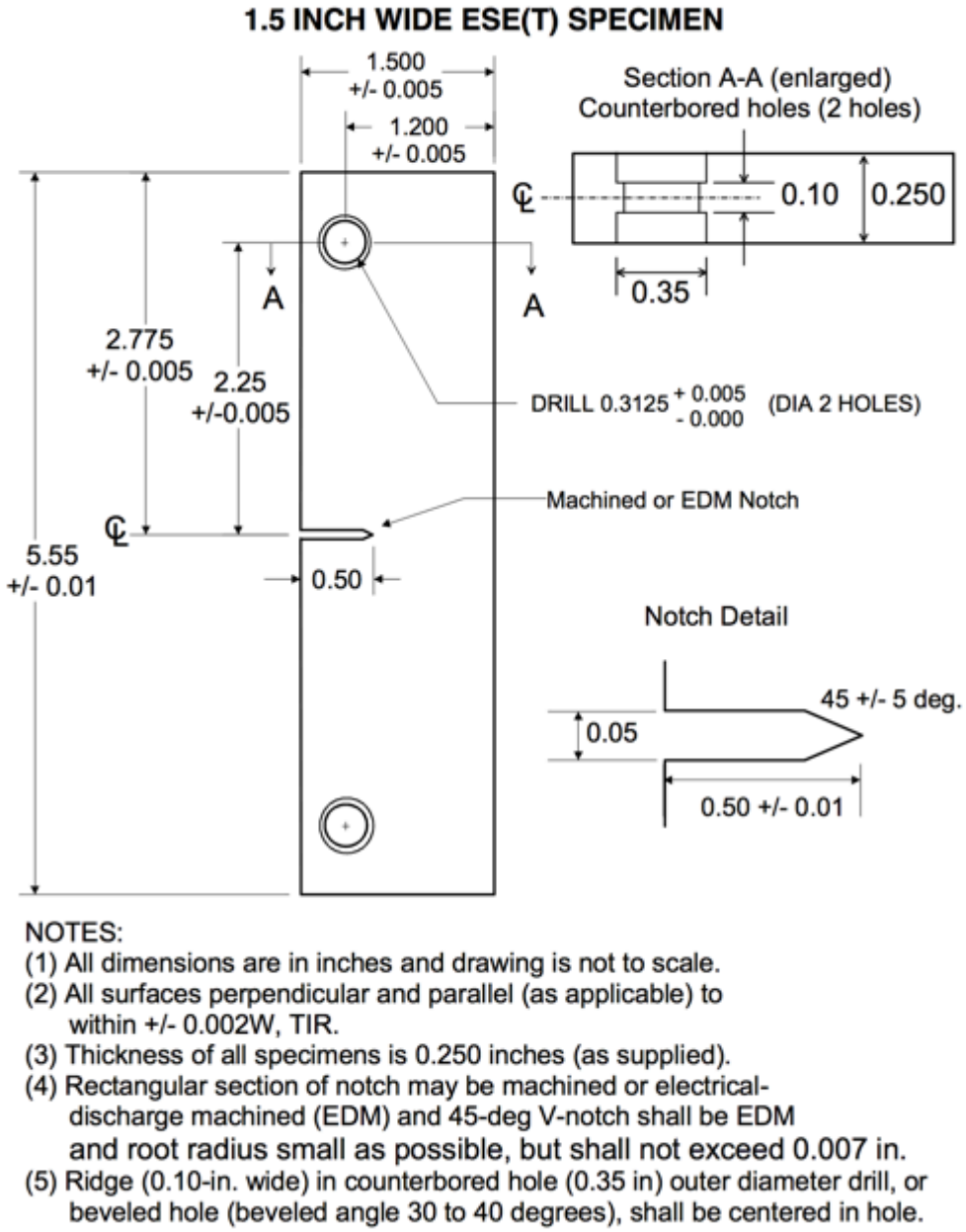

Figure 20. ESE(T) Specimen Layout and Dimensions [56].

3.7.3 Polishing

The specimens were received in a semi-polished state, however surface imperfections were still clearly visible. For the best results from the DIC imagery it is best to have a "mirror" finish. To obtain this "mirror" finish a Buehller EcoMet V 8" polishing machine was used. Depending upon the surface condition of the specimen, polishing can start using 320 grit wet/dry polishing pad, working up through grit sizes as uniform surface conditions are reached before finally using a microfiber polishing pad. Due to smooth finish already on these specimens it was possible to start with the microfiber polishing pad in conjunction with a silica-colloidal solution. Figure 21 shows the difference between the supplied and final surfaces finish.

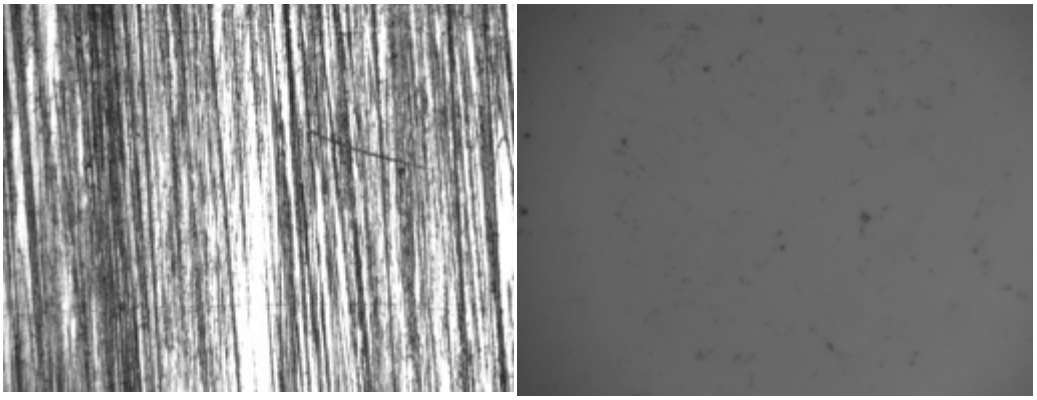

Figure 21. As delivered surface finish (left) and polished surface finish after using silica colloidal solution and microfiber polishing pad (right).

3.7.4 Strain Gage Selection and Application

Previous research on compression pre-cracking with BFS measurements has used a CEA-06-062UW-350/P2 type strain gage [56]. This type of strain gage was unavailable worldwide without a four month lead time. The CEA type strain gage is preferable as it is a universal general-purpose strain gage suitable to fatigue testing. It also comes with enlarged copper tabs for direct soldering of lead wires to the strain gage instead of using jumper wires. Previous research had also revealed that the gage length of 0.062 inches was close to ideal for the application [56]. With this information only, one type of suitable

strain gage was identified and conveniently available, the CEA-13-062UW-120. The change in thermal compensation from 6 to 13 was acceptable as this matched the thermal characteristics of the 7085 material as shown in Table 2. The reduction in resistance to 120 was also deemed acceptable considering the number of cycles the strain gage would be subjected to, as well as heat dissipation characteristics.

Strain gage application was performed in accordance with the Vishay Measurements Group Student Manual for Strain Gage Technology [53]. The basic steps are degreasing the specimen, sanding the application surface with fine grit sandpaper, application of a surface conditioner and neutralizer, test fitting strain gage, bonding strain gage to specimen surface, installation of lead wires and finally application of a polyurethane coating to protect the strain gage and lead wire installation. Before and after installation of the lead wires a multi-meter is used to ensure that the strain gage is operating within 2% of the nominal value and has not been damaged during installation.

Care must be taken during the strain gage installation to ensure that the polished surface (particularly in the region of crack propagation). This is achieved by using a small vice and gauze pads to hold the sample during strain gage application, see Figure 22. Alternative protective methods (such as no-tack plastic coatings) were investigated but all resulted in a compromised polished surface (believed to be due from fumes from the adhesive used to bond the strain gage to the specimen).

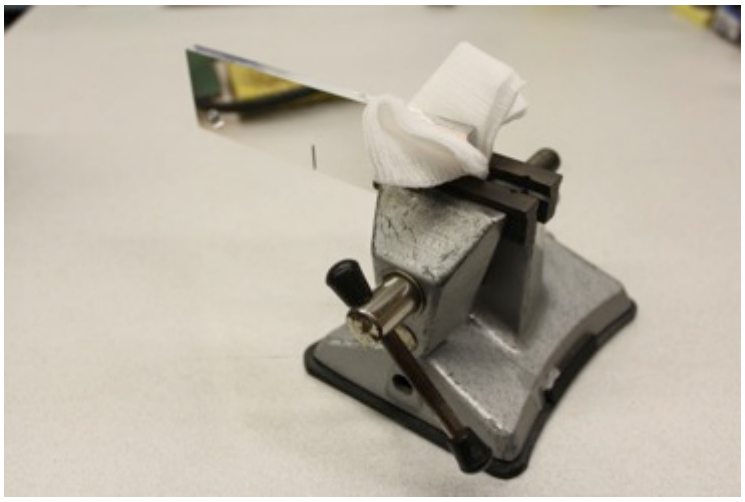

Figure 22. Setup used to hold the sample during strain gage installation.

3.7.5 Speckle Pattern Application

The speckle pattern is a number of small silica based particles that have been temporarily bonded to the surface of the sample through an electrostatic force. The Fatigue Lab Speckle Application Procedure [58] was used as the guide for speckle application. It is desired that the speckle particles be evenly and uniformly distributed after application. However to ensure a suitably dense covering a relatively high air pressure is required which ultimately results in clumping of the speckle particles. It was found that the placement of a filter pad directly in the path of the particles removed nearly all evidence of speckle particle clumping. The filter pad is required to be shifted slightly during the application procedure to ensure a uniform coating. A suitable application of speckle pattern can be seen in Figure 23 at 20x and 40x magnifications. Figure 24 shows the speckle pattern viewed without magnification. Ideally it should appear like a layer of dust on the specimen surface.

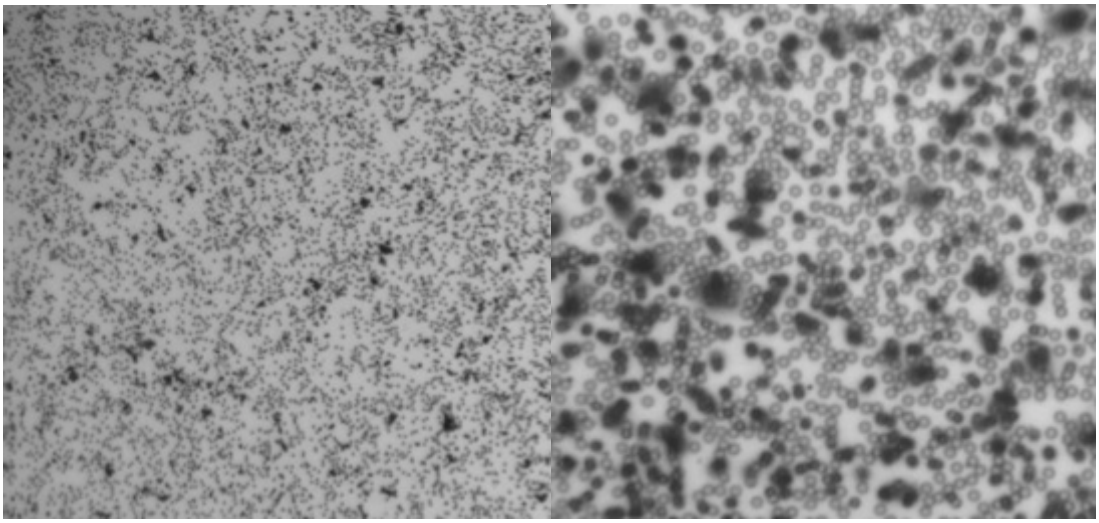

Figure 23. Suitable speckle pattern viewed at 10x magnification (left) and 20x magnification (right).

In the event that clumping is evident, see Figure 25, a short burst of compressed air can clear the clump. It may also damage the surrounding speckle and require repair of the pattern. Suitable care must be taken as damage to the speckle pattern will, in many cases,

damage the surface of the specimen and require re-polishing which requires removal and disposal of the strain gage.

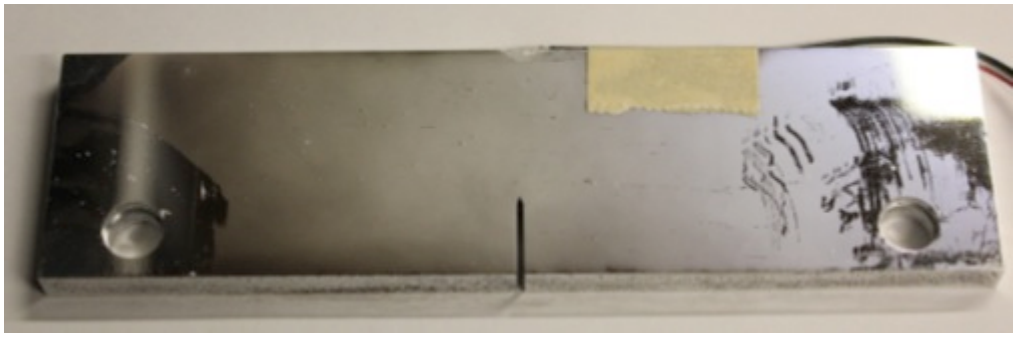

Figure 24. Suitable application of speckle pattern. Although some clumping is evident, the crack path is clear. The distubrance of the pattern around the pin holes is due to the clevis grips, this is normal.

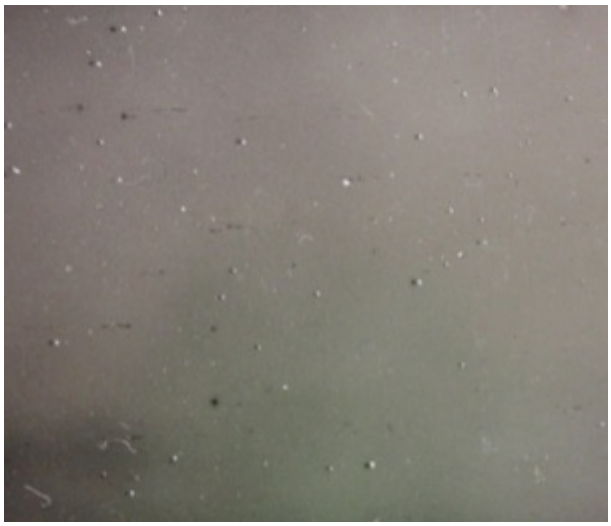

Figure 25. Clumping of silica particles on the material surface.

CHAPTER 4. EXPERIMENTAL PROCEDURE

4.1 Overview

The MTS MultiPurpose Elite software enables the user to design their own custom testing procedure to meet any testing requirements and outputs that they may desire. The testing procedure that has been developed enables the user to select either a CPLR or CPCA test. The test runs until a range of preset conditions have been met. Crack length and cycle count are calculated and monitored throughout the test. Additional data captured throughout the test allows further conclusions and inferences to be made.

4.2 Test Procedure Outline

The basic test flow assumes that the user wants to conduct a CPLR test. Once the CPLR component is completed and the desired threshold value has been determined the test automatically switches to a CPCA test. Starting with a CPCA test will not affect the execution of the program. The CPLR code flow chart is shown in Figure 26 and the CPCA code flow chart is shown in Figure 27. Note that these figures detail only the logic flow for the program. As mentioned it is assumed that the CPLR test will be performed, this part of the test is bracketed by the red box in Figure 26. Once the CPLR test is complete the CPCA component begins, this part of the test is bracketed by a blue box. There are two CPCA sections, the second, bracketed by a green box, is identical to the first except that the loading frequency is reduced in order to capture sufficient data. The pre-cracking section bracketed in yellow is only conducted if a CPLR test is not conducted. A full step by step program flow chart can be seen in Annex B. Code for embedded automatic calculation functions can be seen in Annex C.

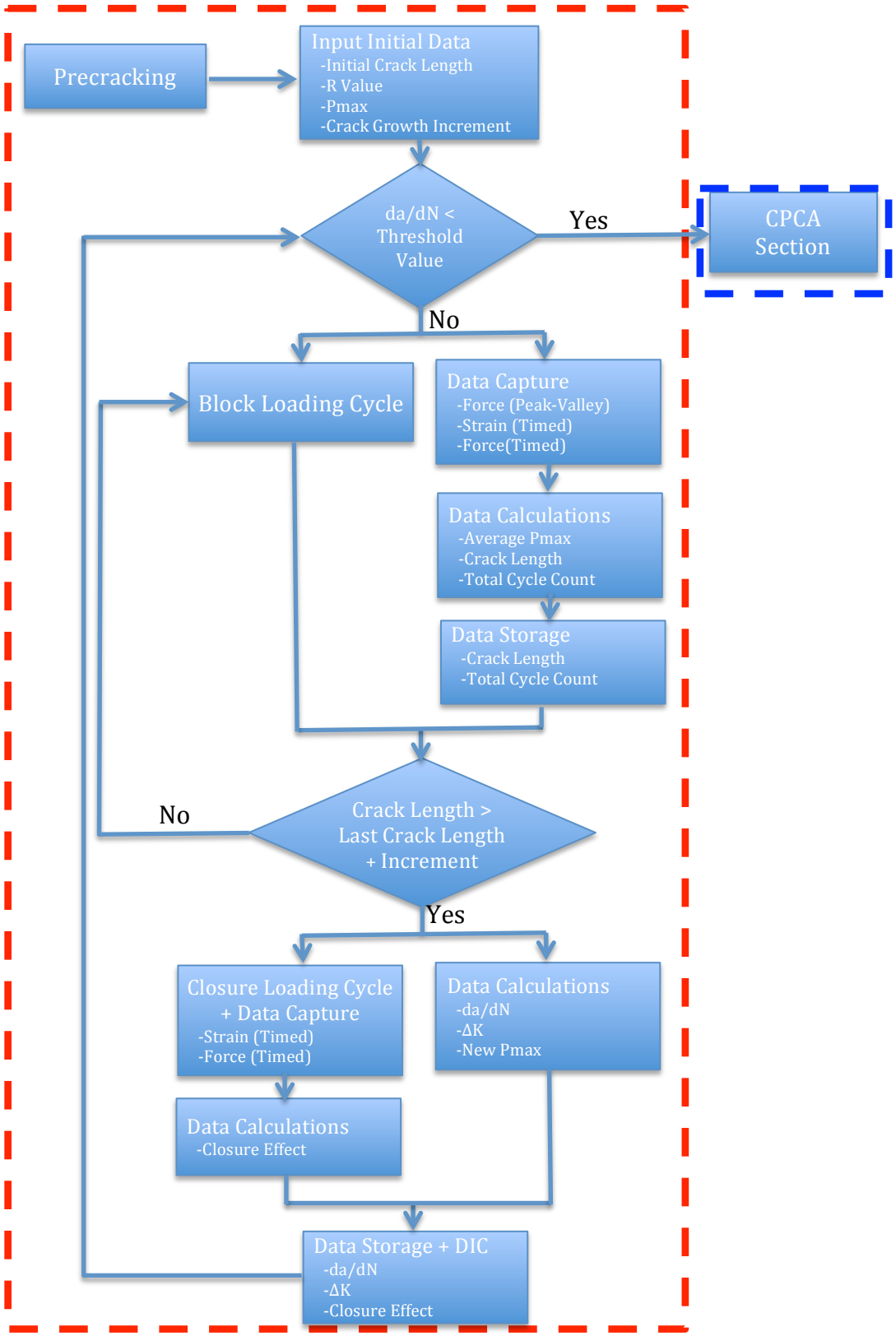

Figure 26. CPLR Code Flow Diagram.

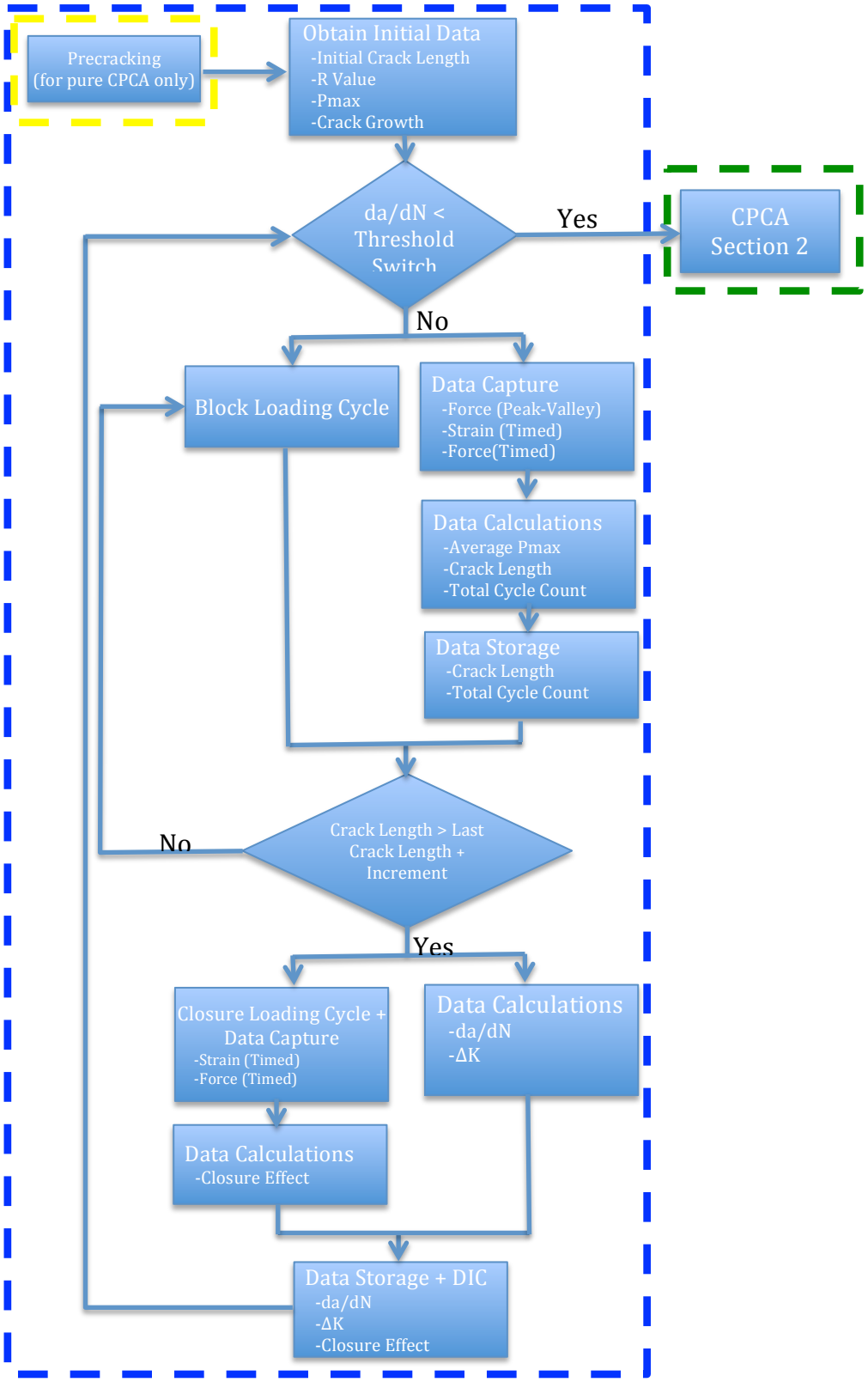

Figure 27. CPCA Code Flow Diagram.

4.3 Testing Processes

4.3.1 Overview

Once the specimen has been prepared and instrumented it is loaded into the MTS machine. During loading it is inevitable that there will be some "damage" to the speckle pattern and polished surface around the grips. This is not an issue provided that the area of crack propagation is not damaged.

There are two main phases to testing, pre-cracking and crack propagation, each containing sub-elements. These elements and the details behind each will be discussed.

4.3.2 Pre-cracking

The specimen is initially pre-cracked in cyclic compression-compression loading. Prior to the commencement of the compression cycling it is recommended to apply a small compressive load through manual machine control. This load should be around 10-20lbf. This pre-load prevents the machine from taking up load too quickly and possibly influencing crack growth. The minimum load is determined through the following relationship [48].

$$\frac{|K_{cp}|}{E} = 0.001 \; to \; 0.002 \; in^{1/2} \tag{10}$$

In this relation K_{cp} is the stress intensity factor at the minimum compressive stress and E is the material elastic modulus. The value of K_{cp} is placed into the following relationship [48], which is solved for load (P).

$$\frac{K_{cp}}{P} = \frac{G(2+\alpha)}{(BW^{1/2})(1-\alpha)^{3/2}} \tag{11}$$

$$Where \quad G = k_0 + k_1\alpha + k_2\alpha^2 + k_3\alpha^3 + k_4\alpha^4 + k_5\alpha^5$$

$$k_0 = 0.5 \quad k_1 = 2.643 \quad k_2 = -6.3 \quad k_3 = 8.25 \quad k_4 = -5.6 \quad k_5 = 1.59$$

The maximum load is obtained through the following relationship.

$$\frac{P_{max}}{P_{min}} = 8\ to\ 16 \tag{12}$$

The specimen is then cycled between these two levels for 30,000 – 100,000 cycles. At this point a small crack of the order 0.001" – 0.01" should be visible.

Since this initial compression pre-crack automatically arrests itself, it is necessary to further grow the pre-crack in a tension-tension load. As with the compression loading, it is recommend that the specimen is first subjected to a small tensile pre-load of 10-20 lbf to prevent possible crack growth retardation from overload. The maximum load for tension is determined by interchanging K_{max} for K_{cp} Equation 11. The value of K_{max} is determined by estimating where in the da/dN vs ΔK curve it is desired to start. The minimum load is determined through selection of an R-value and the following relationship.

$$\frac{Pmin}{Pmax} = R \tag{13}$$

This tension-tension load should be applied until the crack extension criteria is reached. This criteria states that the pre-crack should be grown two or three compressive plastic zone sizes after compression pre-cracking or by half the notch height (h_n), which ever is greater. The crack extension criteria is described by the following relationship.

$$\Delta a = 3(1-R)\rho_{cp} \quad or \quad \Delta a = 0.5h_n \tag{14}$$

$$Which\ ever\ results\ in\ the\ largest\ \Delta a\ is\ to\ be\ used$$

$$\rho_{cp} = \frac{\pi}{8}\left(\frac{K_{cp}}{\sigma_0}\right)^2$$

$$where \quad \sigma_0 = \frac{\sigma_{Yield} + \sigma_{Ultimate}}{2}$$

It was found for the 7085 Aluminum alloy both equations were used depending on the load ratio selcted.

The specimen should then be cycled in tension-tension loading until the required crack length is reached. The magnitude of tension-tension loading is determined from the type of test being conducted (CPCA or CPLR) and R. It is important to comply with the condition in ASTM E647 that the final K_{max} during pre-cracking shall not exceed the initial K_{max} for which test data are to be obtained [12]. That is the loads should decrease or remain the same. Crack length data is collected from the pre-crack but is not valid until the crack extension criteria is met.

4.3.3 Cyclic Loading

During pre-cracking and cyclic loading the specimen is subjected to a sine waveform. It was shown during MTS Machine setup to provide the best control of P_{max} and P_{min}.
Load is applied in a cyclic blocks that vary in number of cycles depending upon the crack growth rate at the time. At lower crack growth rates a block of 1000 cycles is used. At higher rates this is reduced to 250 cycles. This ensures a relatively even distribution of data points.
The nominal frequency of the applied loading is 15 Hz at lower crack growth rates. At higher crack growth rates this is reduced to 10Hz.
In the cyclic loading blocks, Peak-Valley Compensation (PVC) is utilised to ensure the required loads are reached. This is an inbuilt software feature that provides a feedback loop that compares the commanded load with the load actually reached. During machine setup the most ideal sensitivity of the (PVC) was determined and loaded into the software.

4.3.4 Cyclic Loading Data Acquisition

During the cyclic loading a majority of the data is collected for analysis during the test. The following data types are collected:

- Peak Valley Force Data (P_{max})
- Timed Force Data (Crack Length)
- Timed Strain Data (Crack Length)

The peak valley force data is collected for every cycle. This data acquisition process captures every maximum and minimum load. A sensitivity of 2 lbf is used for this process.

The timed force and strain data is collected in matched pairs. This data represents approximately 120 load/unload cycles. The data is collect at a rate of 1024 Hz, which is approximately 68 data points per cycle. This data is used to determine the compliance and in turn the current crack length. These data collection rates are based off those recommended in the Fracture Technology Associates Users Manual [58].

4.3.5 Cyclic Loading Data Calculations

Crack length is periodically calculated and updated through the compliance method detailed in ASTM E647. However, alternative coefficients developed in other compression pre-cracking experiments are used [48]. These coefficients have the same functional form as those in ASTM E647 but have been shown to provide better results in an ESE(T) specimen. Crack length is determined using the following relationship.

$$a = W \times (A_0 + A_1 U + A_2 U^2 + A_3 U^3 + A_4 U^4 + A_5 U^5) \quad (15)$$

$$Where \quad U = \left[A^{*1/2} + 1 \right]^{-1} \quad and \quad A^* = \left| \frac{\varepsilon E B W}{P} \right|$$

$$A_0 = 1.007 \quad A_1 = -2.171 \quad A_2 = 1.537 \quad A_3 = -7.615 \quad A_4 = 22.181 \quad A_5 = -20.754$$

The ε/P portion of the A^* value is determined by taking the upper 50% of the timed force-strain data. Taking the upper 50% of the data should ensure that closure effects do not affect crack growth determination (this is checked after every 1000 cycles). A linear least squares fit is then performed on this data to determine the slope of the data. This slope represents the averaged value of ε/P over a large number of cycles. The linear least squares fit is performed using a built-in software function, see Annex C.

4.3.4 da/dN, ΔK and P_{max} Measurement

The crack growth rate is determined periodically throughout each test as it is one of the primary control measures. It is used to transition between CPLR and CPCA loading and also when to step down testing frequency and number of cycles per loading block. The crack growth rate, da/dN is measured throughout the test using the simple secant method as it provides suitable accuracy and also is quick and easy to compute. The stress intensity factor is calculated using Equation 9, using the average crack length between the current length and previous measured length to calculate the crack growth rate.

Once the crack has been detected to grow past the crack growth increment in the CPLR phase a new reduced load is calculated. This is determined by first calculating a new ΔK as shown below.

$$\Delta K = \Delta K_0 e^{[C(a-a_0)]} \tag{16}$$

Where ΔK_0 is the ΔK at the last crack growth increment, and a_0 is the corresponding crack length. ΔK and a represent the current ΔK and crack length. With these values the load can then be calculated using Equations 8 and 9.

The value of C is recommended to be below $-2in^{-1}$ in ASTM E647 [12]. For this material however a value of $-6in^{-1}$ was found to be more suitable, see the Chapter 4 Section 3 for further discussion.

4.3.5 DIC Imagery and Physical Crack Length Measurement

The user is given the choice to capture DIC imagery at every specified increment of crack growth. This option can also be utilised to take measurements of the physical crack length to a high accuracy to confirm BFS crack measurements.

If the user decides to capture imagery they will have the option to collect images at P_{min}, 40% of P_{max}, 60% of P_{max}, 80% of P_{max}, and P_{max} for both the loading and unloading phases of the cycle.

It is likely that over the duration of the test that variances between the BFS and DIC crack length measurements will vary. In this event the material elastic modulus can be varied to bring the two measurements into closer agreement. The elastic modulus need only be changed if the ΔK for the two crack lengths differs by more than 1%. As a general rule, a difference of up to 0.003" is acceptable.

If it is deemed that a correction is to be made the user is given this option at the conclusion of DIC Imagery capture. The new elastic modulus is determined through utilising the "Goal Seek" function in an excel spreadsheet. The spreadsheet and example calculations can be seen in Annex D.

Measurements should also be taken of the rear face of the specimen to ensure agreement between BFS, and DIC measurements and to also ensure a straight crack front.

4.3.6 Closure Measurements

The influence of crack closure is measured periodically throughout the test. Closure is calculated using the compliance offset method described in ASTM E647. For the purposes of ongoing checks during testing the 2% limit at 50% of the applied load is utilised. Full data is captured and stored to enable more in-depth data analysis to be performed at a later time.

CHAPTER 5. RESULTS AND DATA ANALYSIS

5.1 Overview

A total of four ESE(T) specimens were tested throughout the conduct of this research. Two CPLR tests at R=0.1, one CPCA test at R=0.85 and one CPCA test at R=0.85 that suffered an overload of unknown magnitude. Sufficient data was collected from all successful tests to enable data correlations and inferences to be made. All testing was conducted in laboratory air conditions at room temperature.

5.2 Polishing and Speckle Results

On all specimens prepared, both sides were polished. One side was inevitably polished to a higher standard than the other; this became the side that was speckled for the purpose of DIC data collection. The first issue that was encountered was a result of the large specimen size compared to the polishing disc. This generated large torque forces, which could make the sample hard to control and achieve a uniform polish. It was found that this could be largely avoided by ensuring that the polishing pad remained well lubricated with either the silica colloidal polishing solution or water.

It was also found that if the silica colloidal solution, or residue suspended in water, was allowed to sit on the surface of the specimen for more than about ten minutes (i.e. while polishing the reverse side) it would appear to “etch” into the surface of the specimen, see Figure 28. This residue could not be removed by rinsing, sonic cleaning, or by rubbing with a soft cloth. The only way to remove the “etched” residue surface was to polish it out. As such frequent switching of the side being polished was found to avoid this issue.

Once the specimen is suitably polished the speckle manual recommends sonic cleaning [57]. It was found that this would result in damage to the surface. It appeared as if silica colloidal residue would collect on areas of the specimen. Rinsing liberally with running distilled water, and immediately air-drying under compressed air resulted in the best finish surface finish for speckle application.

Speckle application was achieved with no significant issues. As mentioned previously a more uniform speckle was obtained by first passing the particles through a filter pad. Care had to be taken that the filter pad was close enough to the sample for the process to work, but not so close that it touched the specimen and damaged the speckle.

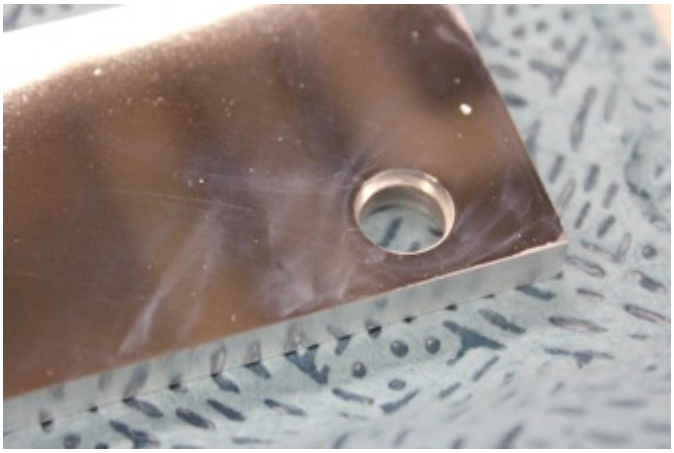

Figure 28. The residue that has been "etched" into the surface can be seen as a blue hue around the pin hole. This can not be removed by rinsing or sonic cleaning.

Although not necessarily an issue, it was difficult to obtain a uniform speckle density between specimens. See figure 29 for an example of differing applied densities. The difference in density did not appear to have an effect on DIC results as discussed in Chapter 6 Section 3.

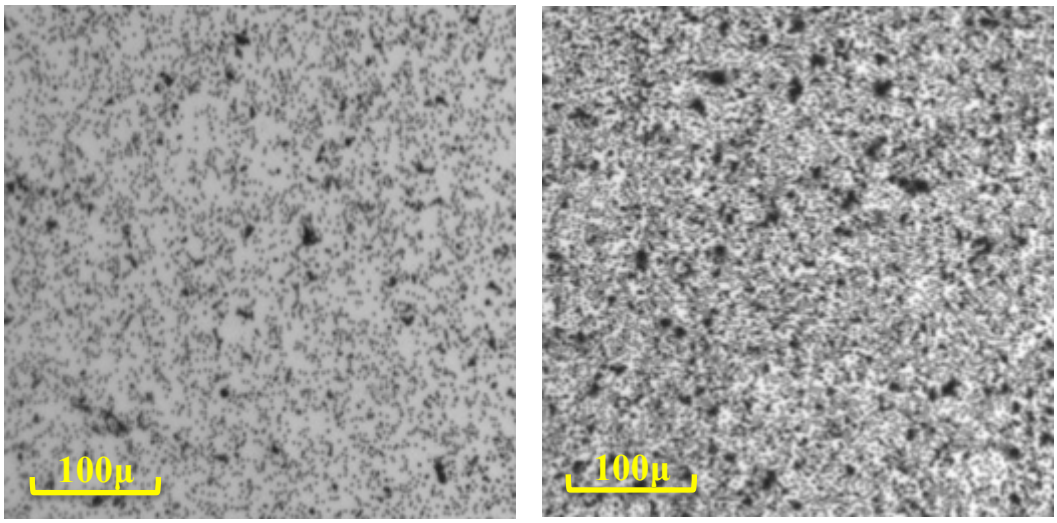

Figure 29. Low density speckle application (left) and high density speckle application (right) both taken at 10x magnification.

5.2 Compression Pre-Cracking Results

The compression-compression phase of pre-cracking occurred with no significant issues. Using Equations 8 and 9 it was determined that the minimum load (based on an initial notch size of 0.5") was -803 lbs. This was rounded down to an even number of -800 lbs. The maximum compressive load was selected as -50lbs. This gives a P_{max}/P_{min} ratio of 16, as described in Equation 12.

Specimen 1 was cycled between the above loads for 30,000 cycles. At this point, no clear indication of a crack was evident. The specimen was cycled for a further 30,000 cycles and a small crack, 0.0018" in length, was evident at this point. The specimen was cycled for further 30,000 cycles with no further crack growth observed.

The remaining specimens were cycled in single blocks at the above compressive loads. Table 3 details the total number of cycles and compressive crack length for each specimen.

Table 3. Compression Pre-Cracking Results

Specimen	Cycles (Total)	Crack Length (inches)
1	90,000	0.0018
2	60,000	0.0017
3	50,000	0.0016
4	50,000	0.0019

These results compare relatively well with Pippan's [59] estimated size of arrested cracks. The relationship developed is given by:

$$a = \frac{1}{5\pi}\left(\frac{\Delta K}{\sigma_{yield}}\right)^2 \tag{17}$$

Although this relationship was developed for an R=∞ load ratio, reasonable correlation can be seen at our load ratio, R=0.0625. Substituting the relevant values into Equation 15 indicates that we should expect an arrested compressive crack of the order of 0.0013". Figure 30 shows a representative arrested compressive crack.

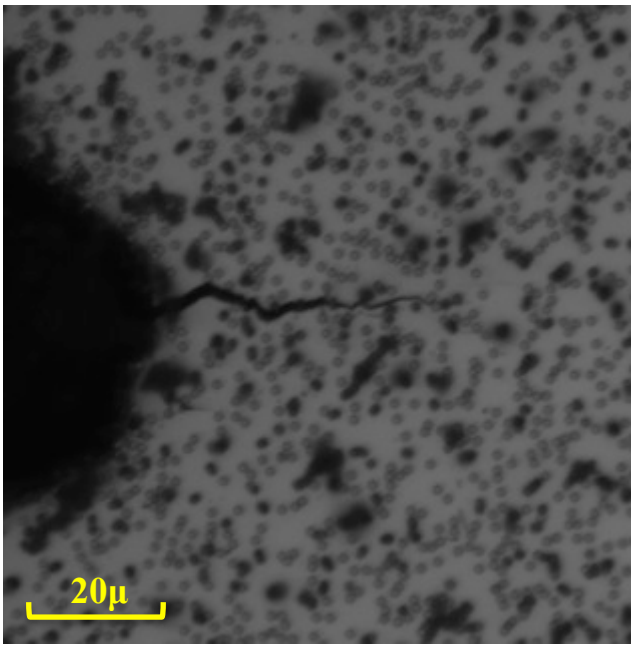

Figure 30. Representative arrested compression-compression pre-crack. Viewed at 20x magnification, crack is approximately 0.0017" in length, note crack is fully open.

5.3 Specimen 1 Results

Specimen 1 was a CPLR, R=0.1 test. It was estimated that an approximate stress intensity to start the ASTM LR test was $\Delta K = 3\ ksi\sqrt{in}$. Using this information and Equation 9 it was determined that for this test $P_{max} = 250\ lbs$. The specimen was then further pre-cracked in tension-tension loading by cycling between 25-250 lbs at 15 Hz for 185,000 cycles. In this time the crack grew to a length of 0.5267". Unfortunately due to a program coding issue no further data was obtained from the pre-cracking.

Once a suitable pre-crack was formed the standard ASTM LR technique utilising $C = -2in^{-1}$ was commenced in order to determine the threshold value. Although loads were decreasing suitably according to Equation 14, the crack length was advancing too rapidly for an accurate determination of a threshold value. At a crack length of 0.891 inches the CPLR phase of the test was stopped. The CPCA component was then commenced at a $P_{max} = 75lbs$, approximately 10% higher than the last CPLR P_{max} in order to avoid the effects of closure that had become evident.

Figure 31 shows the raw crack length (a) vs. cycle (N) data for specimen 1. The small dip in the curve at approximately 12,500 cycles is due to an adjustment in the elastic modulus to bring observed crack length measurements and BFS measurements into agreement. For the remainder of the test the values remained within acceptable limits with only a few minor modifications being made. The sharp rise in the data around 5,000,000 cycles represents the change from CPLR to CPCA testing. A total of 8,350,670 cycles were applied to this specimen prior to fracture.

Although the program was automated to calculate the crack growth rate and SIF, the corresponding crack length and P_{max} were mistakenly not recorded. This oversight proved problematic in determining the ΔK_{eff} curve. As such the raw a vs. N data was utilised as Equation 14 would permit the calculation of P_{max}. Recorded data of visual measurements of crack length (which also recorded P_{max}) showed good agreement with the estimated P_{max}, being within $\pm 2lbs$ of the recorded values. Figure 32 contains the da/dN vs ΔK curve for specimen 1. The CPLR (blue) and CPCA (orange) components have been divided for ease of distinction.

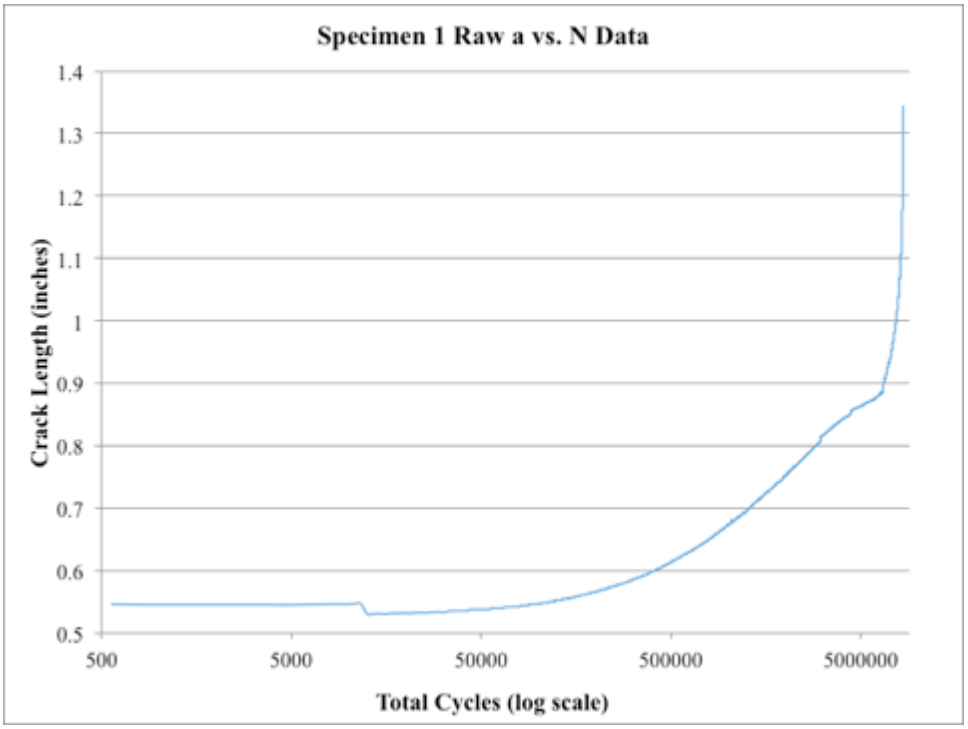

Figure 31. Crack length vs. cycle data for specimen 1.

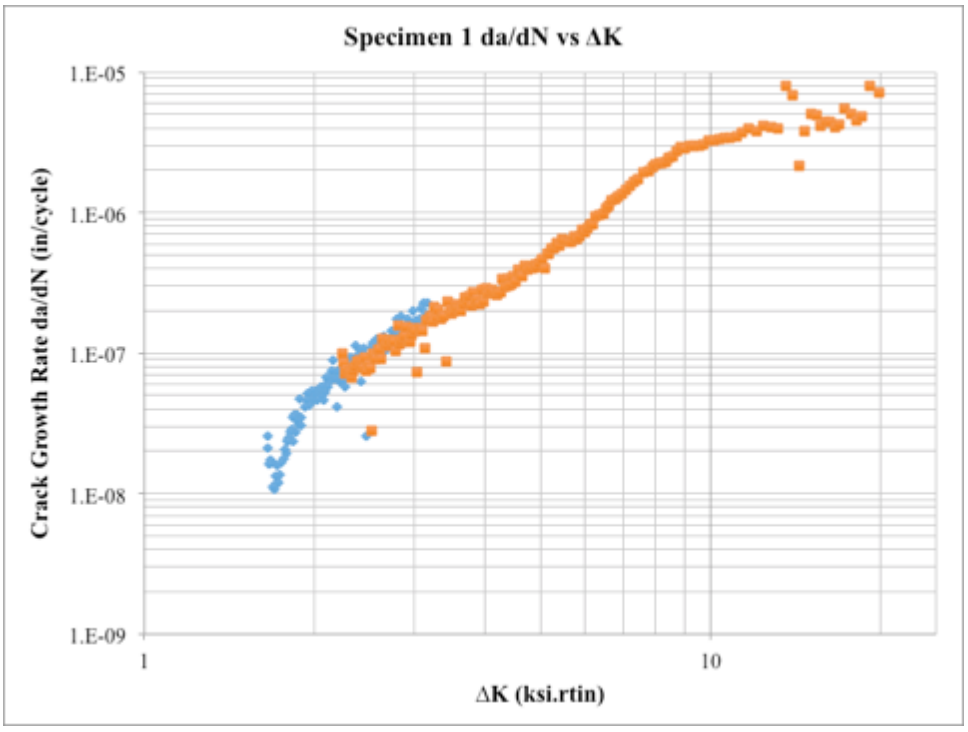

Figure 32. Specimen 1 da/dN vs Δ*K* curve curve. The blue data represents the CPLR phase of the test and the orange data points the CPCA phase of the test.

We can see in Figure 32 that there is a good correlation in the overlap of the CPCA and CPLR curves. There is a slight degree of increased scatter as the data approaches lower crack growth rates. Of particular note are the few points in the CPCA curve that drop significantly lower than the rest of the data. It is possible that these points are due to the effect of some form of microstructural feature and are discussed in more detail in Chapter 6. Also of note in the threshold region are the last seven data points that have inverted and started a trend upwards. That is, although we are continuing to decrease P_{max} the crack continues to speed up. In the fracture region we can also see quite a degree of scatter in the results, possibly due to a transition from intergranular to transgranular cracking, this will be discussed in more detail in Chapter 6.

Closure data was obtained that allowed the crack opening load to be determined using the offset method detailed in ASTM E647. With this information the ΔK_{eff} curve can be determined. Figure 33 shows the ΔK_{eff} curve with the standard ΔK curve. The ΔK_{eff} curve was determined using a 2% offset criterion [12]. Figure 34 shows the normalized change in crack opening load with change in crack length. Relatively high levels of closure were obtained for this specimen. However other research has shown that extremely high levels of closure can occur [61].

In Figure 34 we can see a slow, steady rise in the opening load as we conduct the CPLR phase of testing. This slow rise corresponds well to the slow move into the threshold region as shown in Figure 32. At $\alpha = 0.58$ there is an apparent discontinuity in the data, this corresponds to the transition from CPLR to CPCA loading. During the CPCA phase of loading we see a steady overall trend of decreasing closure as the back surface of the specimen is approached (in a wider specimen this may not be as evident). At $\alpha = 0.65$, we see a rapid increase in closure, followed by a sharp drop. Analysis of DIC images revealed a increased crack roughness in the region, which may be responsible for this effect. This is discussed in more detail in Chapter 6.

The published value of K_{IC} was not observed in this case. The value obtained in this test was $25\ ksi\sqrt{in}$ compared to the published value of $31\ ksi\sqrt{in}$. The difference here is believed to be a result of the specimens used to obtain the published value. Thick forgings 1”-2” thick were used compared to the 0.25” specimens used in this research.

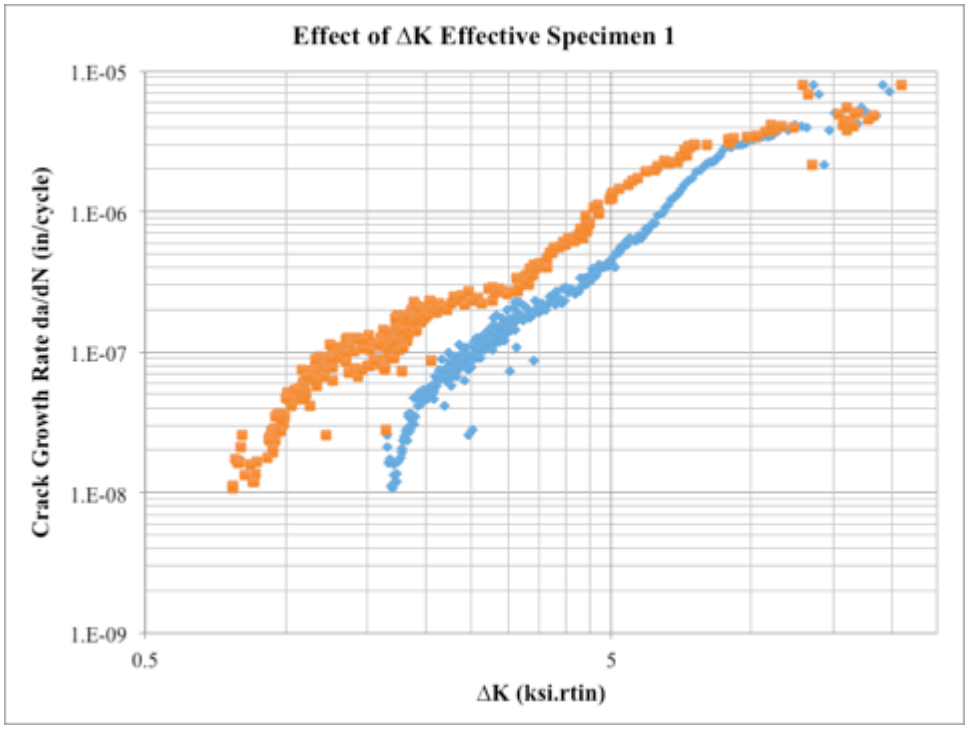

Figure 33. Plot showing the effect of ΔK_{eff}, that is the effect of closure, raw data is represented in blue, and corrected data in orange.

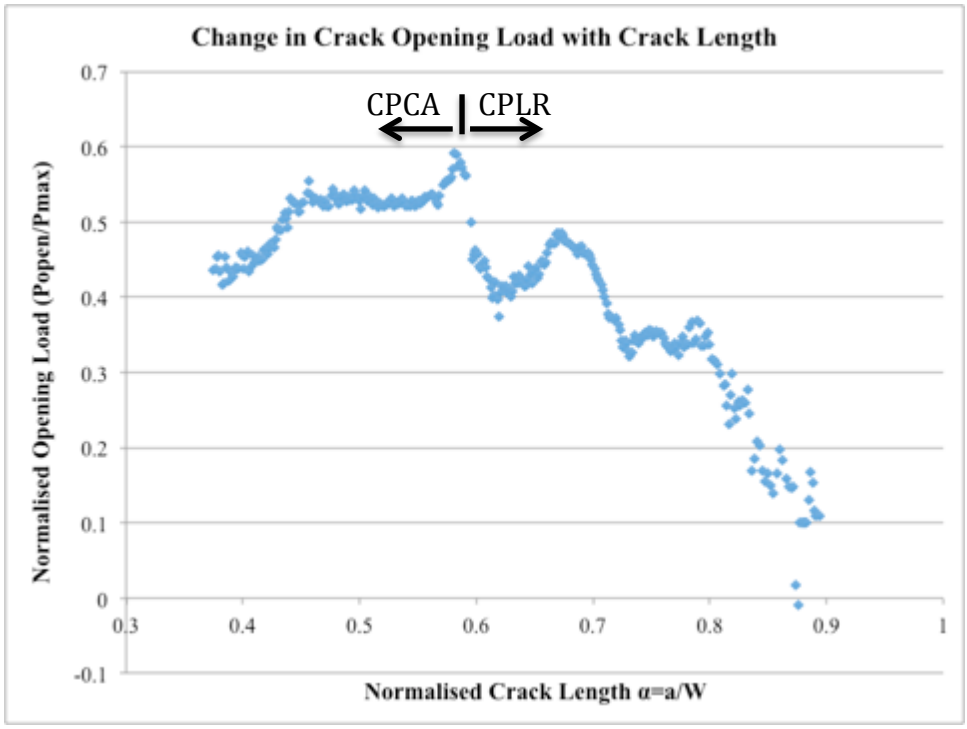

Figure 34. Change in closure with change crack length.

5.3 Specimen 2 Results

Specimen 2 was also a CPLR, R=0.1 test. Based upon the results of specimen 1 and the failure to adequately define a threshold, a number of modifications were made to the procedure.

The first change was a decrease in the C value from $-2in^{-1}$ to $-6in^{-1}$. This modification was intended to drive the load down significantly faster than the rise in SIF due to crack extension.

The second change was to start the test at $\Delta K = 2.2ksi\sqrt{in}$. This modification was intended to reduce the amount of crack extension required to determine a threshold value.

The third change was a modification of the code to record crack length and cycle count at the calculation of da/dN, ΔK and closure, which allows much simpler interpretation of the obtained data.

These modifications result in some slight changes to the tension-tension pre-cracking. In the case of Specimen 2 it was determined $P_{max} = 160lbs$. As with Specimen 1, the pre-cracking growth data was not recorded. It was observed however that the crack grew to a length of 0.528 inches over a period of 700,000 cycles.

At this point the standard ASTM LR procedure was started. A threshold was rapidly identified and the CPCA loading portion of the test was begun. These results would indicate that this is the maximum rate to be applied in order to still maintain five data points per decade of crack growth in accordance with ASTM E647 [12]. Based upon the fracture of specimen 1, the test was halted at $\Delta K = 18.2\ ksi\sqrt{in}$. Figure 35 shows the raw a vs. N data for specimen 2. This data is very typical of a fatigue crack growth test. The change to CPCA loading occurred at roughly 3 million cycles. A total of 15.2 million cycles were applied to specimen 2. Figure 36 shows the da/dN vs ΔK curve for specimen 2. The CPLR (blue) and CPCA (orange) components have been divided for ease of distinction.

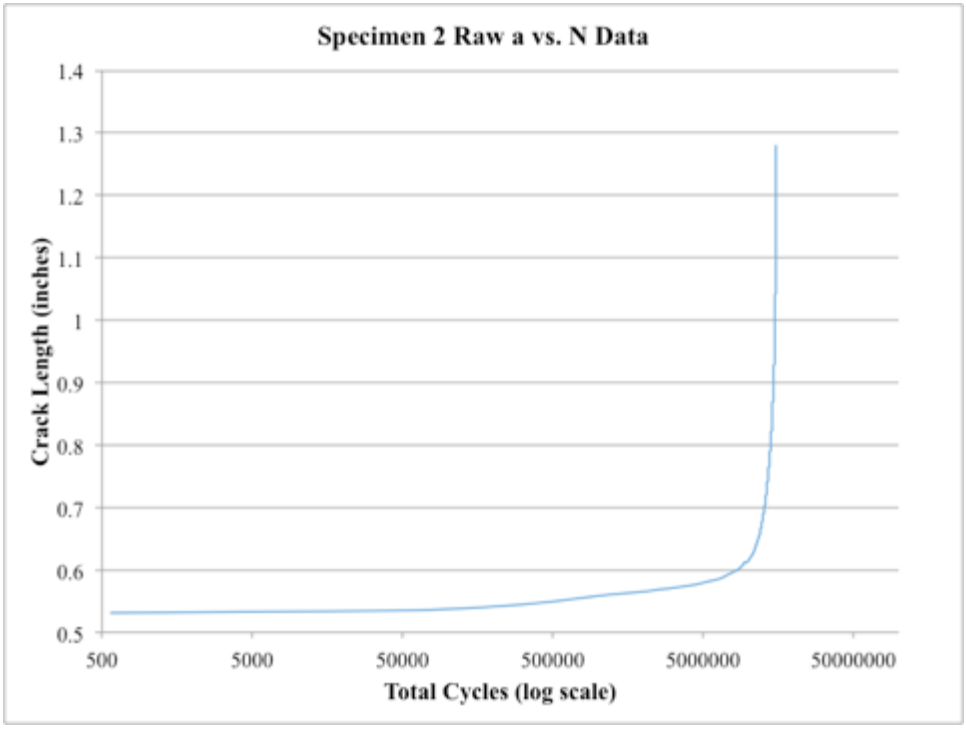

Figure 35. Crack length vs. cycle data for specimen 1

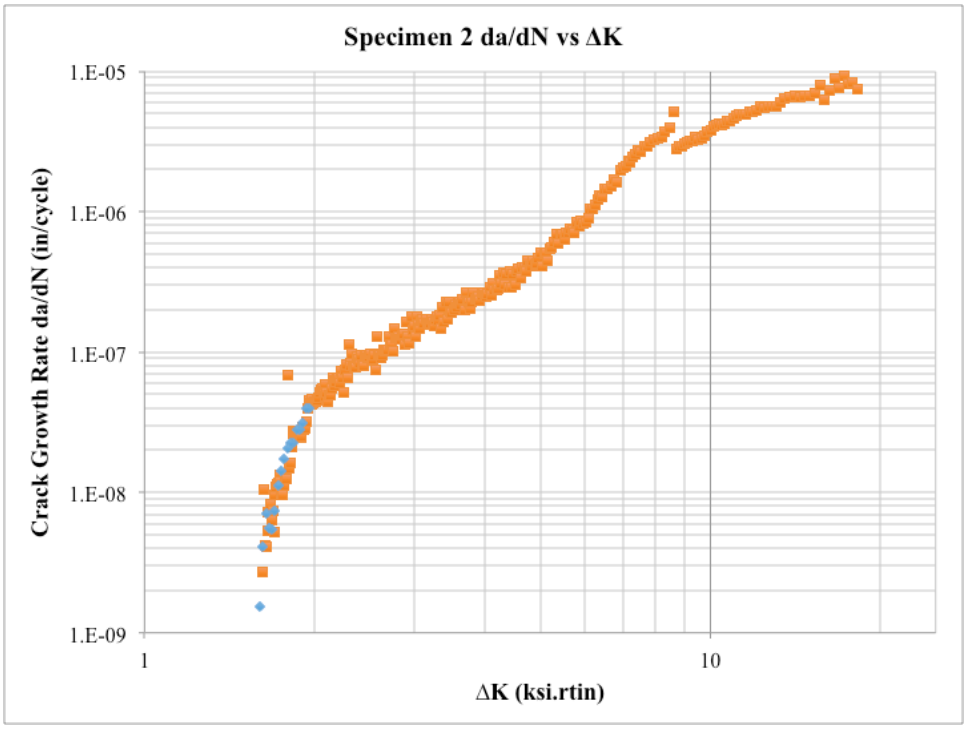

Figure 36. Specimen 2 da/dN vs $\boldsymbol{\Delta K}$ curve curve. The blue data represents the CPLR phase of the test and the orange data points the CPCA phase of the test.

In Figure 36 we can see once again that there is very close agreement between the CPLR and CPCA phases of the test. For specimen 2 we see a significantly increased overlap of the data, leading to further confidence in our data and process.

Due to the threefold decrease in our C value we see significantly less scatter in our results in the threshold region compared to specimen 1. We also see the establishment of a firm threshold well below the ASTM defined threshold.

As with specimen 1, we see an increase in scatter in the fracture region, though of a much decreased degree. Interestingly there appears to be a discontinuity in the data in the steady state region. No adjustments were made to the setup at any point during this time. There is a smooth departure from the established curve and does not appear to a result of transient effects. As a result it would seem as if some sort of material influence caused this discontinuity. Analysis of the DIC imagery of the crack at this point has not revealed any obvious cause for this data. This will be discussed in further detail in Chapter 6. After this small region though the data returns to the steady state and there are no further deviations.

As with specimen 1, the recording of closure data enables the calculation of ΔK_{eff}. Figure 37 shows the da/dN vs ΔK and the ΔK_{eff} curve. Figure 38 shows the change in opening load for increase in crack length.

As with specimen 1 the normalized crack opening load vs. the crack extension is plotted. In Figure 38, although it is a difficult to directly identify, there is a sharp increase in opening load corresponding to our CPLR phase of testing. In the CPCA phase of testing we see a very stable decrease in crack opening load up until about $\alpha = 0.65$. At this point there is a steady and sharp increase in opening load before it decrease again and returns to same steady state curve. There is no indication in the crack growth data of what this might be attributable to. The discontinuity previously mentioned in the da/dN vs ΔK occurs at $\alpha = 0.77$.

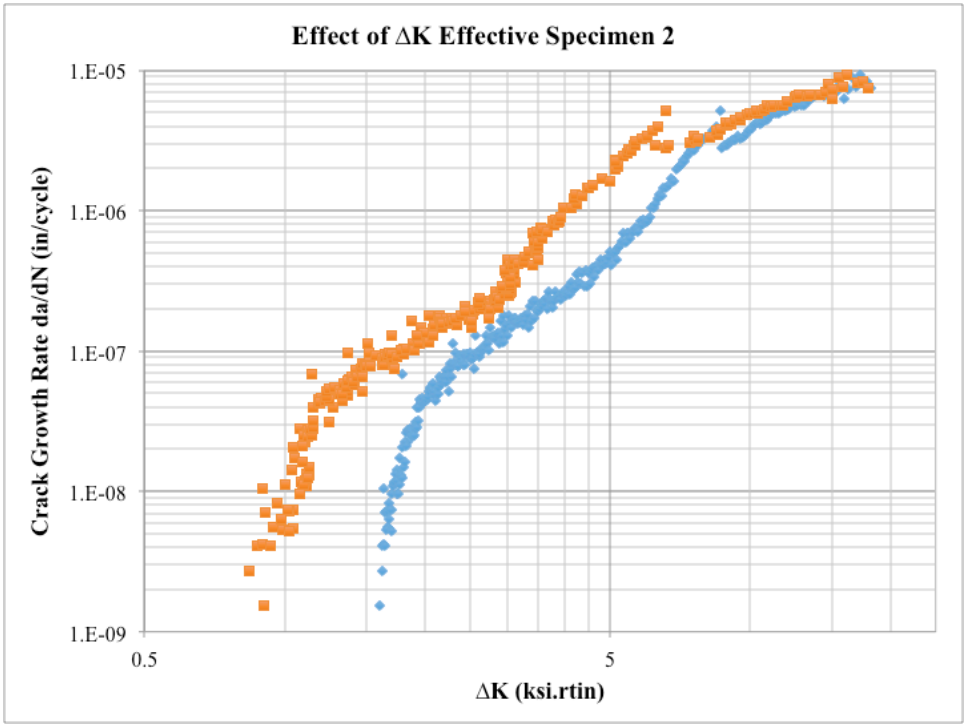

Figure 37. Plot showing the effect of ΔK_{eff}, that is the effect of closure, raw data is represented in blue, and corrected data in orange..

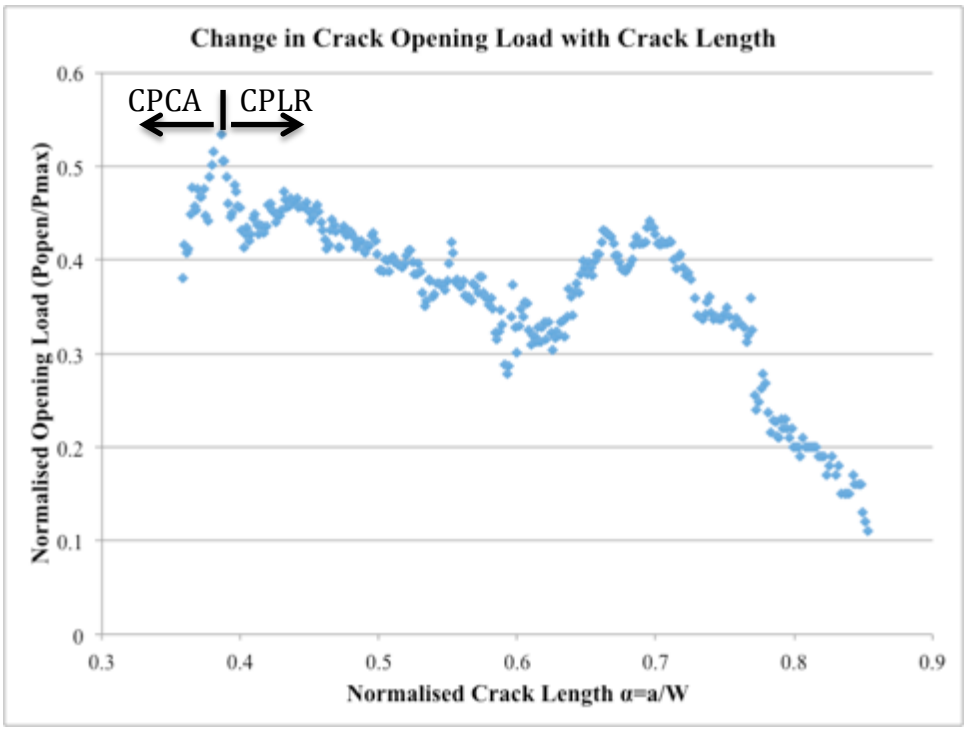

Figure 38. Change in closure with change crack length.

5.4 Specimen 3 Results

Specimen 3 was to be a CPCA R=0.85, CPCA test as outlined in ASTM E647. After being pre-cracked in compression it was necessary to determine the load at which crack extension would occur. In this process an initial $P_{max} = 300lbs$ was selected. The sample was then cycled in tension-tension at 15Hz for 400000 cycles. During this time the crack length was monitored every 1000 cycles. If there was no clear trend of growth in the data and a visible extension of the crack, the load was increased by 10% and the process repeated. It was found during this process that crack extension first occurred at $P_{max} = 500lbs$.

Unfortunately after about 0.002 inches of crack extension the specimen suffered an overload of unknown magnitude due to hydraulic pump failure. It was later determined that the pump over heated and automatically shutdown due to water supply issues.

The recorded data gave no indication of any magnitude of overload. During restart of the pump, the load was carefully controlled and there were no indications of any overload.

Observation of the crack tip using the DIC camera revealed that the existing crack was in a fully opened position, indicating significant residual stresses in the area. The entire crack can be observed to be completely open. Emanating from the crack tip at roughly 45° angles were two cracks. Figure 39 shows this detail.

The sample was cycled at R=0.85, $P_{max} = 500lbs$ for a further 2.5 million cycles with no evidence of any crack growth. The sample was removed and stored in an airtight container for later testing if possible.

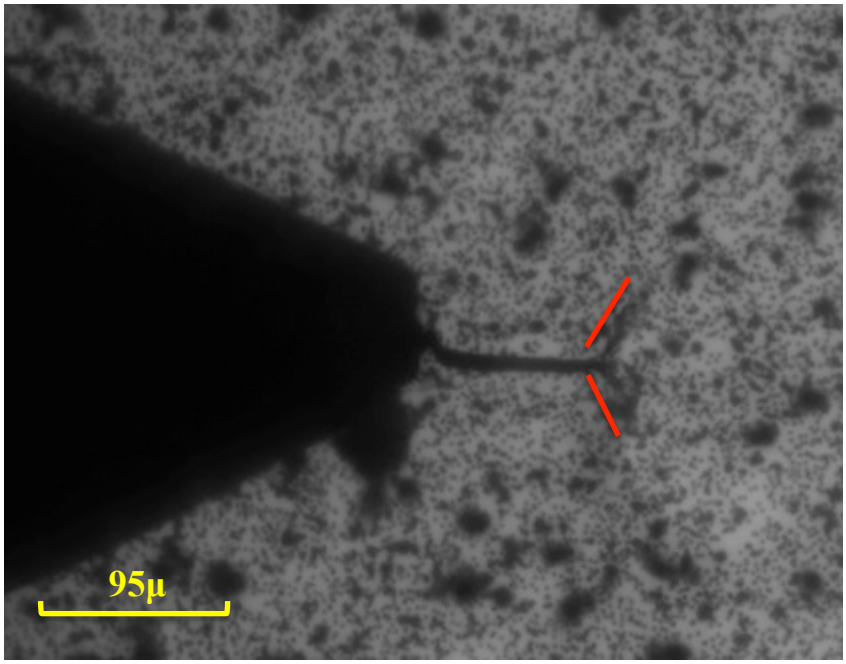

Figure 39. Image of the overloaded crack. Note the 45 degree slip bands emanating from the crack tip, shown with red lines.

5.5 Specimen 4 Results

Specimen 4 is a replacement for specimen 3 that was damaged during testing. As outlined above the test CPCA R=0.85 as outlined in ASTM E647. Due to the knowledge gained from the specimen 3 initial loading was begun at $P_{max} = 440lbs$. Crack extension was observed to occur at $P_{max} = 485lbs$. Initial crack growth was of the order 1.5×10^{-9} in/cycle.

Figure 40 contains the raw a vs. N data for specimen 4. Figure 41 contains the da/dN vs ΔK curve. Considering the high load ratio, closure is generally not an issue. Closure data however, was obtained and analysed. It showed that the crack was fully by about 1% of the maximum load, which is likely due to calculation and rounding errors. As such a closure effect and ΔK_{eff} curve will not be presented for this specimen. A total of 22.6 million cycles were applied to the specimen.

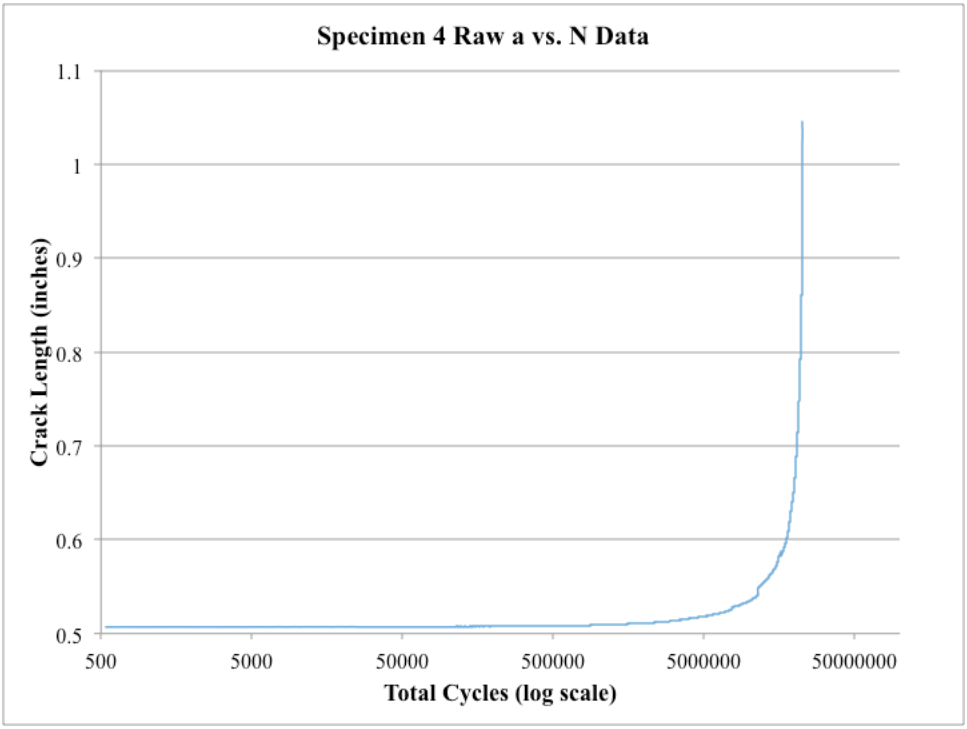

Figure 40. Crack length vs. cycle data for specimen 4.

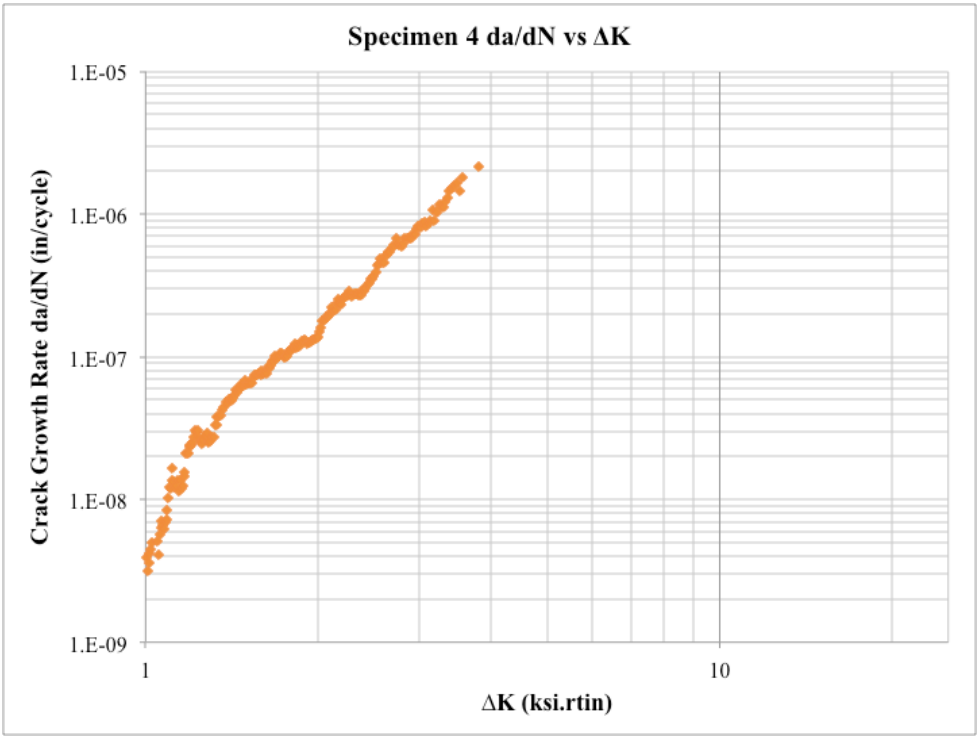

Figure 41. Specimen 4 da/dN vs $\boldsymbol{\Delta K}$ curve curve.

Just after the specimen has passed the crack extension criteria a hydraulic pump failure due to severe electrical storms was experienced. After this pump failure the specimen was unloaded to facilitate application of hydraulic power. After hydraulic power was returned the specimen was returned to testing. It was unsure at this point if the specimen had been subjected to an overload during the pump failure. Crack length data was analysed over the next several hours and a definite growth trend was observed. Interestingly a few hours into the test there was a jump in crack length with no observable difference seen on DIC imagery. Some hours later there was once again a definite decrease in crack growth rate observed before it returned to the previous steady state value from the beginning of the test. During this time there were no observable causes for this change in rate obtained by DIC imagery.

It is hypothesized that these observations are due to a change in the plastic zone size. At R=0.85, the plastic zone is, using Equation 4, estimated to be about 0.00004" in radius. While an estimated single cycle of R=0.1 (due to reloading of sample) has a plastic zone radius of 0.0014". The major change in crack growth rate corresponds roughly with an exit from the plastically affected zone as a result of the R=0.1 loading. Figure 42 below details this period of crack growth for specimen 4.

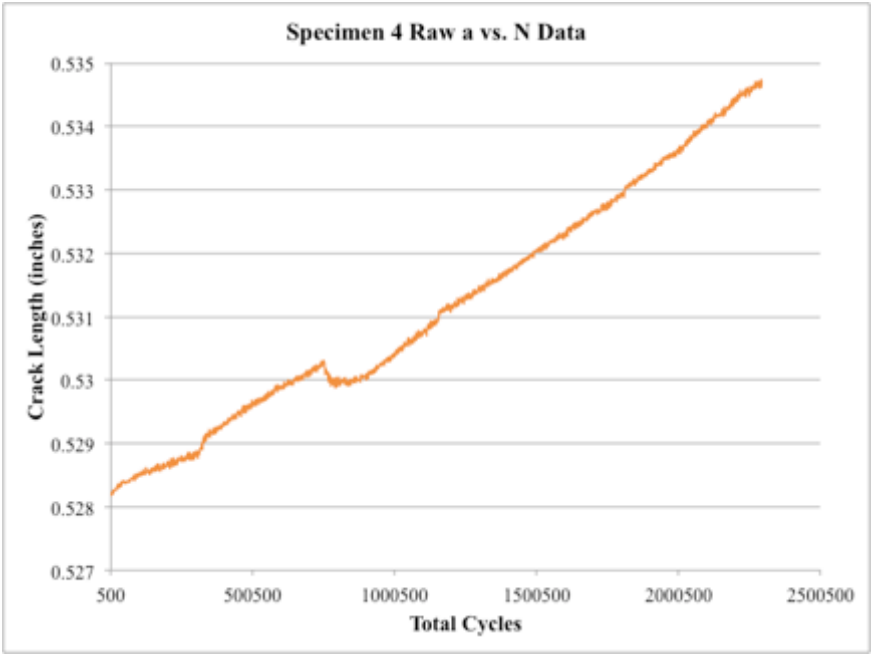

Figure 42. Suspected period of growth through plastically affected zone.

Overall the growth trend for specimen 4 appeared quite stable throughout the entire test. Once the sample passed the first knee, crack growth occurred rapidly. In this sample it ws observed that the sample failed and fracture occurred about 0.2" prior to the other specimens due to the high load ratio. In this test the fracture toughness was calculated to be 25.4 $ksi\sqrt{in}$ which is in agreement with specimen 1, though still different from the published data.

5.6 Consolidated Data

Figure 43 below shows a consolidated da/dN vs ΔK curve for all tests conducted. The data in Figure 43 shows very close agreement for the two R=0.1 CPLR tests. The R=0.85 test follows the trend also.

The data in Figure 44 detailing closure corrected data shows that there is a degree of correlation between the two tests. Ideally these two tests should have collapsed onto each other once closure had been accounted for. There may be some potential issues with the way in which closure opening levels are determined. The R=085 test fits the trend well, particularly in the lower crack lengths. At higher crack lengths, much faster, albeit stable, crack growth rates were observed.

The data obtained has been consolidated in Table 4 below. For each successful specimen the load ratio and type of loading is recorded. The values for a Paris fit of data in the linear region is also recorded as well as threshold versions for both raw and corrected data. The corrected data shows a good correlation between the fit coefficients for the Paris region. The values determined for ΔK_{th} also agree well and would indicate that this material has a $\Delta K_{th} = 0.92\ ksi\sqrt{in}$.

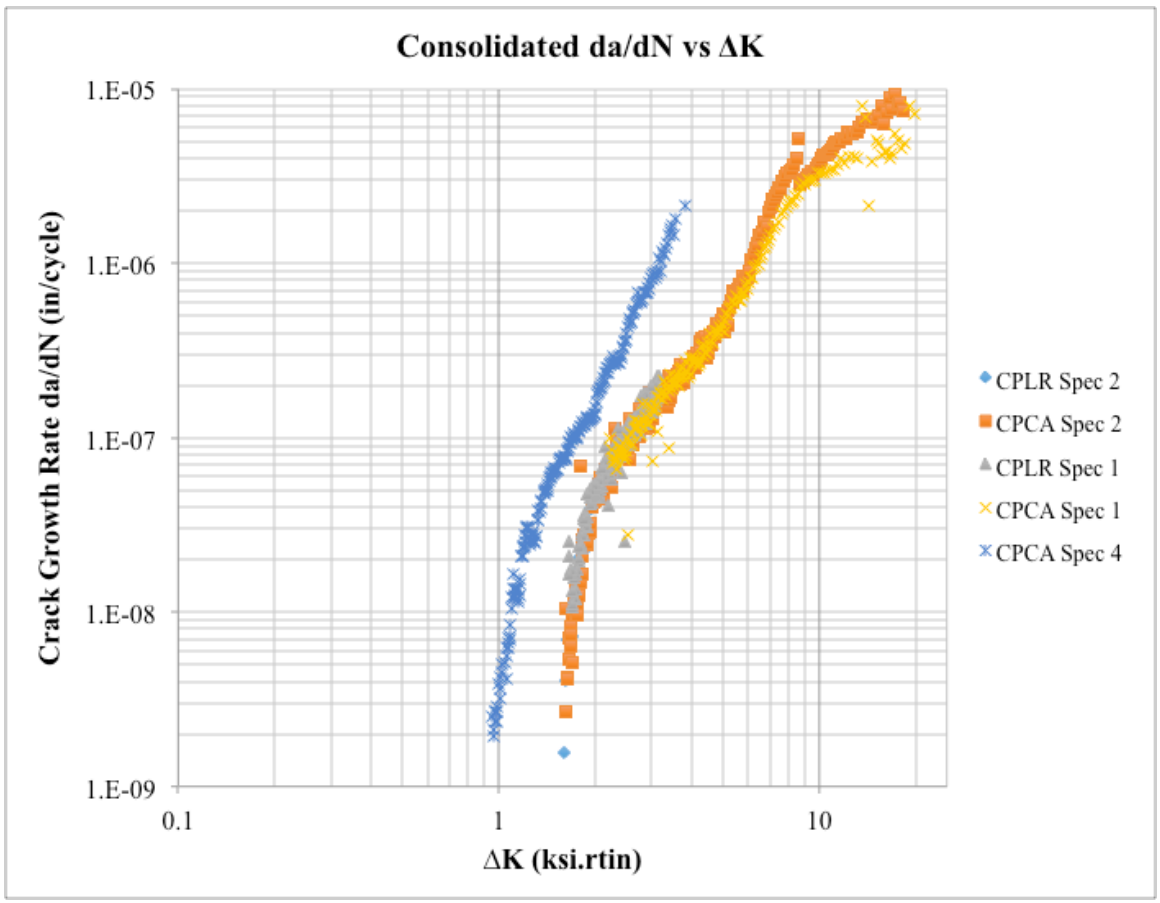

Figure 43. Consolidated fatigue crack growth data for all specimens.

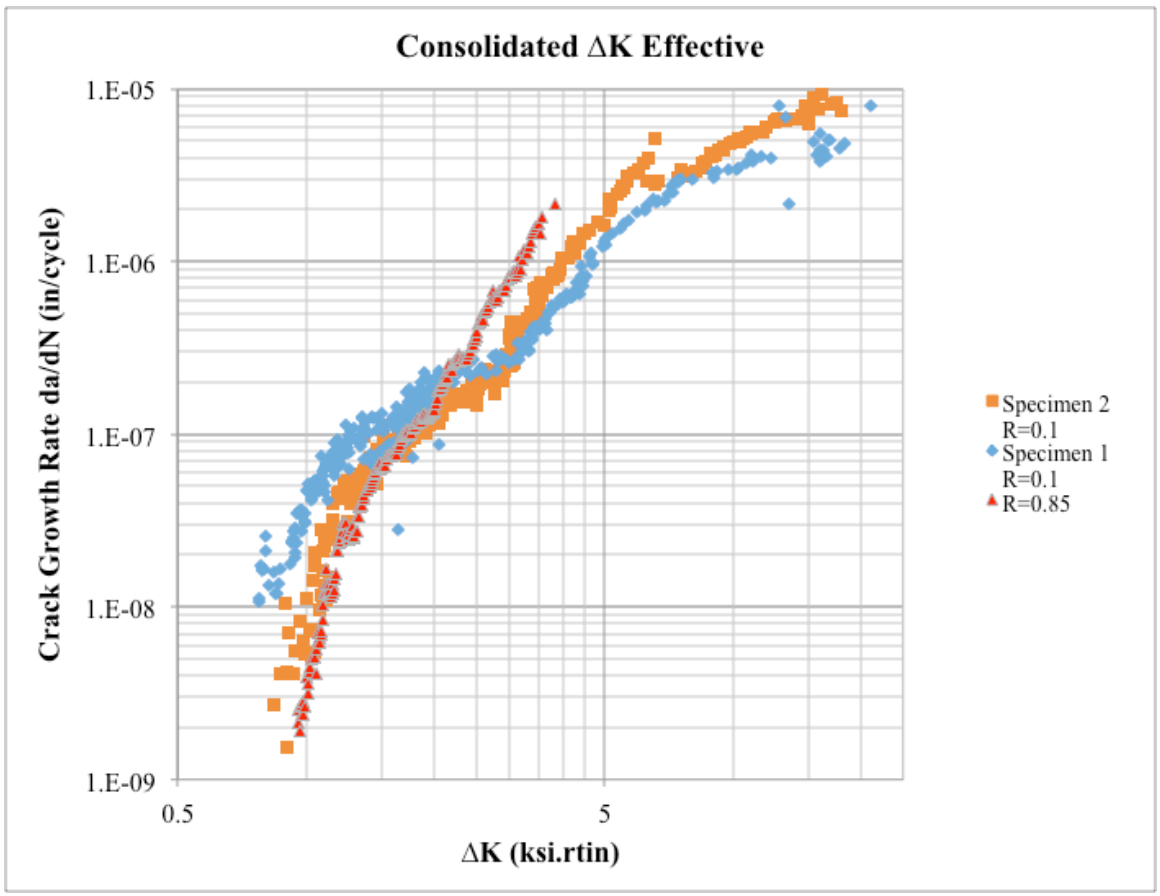

Figure 44. Collapsed ΔK_{eff} data.

Table 4. Consolidated Data for Tests Completed

Data Summary								
			Raw Data (ΔK)			**Corrected Data (ΔK_{eff})**		
Spec	**R**	**Loading**	**C**	**m**	ΔK_{th} $(ksi\sqrt{in})$	**C**	**m**	ΔK_{th} $(ksi\sqrt{in})$
1	0.1	CPLR/CPCA	9.74e-9	2.44	1.72 (est)	4.97e-8	1.71	0.91 (est)
2	0.1	CPLR/CPCA	1.01e-8	2.38	1.62	3.37e-8	1.92	0.89
4	0.85	CPCA	1.24e-8	3.82	0.95	1.24e-8	3.82	0.95

CHAPTER 6. DIC RESULTS

6.1 Overview

The use of the DIC camera provided a high fidelity method with which to monitor and observe crack growth through the various stages. The imagery has provided a valuable means with which to explain and correlate fatigue crack growth rates and closure measurements. The DIC technique has also enabled visualization of the strain fields around the crack tip.

6.2 Crack Features

6.2.1 Specimen 1

The first interesting feature observed in the DIC imagery for specimen 1 was the crack path at around $\alpha = 0.56$. This corresponds to the region in which the lowest loads were being applied and the closure effects were near their peak value. In this region, it was observed that the crack path took a "wave-like" or saw-tooth path, see Figure 45. This crack path, with the increased roughness/tortuosity explains the rise in the closure levels and is a good example of roughness-induced closure. Once a period of CPCA loading had been applied a much more stable and straight crack front had developed.

Secondly as noted in Figure 35 there was an increase in the crack opening load at approximately $\alpha = 0.65$. As can be seen in Figure 46, which corresponds to $\alpha = 0.69$, there is a defined saw-tooth nature of the crack path. It is possible that this contributed to the observed rise in closure load. Unfortunately subsequent images were not obtained as failure occurred rapidly. It would be expected that a more stable crack path would have been established past this zone.

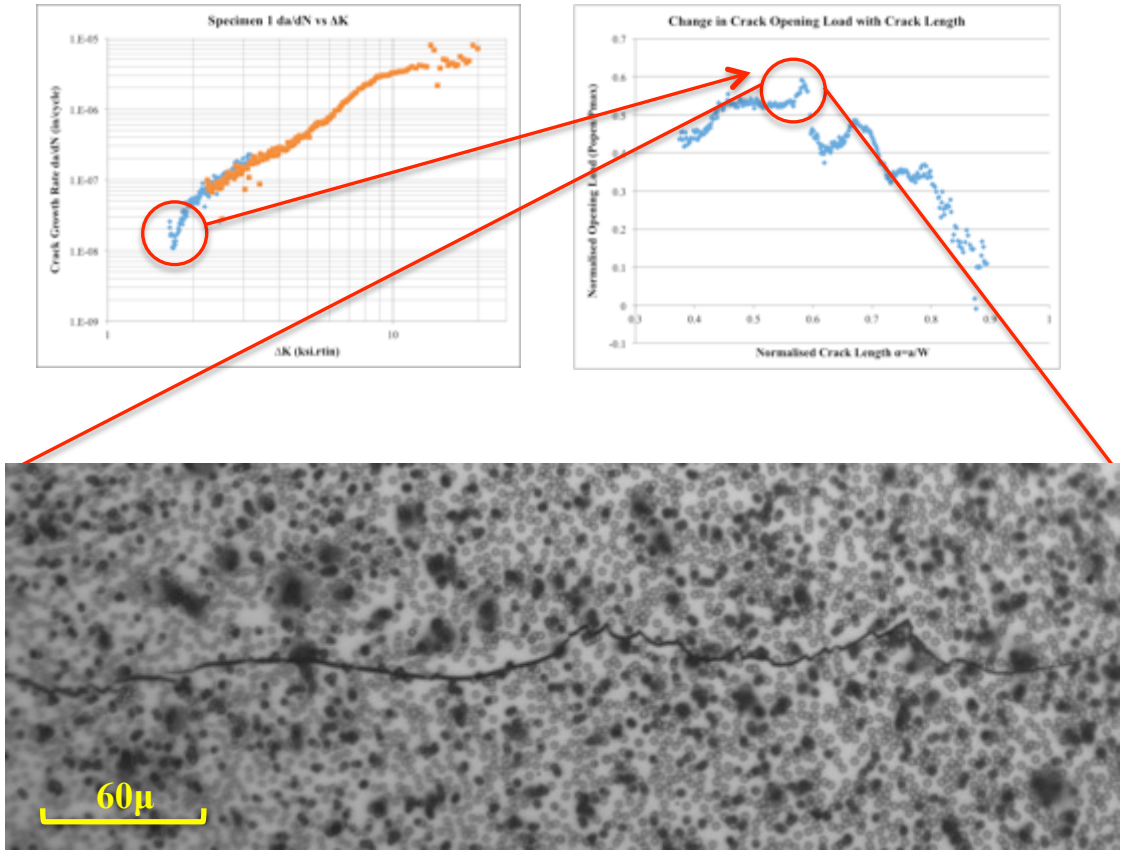

Figure 45. Increased surface roughness corresponding to a rise in closure. Viewed at 20x magnification.

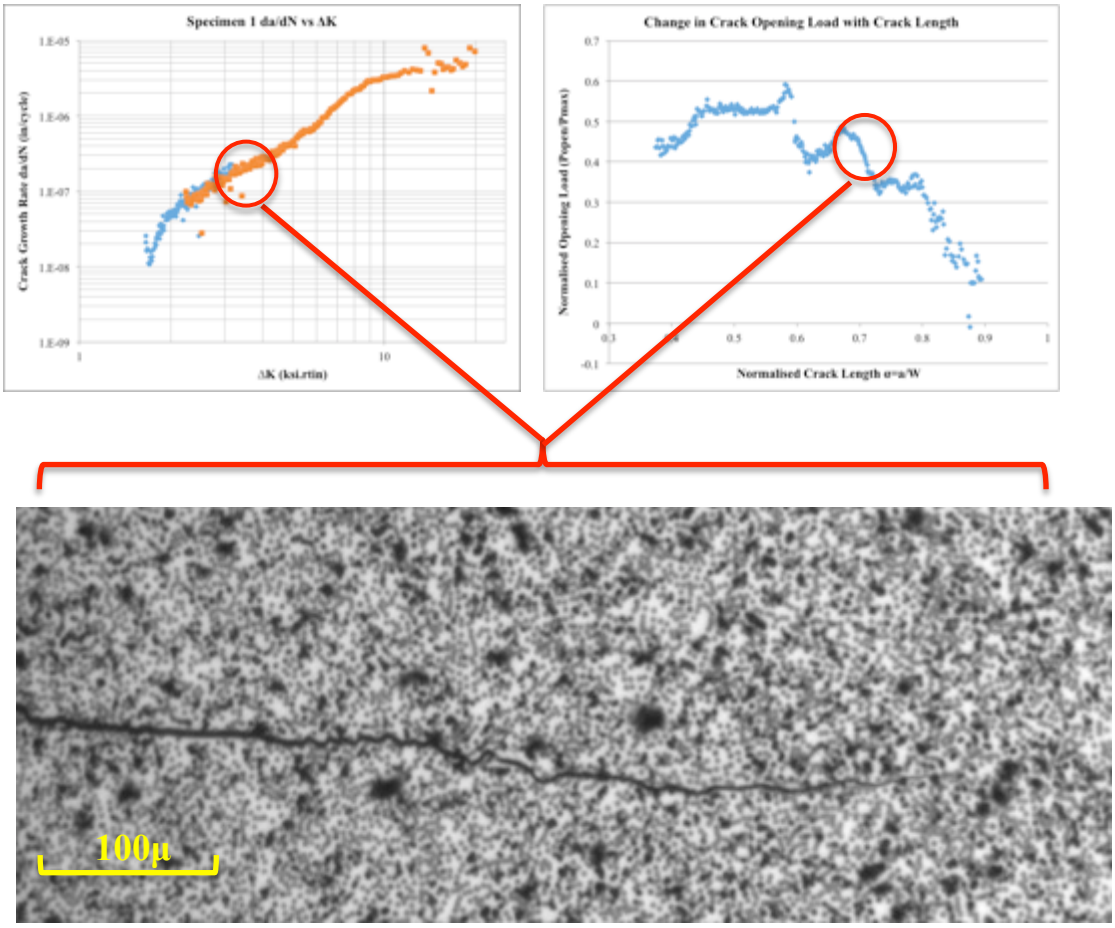

Figure 46. Region of more stabilized crack growth once the sample had entered the CPCA loading region, tortuosity contributing to closure still evident. Viewed at 10x magnification.

6.2.2 Specimen 2

As previously noted there is definite discontinuity in the crack growth data shown in Figure 37. The region leading up to and containing this discontinuity is bounded by $\alpha = 0.71$ and $\alpha = 0.77$. Analysis of the crack images show no regions of interest or features which might have been attributed to this rise in crack growth, see Figure 47. The change in crack growth was previously attributed to a potential change from intergranular to transgranular crack growth. This does not seem to be the case, as Figure 48 shows there still seems to be a significant degree of intergranular crack growth at larger crack lengths.

As with specimen 1 there was a noted rise in closure at one point during the test. Analysis of the crack images show regions of increased surface roughness and tortuosity, which may be attributable to the rise in closure observed, see Figure 49.

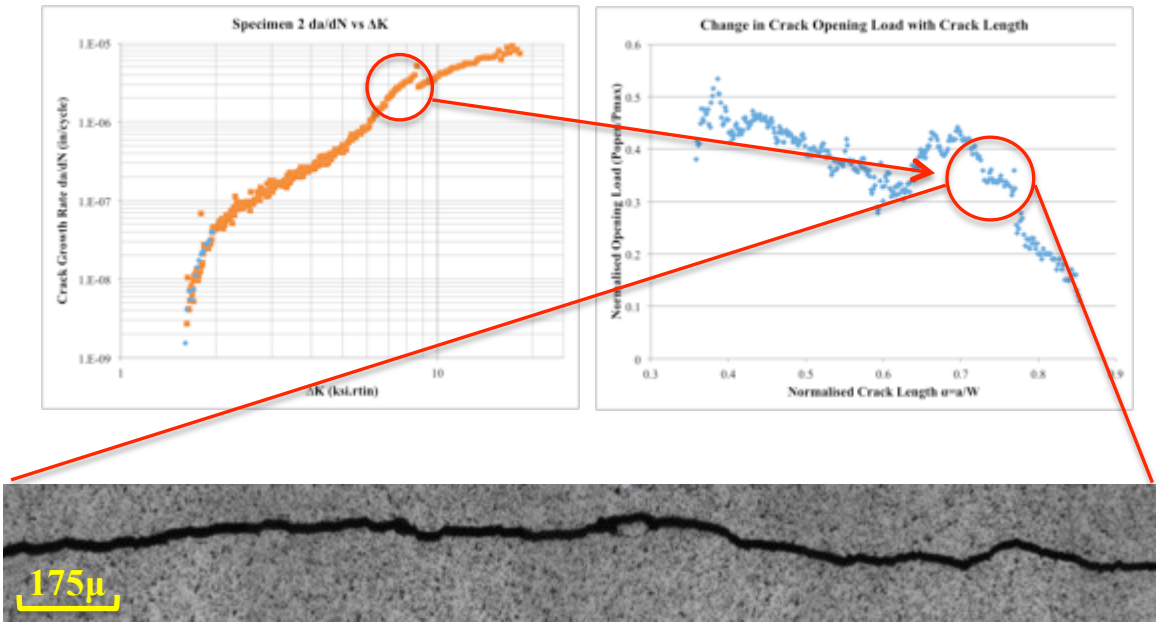

Figure 47. Crack region corresponding to the discontinuity observed in the crack growth data. Viewed at 10x magnification.

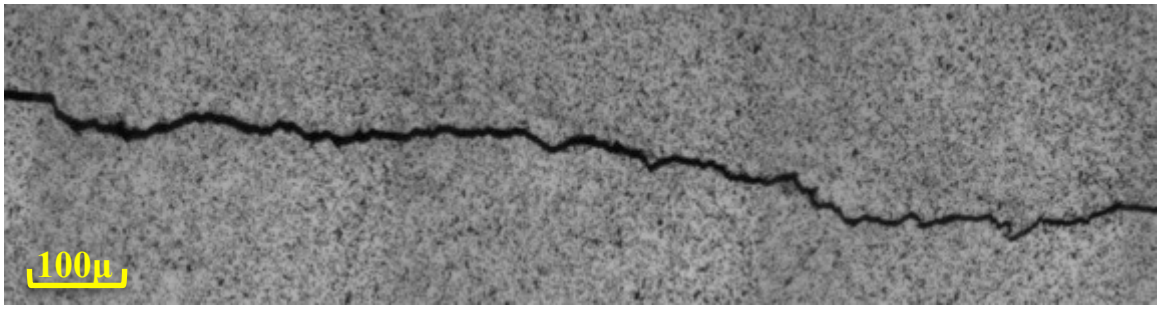

Figure 48. Crack region past the discontinuity. It is very evident in this figure that intergranular cracking is still the primary method of crack propagation. Viewed at 10x magnification.

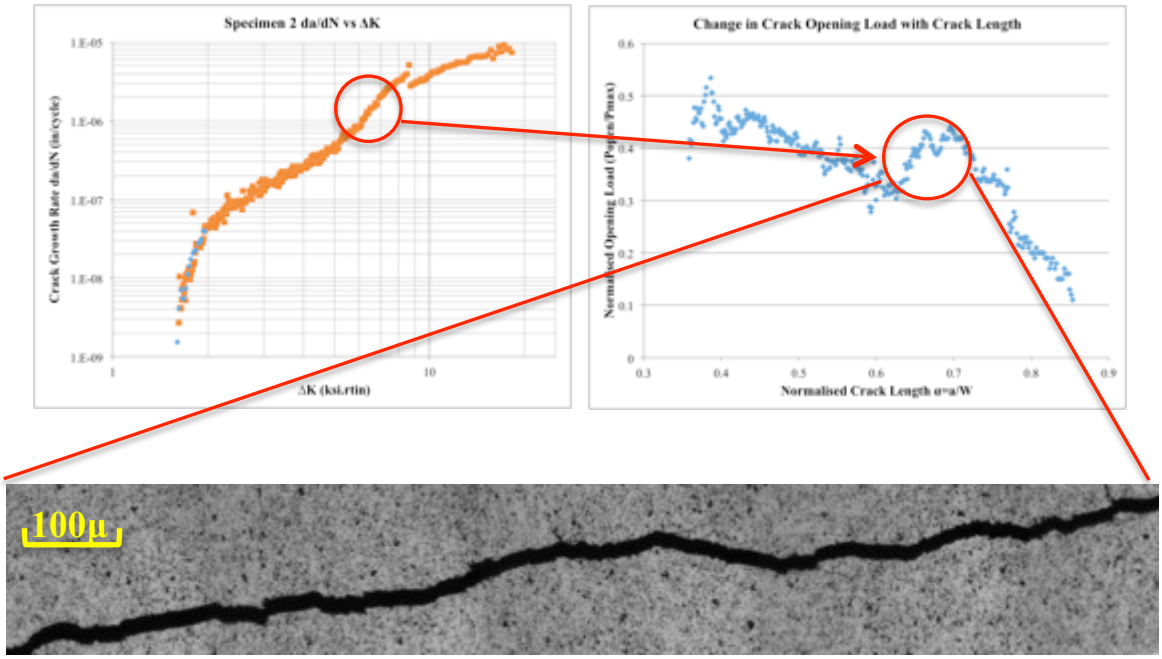

Figure 49. Crack region corresponding to the rise in closure. Some jagged crack surfaces are evident here and likely contributed to the observed rise in closure. Viewed at 10x magnification

6.2.4 Specimen 4

The crack images obtained for the R=0.85 test show a relatively stable and straight crack. There is very little evidence of roughness of surface and tortuosity as was evident in tests at lower load ratios. Cracks propagating at the lower load ratios were noticed to exhibit a range of crack branching (discussed in the next section), particularly at low crack lengths. In the high load ratio test this crack branching was also observed. Figure 50 shows a stable crack at R=0.85, $P_{max} = 485lbs$ at a crack length of about 0.535 inches.

It was also noted during the testing that when crack branching was evident there was an associated change in crack growth rate (although not observable on the plots). It was noted through observation of the time between crack increments. It was observed that in the region before crack branching the increments were occurring roughly every 2.5 hours. This time would suddenly jump to 3 hours, with crack branching evident in DIC imagery.

In the region once the dominant crack had established itself the increments would then rapidly approach the previous 2.5 hour rate.

There are no real features of note in the data with the exception of the inflection in the crack growth rate about half way through the data. No changes were made to the test during this time. DIC imagery was not captured in this region, it is therefore not possible to determine the cause.

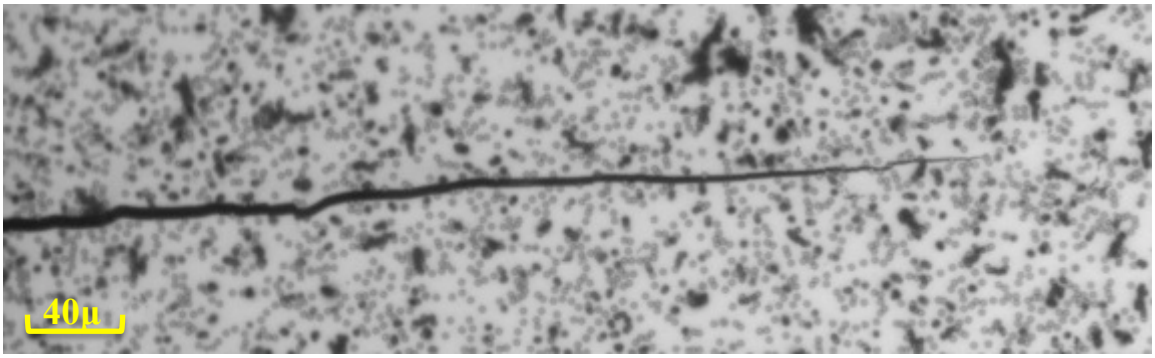

Figure 50. Stable fatigue crack growth at R=0.85 and a crack length of 0.535 inches.

6.2.5 Other Crack Features

Throughout testing the DIC camera allowed capture of a range of other crack features, which may be of interest in future work where strain fields will be more closely analyzed. Figure 51 contains a parallel crack, which appears to have developed on each side of a material grain. As the test progressed one side became the dominant crack.

Figure 52 contains a similar situation as Figure 51, except in this image there are a number of independent crack paths. As the test progresses one of these cracks becomes the dominant path and the remainder arrest.

These types of crack features were observed in the R=0.1 tests and generally at smaller crack lengths. These features were also observed in the R=0.85 test.

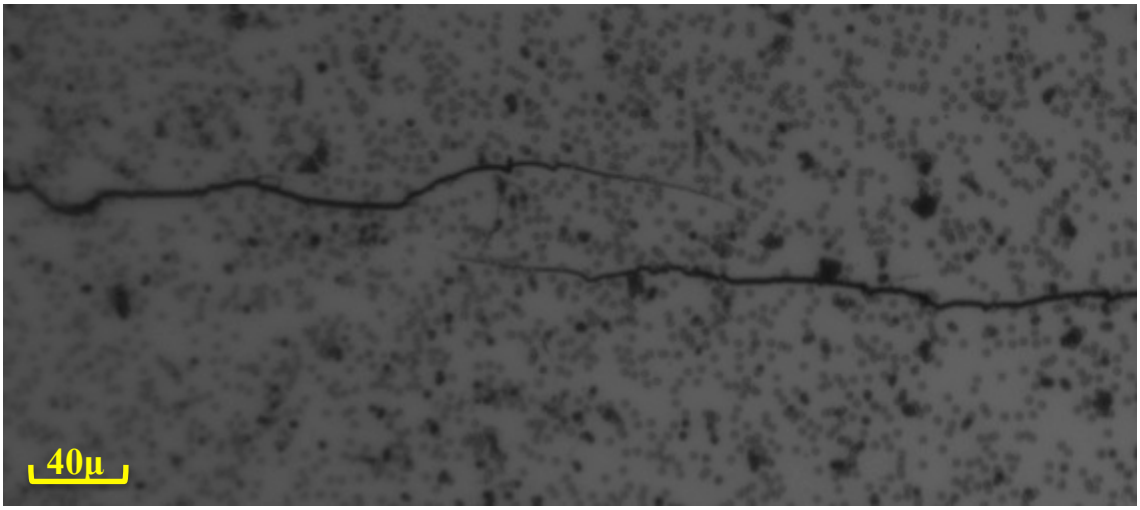

Figure 51. Twin cracks. This feature was observed on all samples, particularly at smaller crack lengths.

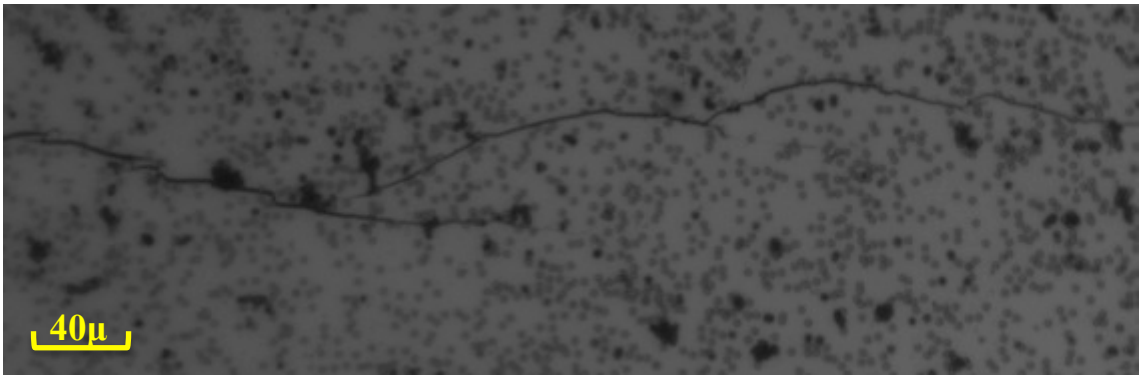

Figure 52. Region in which various crack paths are evident.

6.3 Strain Mapping

DIC Images were taken at roughly equal intervals along the length of the crack as it propagated. For each location a series of nine images were taken at nine load levels (four during loading, one at peak load and four during unloading). Figure 53 details the image layout. VIC-2D software was then used to analyze the images and produced strain fields.

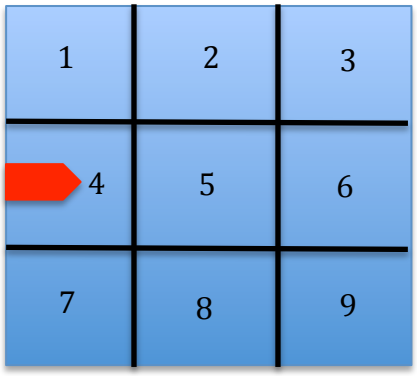

Figure 53. Diagram detailing the arrangement of the nine images captured at each load level. The red area represents the crack tip.

The first series of images produced some spurious results as shown in Figure 54. It was initially thought that the bands of high strain being shown were possible grain boundaries. This was quickly discounted however as the grains would have been around 0.5mm in diameter. Further analysis showed that the issue was with the software that had been utilized to stitch the images. The strain bands were determined to occur roughly where the images would have been stitched together. As a result only image 4. was used in the creation of the strain maps.

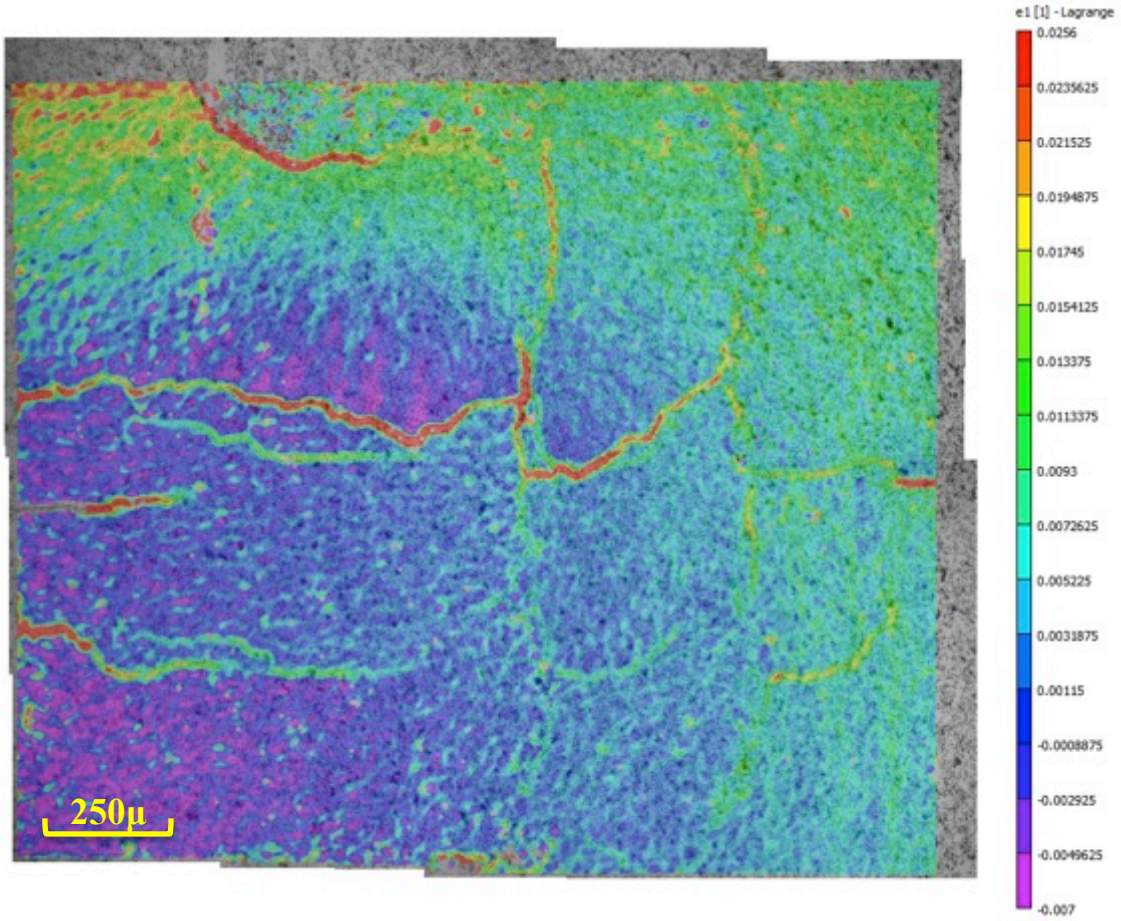

Figure 54. Example image detailing high strain bands observed, these bands are believed to be an artifact of the image stitching process.

When utilizing just image four of the nine image square, the DIC images obtained were much more indicative of the strain in the component at the time of loading. Figure 55, 56 and 57 show the strain map progression for a crack of 0.659 inches at three different load levels. It is clear to see that the rough contours between the three plots are roughly equal in shape and location. In the bottom left hand corner of each image appears to be evidence of the 45 degree plastic wake that is evident in other research of this type [29]. Although not readily evident due to the color plots, the third plot at the highest load does experience an overall greater strain throughout the material.

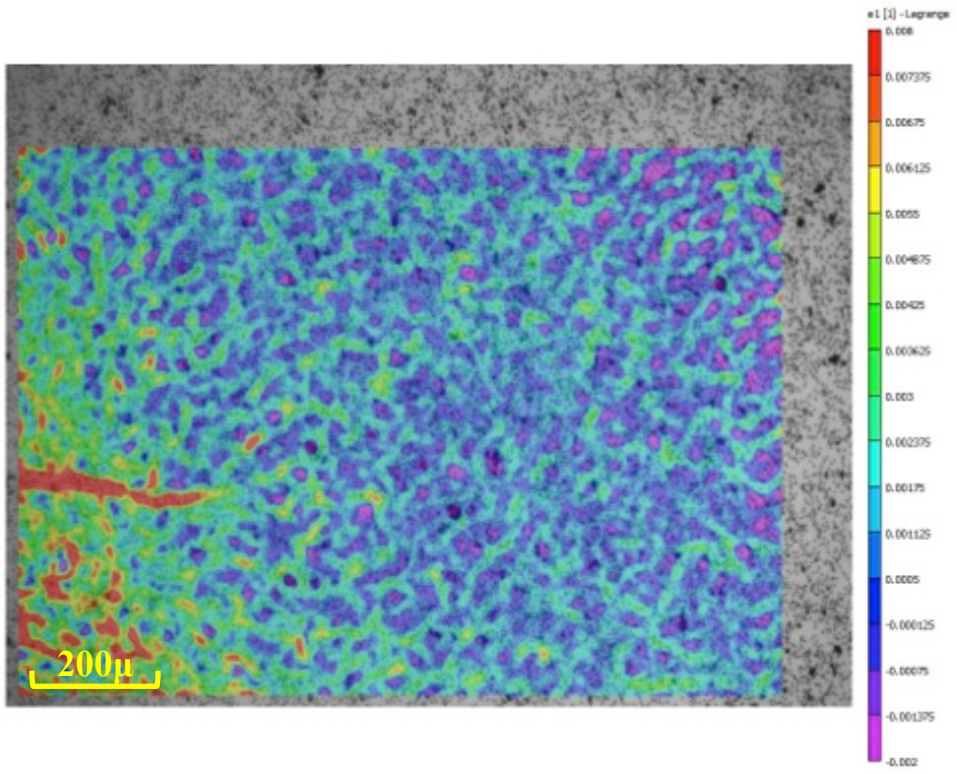

Figure 55. Strain map at 0.659 inches and 70.7lbs.

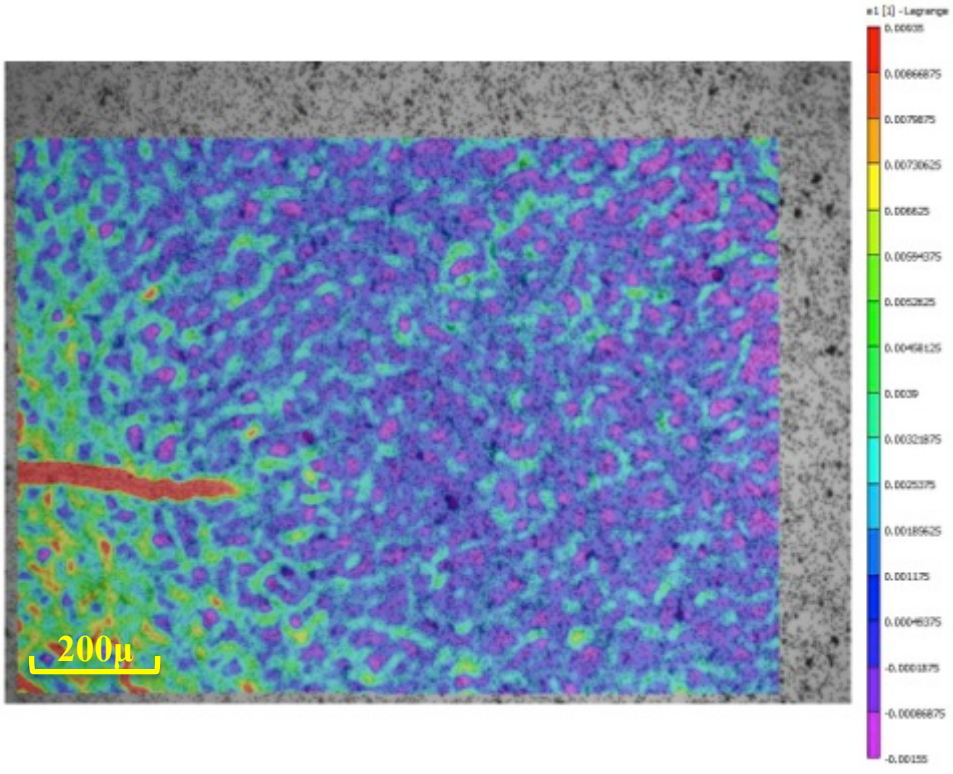

Figure 56. Strain map at 0.659 inches and 94.2lbs.

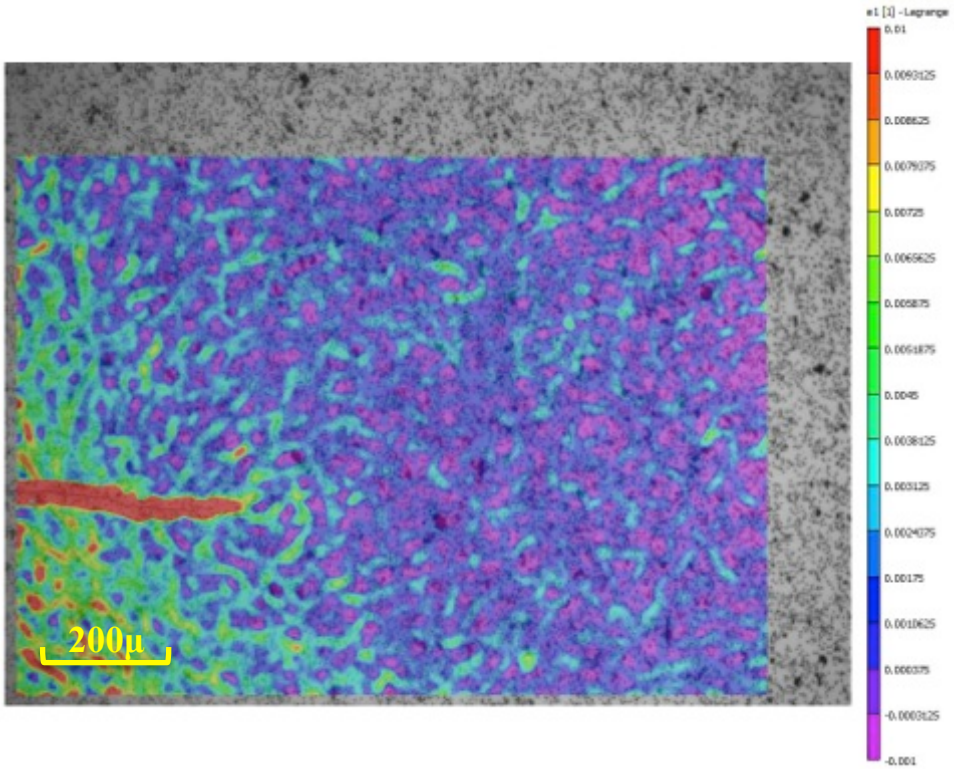

Figure 57. Strain map at 0.659 inches and 117.8lbs.

Figures 58, 59 and 60 show the strain map progression for a crack at 1.115 inches at three different load levels. With this series of images it is much easier to discern the progression of the strain fields. In Figure 58 the strain form appears relatively uniform with possible fringes of plastic wake visible in the upper and lower left hand corners. As load is increased we see the uniform area remain, however the plastic wake fringes intensify. At the next load level we see an the plastic wake fringes once again and a defined circular strain zone at the tip of the crack.

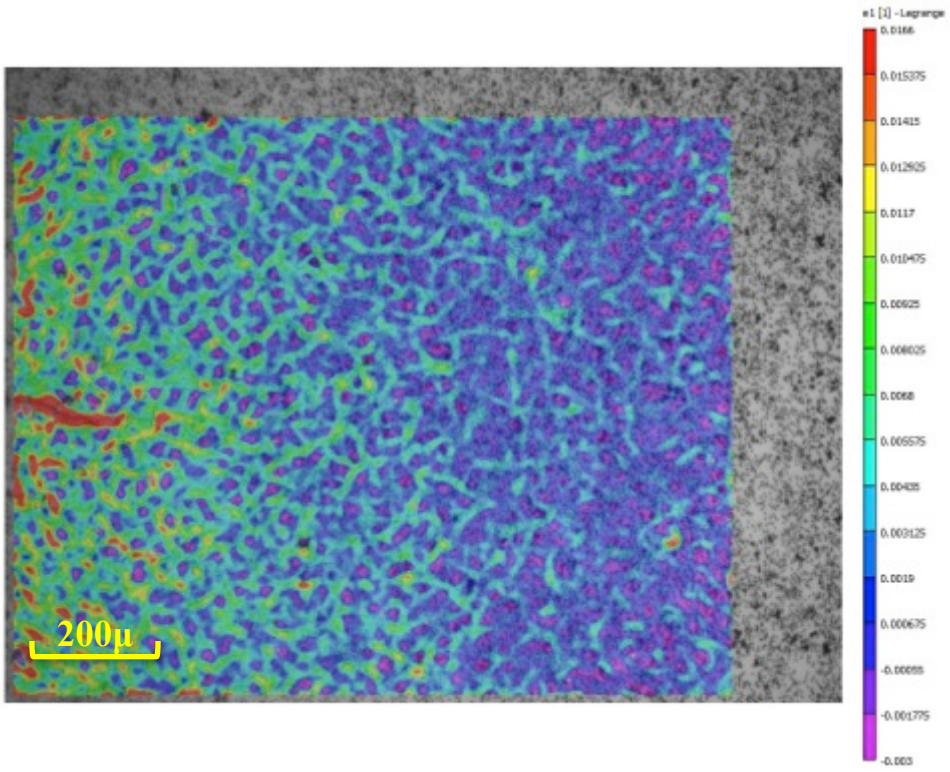

Figure 58 Strain map at 1.115 inches and 47.1lbs.

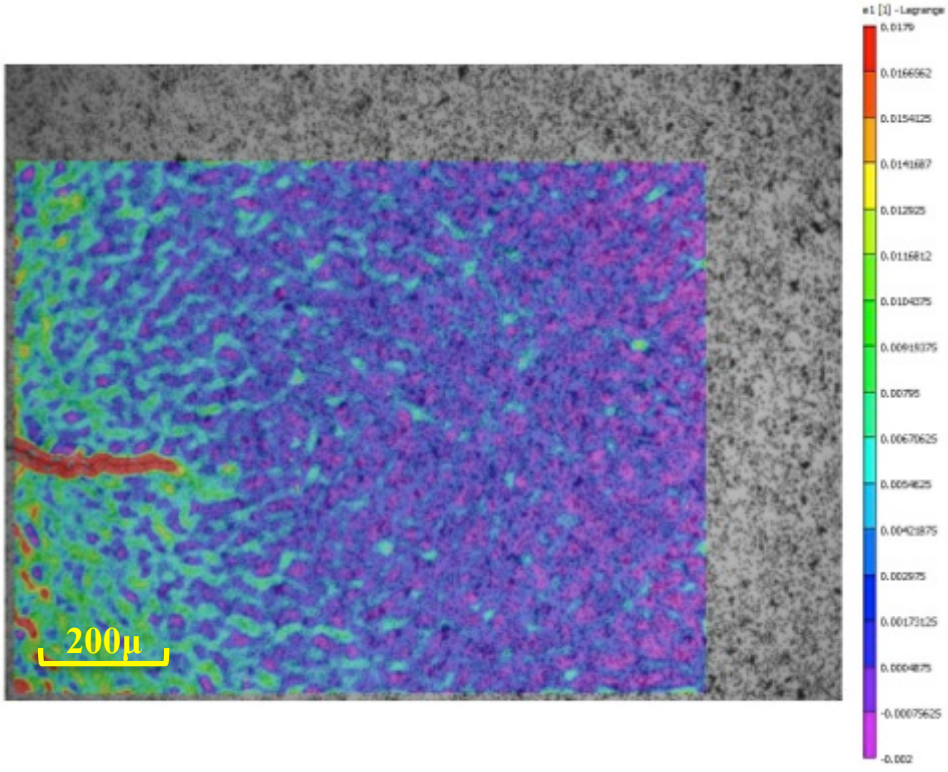

Figure 59. Strain map at 1.115 inches and 70.7lbs.

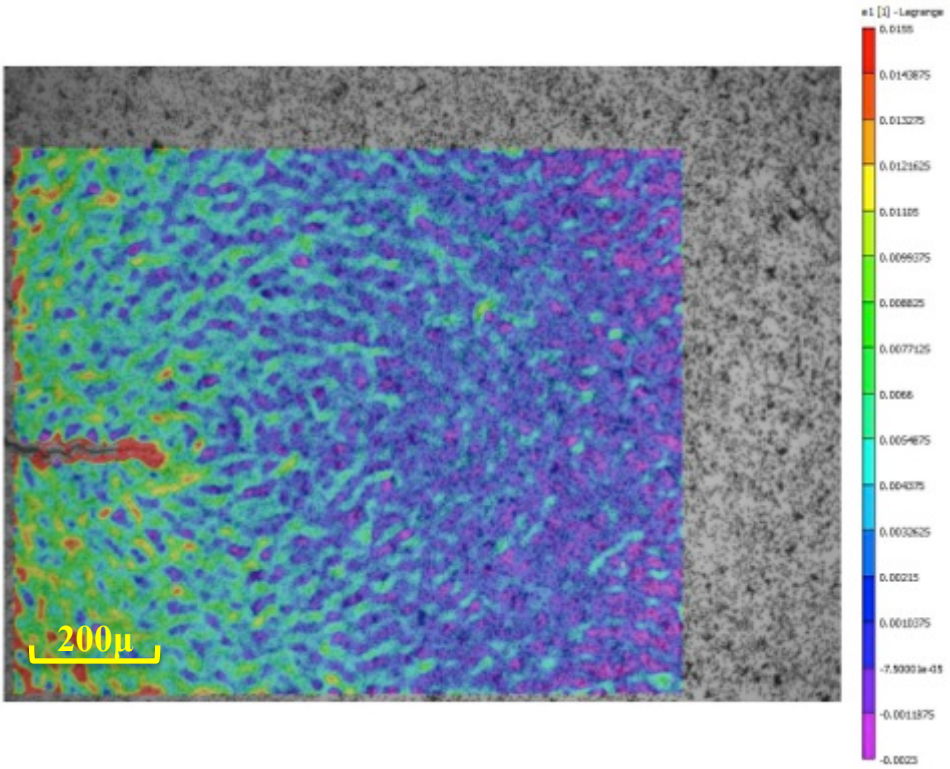

Figure 60. Strain map at 1.115 inches and 90.2lbs.

CHAPTER 7. SUMMARY

This research has provided the foundation for continued experiments on the characterization of small fatigue crack growth. A custom, and modifiable, load frame was developed in order to conduct the required testing. A custom fatigue crack growth code was also developed. This code incorporates calculations for crack length determined using strain data obtain from a BFS gage. The code also accounts for and calculates the magnitude of global closure effects on the specimen. The result is that a highly automated system for the development of fatigue crack data has been developed. This highly customizable system has demonstrated that with a minimum of effort, fatigue crack growth thresholds as low as 1×10^{-9} in/cycle can be reliably determined for both high and low load ratios using compression pre-cracking, with either a constant amplitude or load reduction loading scheme.

The magnitude of closure effects was reliably determined for all phases of testing and the development of a ΔK_{eff} for each test was possible. The collapse of all data onto a single da/dN vs. ΔK_{eff} curve enabled the determinate of a $\Delta K_{th} = 0.92\ (ksi\sqrt{in})$ value for Aluminum 7085.

The DIC imaging phase of this project has shown that the camera and lens combinations are suitable for obtaining wide field strain data and magnified image capture. The mapped strain fields have shown promising results in their raw form and further post processing may result in a much higher fidelity result. The DIC imagery has also proved itself a powerful tool to explain and correlate crack growth rate and closure effect results.

CHAPTER 8. RECOMMENDATIONS AND FUTURE WORK

8.1 Overview

Although a range of useful data has been generated by this work, a test matrix of follow up experiments have been suggested, and also confirm the data that has been produced to date. To ensure the successful conduct and outcome of this follow on work a number of recommendations have also been developed.

8.2 Recommendations

The following recommendations have been developed to ensure smooth operation of the machinery and that suitable imagery is obtained.

1. At the conclusion of each fatigue crack test the hydraulic pump cooling water filters should be cleaned/changed.
2. Hydraulic oil temperature should be monitored at least daily for any indication of a rise in temperature, which may be indicative of clogged filters or heat exchangers.
3. In the event of a hydraulic pump failure, allow pressure to bleed before removing a clevis pin prior to re-application of hydraulic power (re-application of hydraulic power should be accomplished under manual displacement control).
4. During DIC imagery capture, re-alignment on the crack tip should be performed at every load increment due to increased strain at higher load levels.

5. DIC Imagery should be captured every 0.1 inches of crack growth to allow better correlation of data. A full crack length series of images should also be obtained at this point.

6. During DIC capture any interesting crack features should be captured immediately and monitored, with crack length and load recorded.

8.3 Future Work

The following work is to be completed in the future by members of the School of Aeronautics and Astronautics Fatigue Lab as a series of ongoing Undergraduate Senior Research Projects, Masters and PhD Theses.

1. Software code modifications to allow for an integrated pre-cracking function.

2. Software code modifications to allow for an integrated closure load determination utilising a polynomial fitting method.

3. Conduct of the following fatigue crack growth and threshold determination tests.

Table 5. Future Fatigue Crack Growth Tests

Specimen 5	R=0.4 CPCA
Specimen 6	R=0.4 CPLR-CPCA
Specimen 7	R=0.7 CPCA
Specimen 8	R=0.7 CPLR=CPCA
Specimen 9	R=0.1 Spike Overload CPCA
Specimen 10	R=0.4 Spike Overload CPCA

4. Further development of the DIC capability incorporating EBSD results for increased image fidelity/resolution. EBSD should be performed and after testing

and consolidated with the DIC imagery. It is expected that development of this technique should produce results similar to those in Figure 61 in which similar experiments were conducted, albeit on a smaller scale.

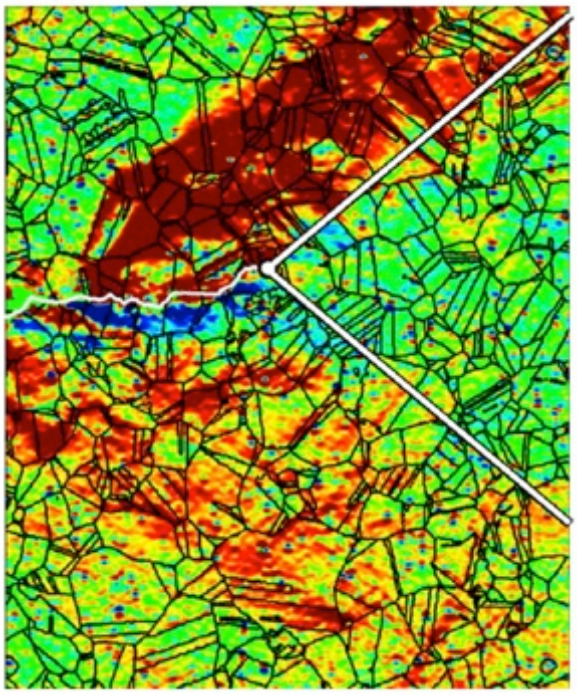

Figure 61. Correlated image of EBSD and DIC Strain Fields [61].

5. Confirmation of BFS closure levels using virtual extensometers in Vic2D software.
6. Development of the correlation methods between crack growth rate variability with tortuosity of crack and microstructure.

REFERENCES

REFERENCES

[1] Walter Schutz, "A History of Fatigue," *Engineering Fracture Mechanics*, vol. 54, no. 2, pp. 263-300, 1996.

[2] Norman E. Dowling, *Mechanical Behavior of Materials - Engineering Methods for Deformation, Fracture, and Fatigue*, 3rd ed., Holly Stark, Ed. Upper Saddle River, New Jersey, USA: Pearson Prentice Hall, 2007.

[3] Jaap Schijve, "Fatigue of Structures and Materials in the 20th Century and the State of the Art," *International Journal of Fatigue*, vol. 25, pp. 679-702, 2003.

[4] Fraterni A., Stephens R. R., Fuchs H., Stephens R. I., *Metal Fatigue in Engineering*.: Wiley, 2001.

[5] Alten Grandt, *Fundamentals of Structural Integrity*. Hoboken, New Jersey, USA: Wiley and Sons, 2004.

[6] US Air Force. AFGROW. [Online]. http://www.afgrow.net/applications/DTDHandbook/pdfs.aspx

[7] Sangid M., "The Physics of Fatigue Crack Initiation," *International Journal of Fatigue*, vol. 57, pp. 58-72, December 2013.

[8] Humfrey J., Ewing J., "The Frature of Metals Under Repeated Alternations of Stress," *Philos Trans Roy Soc Lond*, 1903.

[9] Hudak Jr S., Lankford J., "The Relevance of the small crack problem to lifetime prediction in gas turbines," *International Journal of Fatigue*, vol. 9, no. 2, pp. 87-93, 1987.

[10] Rovinelli A., "Influene of Microstucture Variability on Short Crack Growth Behavor," Universita di Bologna, Thesis 2013.

[11] Armstrong R., Antolovich S., "Plastic Strain Localization in Metals: Origins and Consequences," *Progress in Materials Science*, vol. 59, pp. 1-160, 2014.

[12] ASTM International, *Standard Test Method for Measurement of Fatigue Crack Growth Rates*.: ASTM International, 2011.

[13] S. Pearson, "Initiation of Fatigue Cracks in Comercial Aluminium Alloys and the Subsequent Propagation of Very Short Cracks," *Engineering Fracture Mechanics*, vol. 7, pp. 235-247, 1975.

[14] Schneider J., Daniel A., McKnight D., Newman Jr J., "Compression Pre-Cracking to Generate Near Threshold Fatigue-Crack-Growth Rates in Two Aluminium Alloys," *International Journal of Fatigue*, vol. 27, 2005.

[15] George Irwin, "Analysis of Stresses and Strains Near the End of a Crack Traversing a Plate," *Journal of Applied Mechanics*, vol. 24, pp. 361-364, 1957.

[16] Alan Griffith, "The Phenomena of Rupture and Flow in Solids," *Philos. Trans. R. Soc.*, vol. 221, 1920.

[17] Jaap Schijve, *Fatigue of Structures and Materials*. Dordrecht, The Netherlands: Kluwer Academic Publishers, 2001.

[18] Bahram Farahmand et al., *Fatigue and Fracture Mechanics of High Risk Parts*. New York, New York, USA: Chapman and Hall, 2007.

[19] TheDiagram. The Diagram. [Online]. thediagram.com/12-3/ththreemodes.html

[20] Erdogan F. Paris P., "A Critical Analysis of Crack Propagaiton Laws," *Transactions of the ASME, Journal of Basic Engineering*, vol. 85, no. 3, pp. 528-534, 1963.

[21] Boettner R., McEvily A., "On Fatigue Crack Propagation in F.C.C Metals," *International Conference on Mechanisms of Fatigue in Crystalline Solids*, vol. 11, pp. 725-743, November 1962.

[22] Ritchie R., "Propagation of short fatigue cracks," *International Materials Reviews*, vol. 29, no. 1, pp. 445-475, 1984.

[23] Walker K., "The Effect of Stress Ratio During Crack Propagation and Fatigue for 2024-T3 and 7075-T6, The Effect of Environment and Complex Load History on Fatigue Life," *Effects of Environment and Complex Load History on Fatigue Life*, pp. 1-14, 1970.

[24] Forman R., et al., "Numerical Analysis of Crack Propagation in Cyclic Load Structures," *Journal of Basic Engineering*, vol. 89, no. 3, pp. 459-463, 1967.

[25] Borrego L., et al., "Comparison of The Crack Growth Behanviour of AA6082-T6 and AA6061-T651 Aluminium Alloys," *Anales de Mecanica de la Fractura 28*, vol. 1, 2011.

[26] Wolf Elber, "The Significance of Fatigue Crack Closure," *Damage Tolerance in Aircraft Structures, ASTM STP 486*, pp. 230-242, 1971.

[27] Wolf Elber, "Crack Closure and Crack Growth Measurements in Surface Flawed Titanium Alloy Ti-6al-4V," National Aeronautics and Space Administration, Hampton, Technical Note 1975.

[28] Carrol J., et al., "Investigation of Fatigue Crack Closure Using Multiscale Image Correlation Experiments," *Engineering Fracture Mechanics*, vol. 76, 2009.

[29] AllisonJ., et al., "A Comparison of Measurement Methods and Numerical Procedures for the Experiemntal Characterization of Fatigue Crack Closure," *Mechanics of Fatigue Crack Closure ATM STP 982*, pp. 171-185, 1988.

[30] Jaap Schijve, "Fatigue Crack Closure: Observations and Technical Significance," pp. 5-34, 1988.

[31] McEvily J., "On Crack Closure and Fatigue Crack Growth," *Mechanics of Fatigue Crack Closure*, pp. 35-43, 1988.

[32] Liaw P., "Overview of Crack Closure at Near Threshold Fatigue Crack Growth Levels," *Mechanics of Fatigue Crack Closure*, pp. 62-92, 1988.

[33] Pippan R., Riemelmoser F., "Consideration of the mechanical behaviour of small fatigue cracks," *International Journal of Fracture*, vol. 118, pp. 251-270, 2002.

[34] Newman Jr J., et al., "Small-Crack Growth and Fatigue Life Predictions for High Strength Aluminium Alloys. Part II," *Fatigue Fract Engng Mater Struct*, pp. 59-72, 1999.

[35] Miller K., "The Behaviour of Short Fatigue Crcaks and Their Initiation Part 1," *Fatigue Fract. Engng Mater. Struct.*, vol. 10, no. 1, pp. 75-91, 1987.

[36] Yoder G., et al., "Quantitative Analysis of Microstructural Effects on Fatigue Crack Growth in Widmanstatten," *Journal of the Mechanics and Physics of Solids*, vol. 61, no. 8, pp. 1670-1690, 1979.

[37] de los Rios E., Navarro A., "An Alternative Model of the Blocking of Dislocations at Grain Boundaries," *Philosophical Magazine A (Physics of Condensed Matter, Defects and Mechanical Properties)*, pp. 37-42, 1988.

[38] Lankford J., "The Growth of Small Fatigue Cracks in 7075-T6 Aluminium," *Fatigue Fract Engng Mater Struct*, vol. 5, no. 3, pp. 233-248, 1982.

[39] Martin J., Nicholls D., "A Comparison of Small Fatigue Crack Growth, Low Cycle Fatigue and Long Fatigue Crack Growth in Al-Li Alloys," *Fatigue Fract. Engng Mater. Struct*, vol. 14, no. 2/3, p. 185/192, 1991.

[40] Pippan R., et al., "A Comparison of Different Methods to Determine Threshold of Fatigue Crack Propagation," *International Journal of Fatigue*, vol. 16, no. 8, pp. 579-582, 1994.

[41] Newman Jr J., Forman R., Forth S., "On Generating Fatigue Crack Growth Thresholds," *International Journal of Fatigue*, vol. 25, pp. 9-15, 2003.

[42] McEvily A., Minakawa K., "On Near-Threshold Fatigue Crack Growth in Steels and Aluminium Alloys," *Int. Symposium on Fatigue Thresholds*, vol. 2, 1981.

[43] Newman J., "Analysis of Fatigue Crack Growth and Closure Near Threshold Conditions," STI Program Office, National Aeronautics and Space Administration, 1999.

[44] Newman Jr J., "A Nonlinear Fracture Mechanics Approach to the Growth of Small Cracks," National Aeronautics and Space Administration, Hampton, 1983.

[45] Newman Jr J., Yamada Y., "Crack-Closure Behavior of 2324-T39 Aluminium Alloy Near-Threshold Conditoins for High Load Ration and Constant Kmax Tests," *International Journal of Fatigue*, vol. 31, 2008.

[46] Newman Jr J., Yamada Y., "Compression Precracking Methods to Generate Near-Threshold Fatigue Crack Growth Rate Data," *International Journal of Fatigue*, vol. 32, 2010.

[47] Hubbard R., "Crack Growth Under Cyclic Compression," *Journal of Basic Engineering*, December 1969.

[48] Forth C., Newman J., James M., "Load History Effects Resulting from Compression Pre-Cracking," *Journal of ASTM International*, vol. 2, no. 9, 2005.

[49] Newman Jr J., "Compression Pre-Cracking Test Procedures and Crack Growth Monitoring in Compact (or ESE(T)) Specimens," 2012.

[50] MTS Systems Corporation, *MTS TestSuite Multipurpose Elite User Guide*.: MTS Systems Corporation, 2013.

[51] MTS Systems Corporation, *Series 609 Alignment Fixture Product Information*.: MTS Systems Corporation, 2008.

[52] ASTM International, *Standard Practice for Verification of Testing Frame and Specimen Alignment Under Tensile and Compressive Axial Force Application*.: ASTM International, 2012.

[53] Vishay Measurements Group., *Student Manual for Strain Gage Technology*., 1992.

[54] Mueller L., et al, "ALCOA 7085 Die Forgings - 7th Generation Structural Solutions," ALCOA Technical Center, ALCOA, Green Letter 2006.

[55] Yamada Y., "Experimental Investgations on Near-Threshold Events in Fatigue Crack Growth," Aerospace Engineering, Mississippi State University, Thesis 2010.

[56] Walker K. (2013) ESE(T) Specimen Layout and Geometry.

[57] Newman J. (2103, June) Email - Back Face Strain Gages and Compression Pre-Cracking.

[58] Puccio Brandon., "AAE 490 Speckle Pattern Procedure," School of Aeronautics and Astronautics, Purdue University, 2013.

[59] Donald K., *Fracture Tech Manual*.: Fracture Tech, 2013.

[60] Pippan R., "The Growth of Short Cracks Under Cyclic Compression," *Fatigue Fract. Engng Mater. Struct*, vol. 9, no. 5, pp. 319-328, 1987.

[61] Sangid M.D., et al., "High Resolution Analysis Of Opening and Sliding in Fatigue Crack Growth," *International Journal of Fatigue*, vol. 37, pp. 134-145, April 2012.

[62] Carroll J., et al., "High Resolution Digital Image Correlation Measurments of Strain Accumulation of Fatigue Crack Growth," *International Journal of Fatigue*, 2012.

[63] Barter S., Chen F., Jones R., "Experimental Studies into Short Crack Growth," *Engineering Failure Analysis*, vol. 18, 2011.

APPENDICIES

Appendix A – Alignment Data

Alignment Data

MTS Method

SG1	222	SG7	220	Width	1.5
SG2	220	SG8	212	d	0.38
SG3	222	SG9	225		
SG4	211	SG10	214		

Upper Level

Bx	2.64	PBSx	1.206857
By	-6.58784	PBSy	-3.01158

Lower Level

Bx	-1.75	PBSx	-0.80367
By	-5.74597	PBSy	-2.63879

ASTM Method

a	218.75	e1	225.3378	MaxB	8.837838
w	1.5	e3	212.1622	PB	4.040154
d	0.38	e2	221		
		e4	216.5		

Raw Data

				Microstrain Readings				
SG	200	400	600	800	200	400	600	800
1	54	110	166	221	54	108	164	219
2	55	111	166	218	56	110	165	219
3	54	108	161	217	55	110	164	218
4	51	103	156	211	51	105	158	212
7	56	113	169	223	55	111	167	222
8	54	110	164	217	54	109	163	218
9	55	109	164	221	56	111	166	221
10	54	106	158	212	54	107	159	213
BS Top	3.7	4.1	3.8	3.3	3.7	2.1	2.6	2.3
BS Bottom	3.2	4.6	5.08	4.2	3.2	3.2	4.1	3.5
				Microstrain Readings				
	200	400	600	800	200	400	600	800
	53	106	161	216	56	112	168	223
	56	110	164	219	56	110	164	217
	56	112	166	220	57	111	166	220
	50	104	158	212	54	108	160	215
	56	112	167	221	57	114	170	224
	60	116	171	224	57	112	166	219
	55	110	166	222	55	109	163	221
	53	105	158	213	53	106	159	211
BS Top	4.2	1.8	1.7	1.5	3.1	2.9	4	3.1
BS Bottom	5.3	3.4	3.3	2.5	4.5	4.7	4.6	4.7

Appendix B – Code Flow Diagram

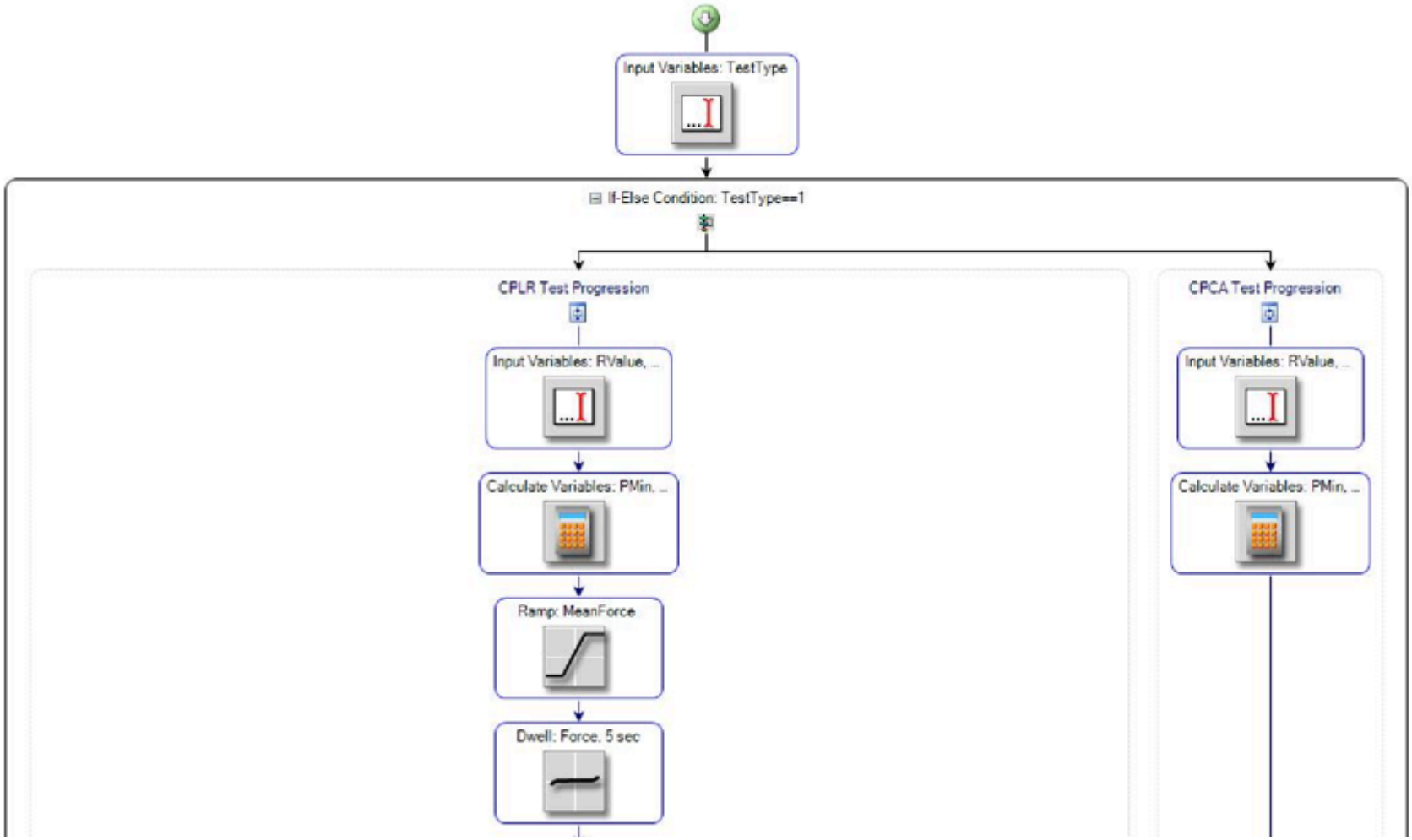
Input Variables: TestType
If-Else Condition: TestType==1
CPLR Test Progression
Input Variables: RValue, ...
Calculate Variables: PMin, ...
Ramp: MeanForce
Dwell: Force, 5 sec
CPCA Test Progression
Input Variables: RValue, ...
Calculate Variables: PMin, ...

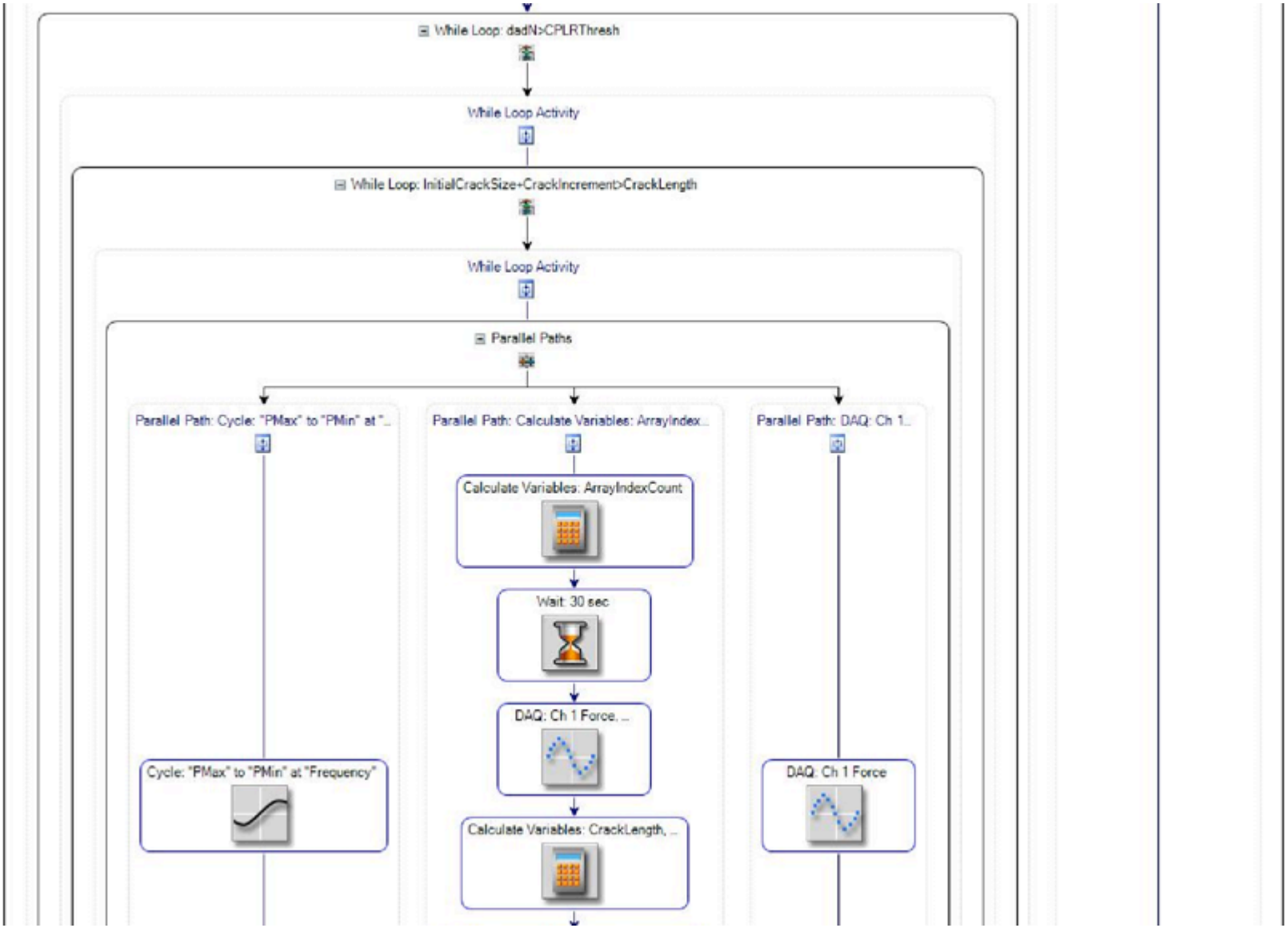
While Loop: dadN>CPLRThresh
While Loop Activity
While Loop: InitialCrackSize+CrackIncrement>CrackLength
While Loop Activity
Parallel Paths
Parallel Path: Cycle: "PMax" to "PMin" at "...
Parallel Path: Calculate Variables: ArrayIndex...
Parallel Path: DAQ: Ch 1...
Calculate Variables: ArrayIndexCount
Wait: 30 sec
DAQ: Ch 1 Force, ...
Calculate Variables: CrackLength, ...
Cycle: "PMax" to "PMin" at "Frequency"
DAQ: Ch 1 Force

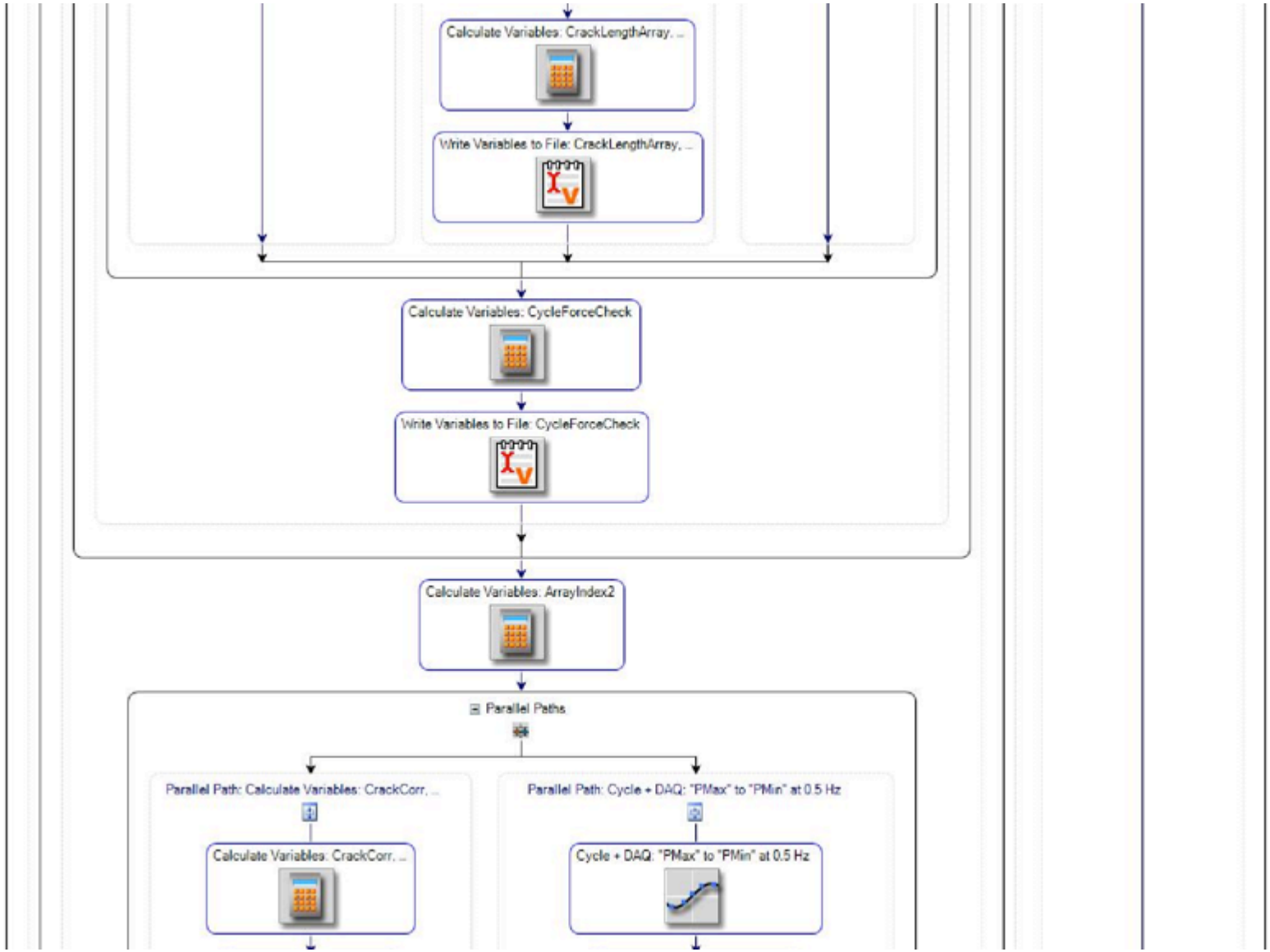
Calculate Variables: CrackLengthArray, ...
Write Variables to File: CrackLengthArray, ...
Calculate Variables: CycleForceCheck
Write Variables to File: CycleForceCheck
Calculate Variables: ArrayIndex2
Parallel Paths
Parallel Path: Calculate Variables: CrackCorr, ...
Calculate Variables: CrackCorr, ...
Parallel Path: Cycle + DAQ: "PMax" to "PMin" at 0.5 Hz
Cycle + DAQ: "PMax" to "PMin" at 0.5 Hz

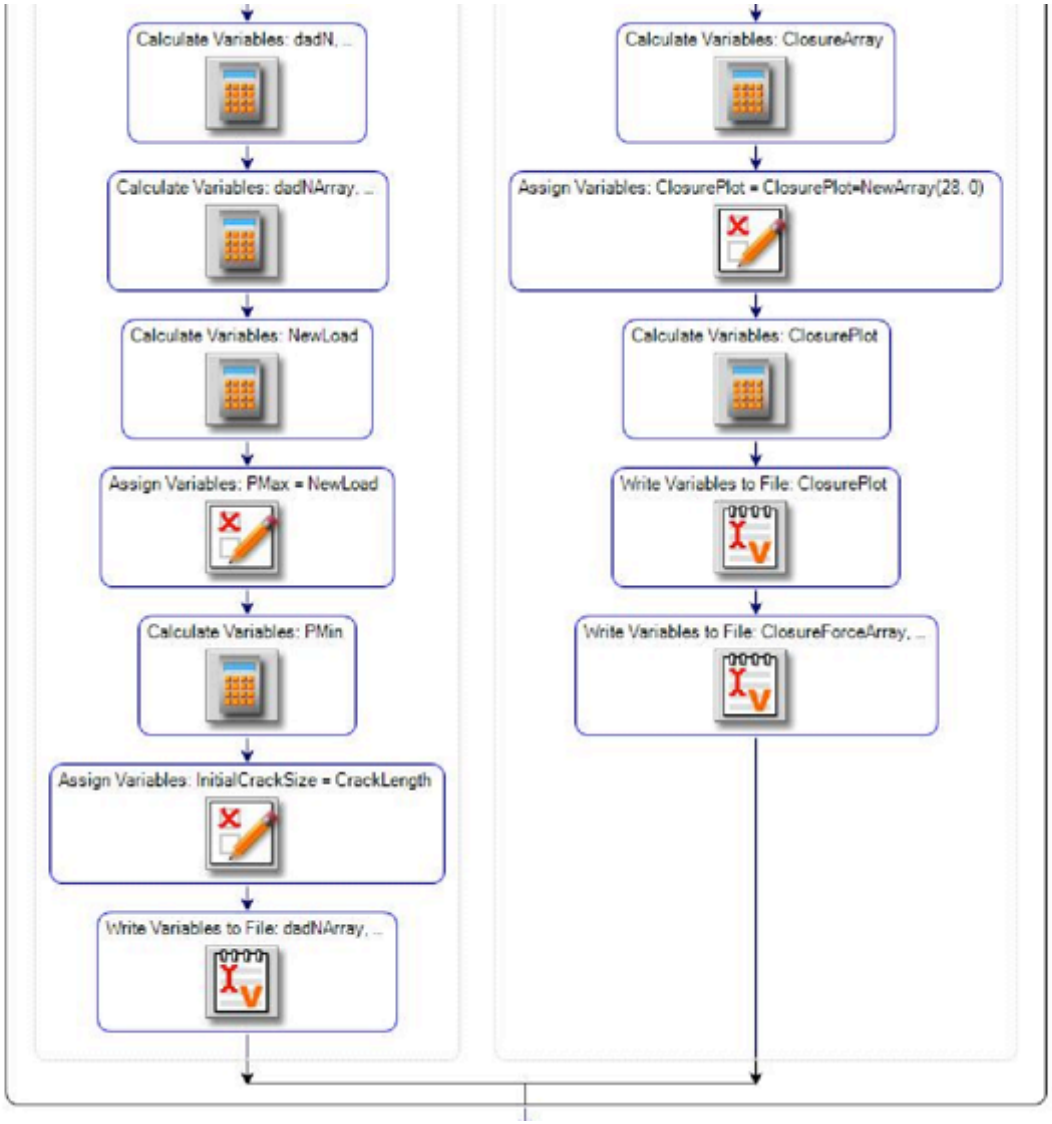
Calculate Variables: dadN, ...
Calculate Variables: dadNArray, ...
Calculate Variables: NewLoad
Assign Variables: PMax = NewLoad
Calculate Variables: PMin
Assign Variables: InitialCrackSize = CrackLength
Write Variables to File: dadNArray, ...
Calculate Variables: ClosureArray
Assign Variables: ClosurePlot = ClosurePlot=NewArray(28, 0)
Calculate Variables: ClosurePlot
Write Variables to File: ClosurePlot
Write Variables to File: ClosureForceArray, ...

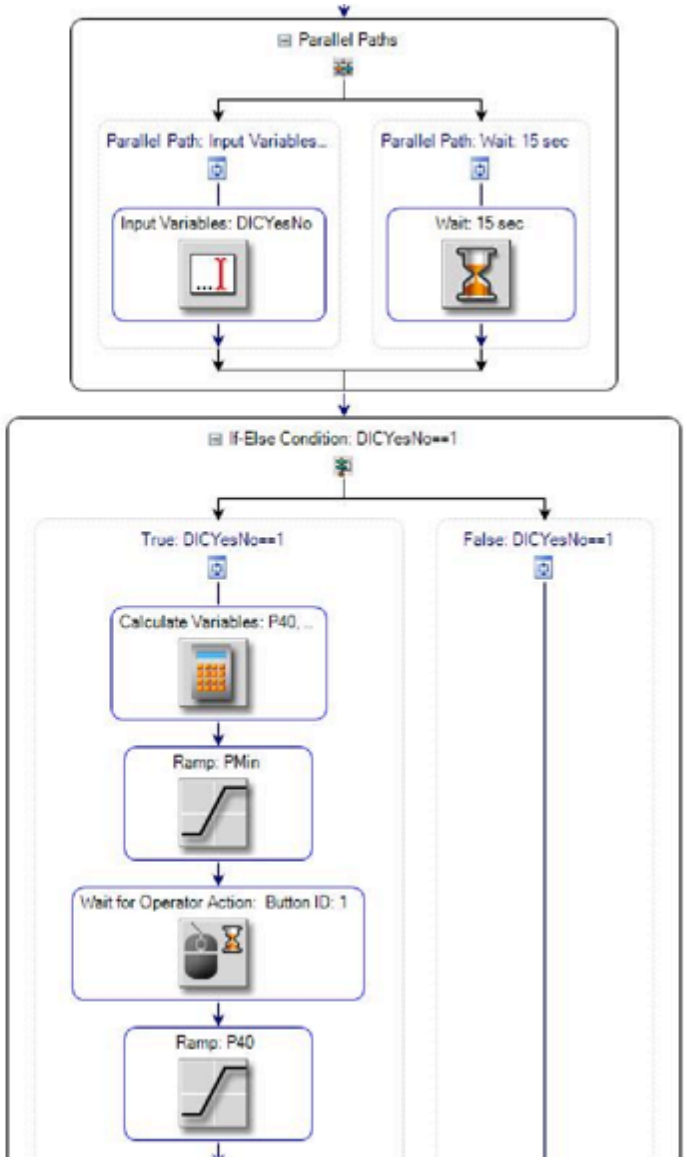
Parallel Paths
Parallel Path: Input Variables...
Parallel Path: Wait: 15 sec
Input Variables: DICYesNo
Wait: 15 sec
If-Else Condition: DICYesNo==1
True: DICYesNo==1
False: DICYesNo==1
Calculate Variables: P40, ...
Ramp: PMin
Wait for Operator Action: Button ID: 1
Ramp: P40

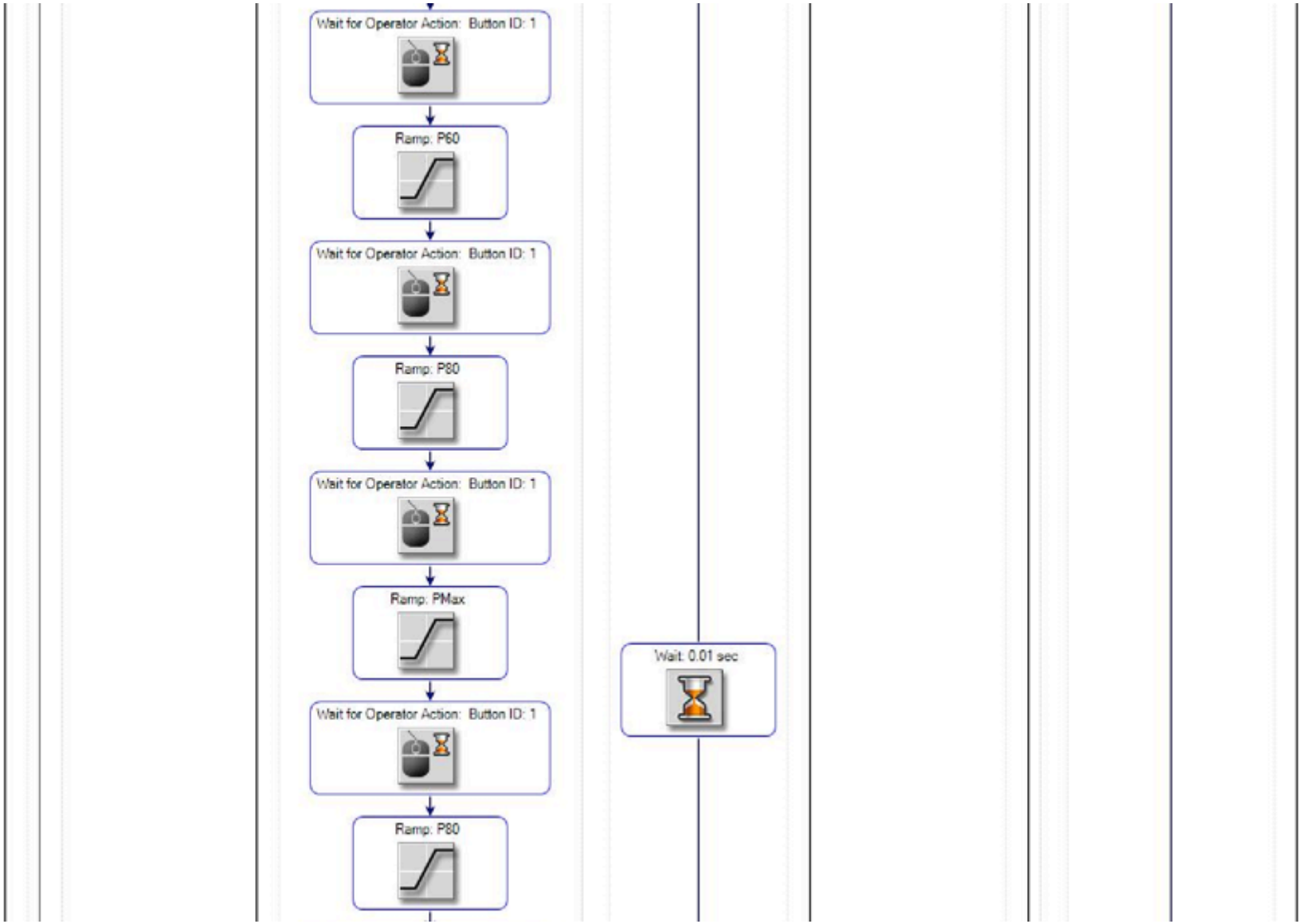
Wait for Operator Action: Button ID: 1
Ramp: P60
Wait for Operator Action: Button ID: 1
Ramp: P80
Wait for Operator Action: Button ID: 1
Ramp: PMax
Wait for Operator Action: Button ID: 1
Ramp: P80
Wait: 0.01 sec

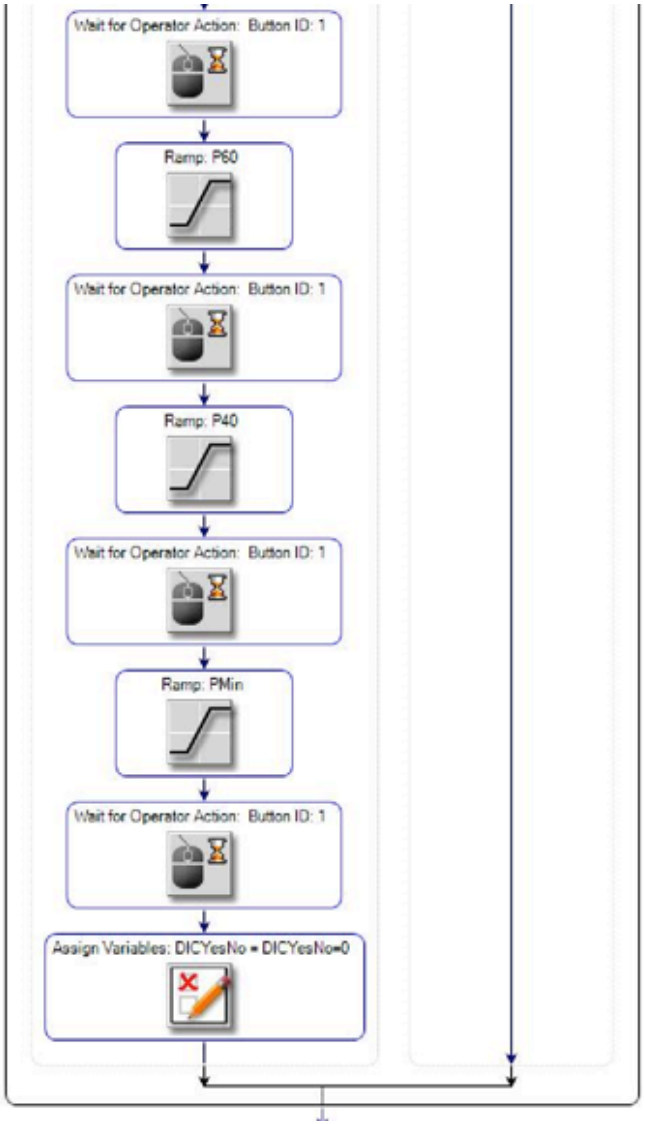
Wait for Operator Action: Button ID: 1
Ramp: P60
Wait for Operator Action: Button ID: 1
Ramp: P40
Wait for Operator Action: Button ID: 1
Ramp: PMin
Wait for Operator Action: Button ID: 1
Assign Variables: DICYesNo = DICYesNo=0

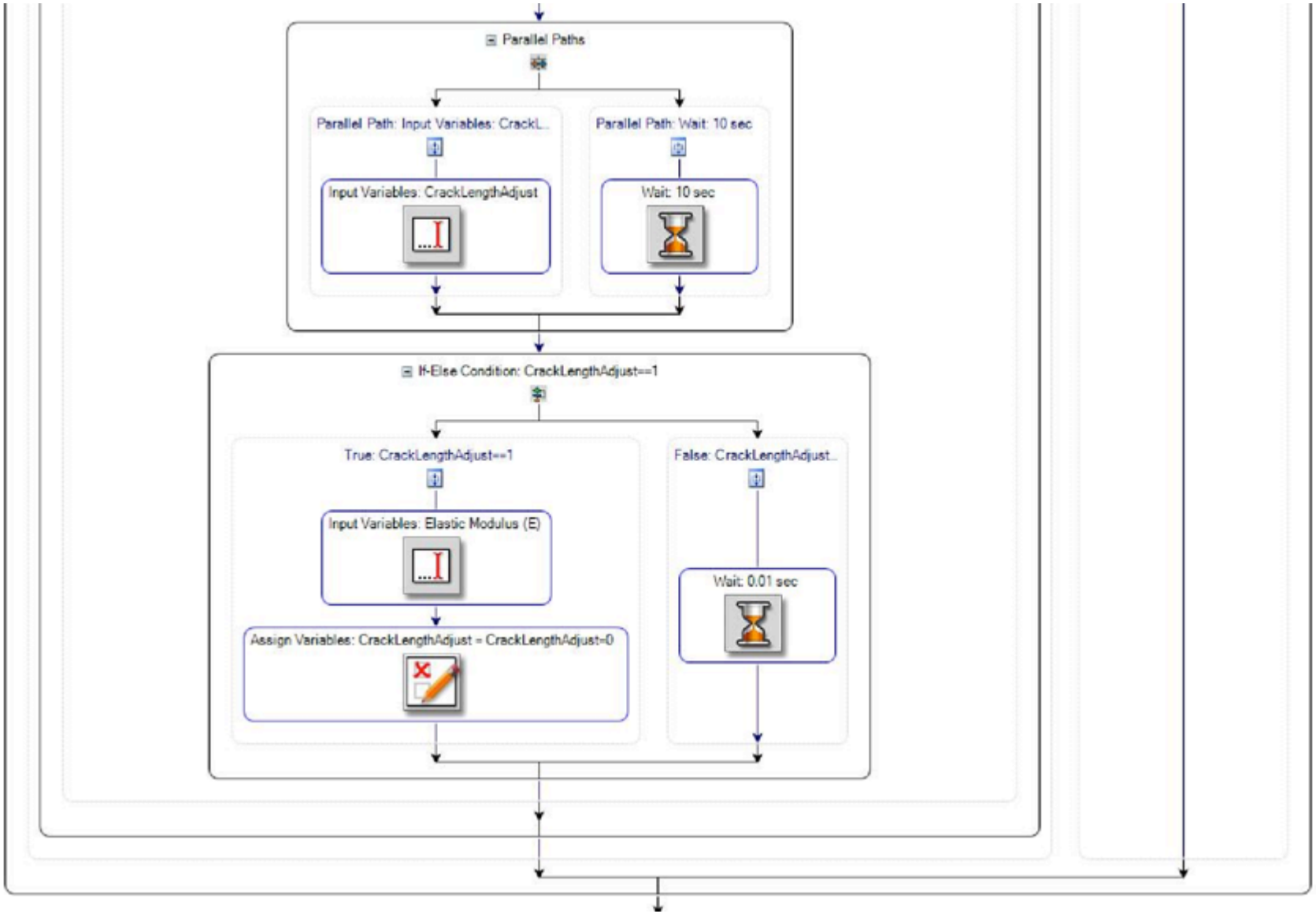
Parallel Paths
Parallel Path: Input Variables: CrackL...
Parallel Path: Wait: 10 sec
Input Variables: CrackLengthAdjust
Wait: 10 sec
If-Else Condition: CrackLengthAdjust==1
True: CrackLengthAdjust==1
False: CrackLengthAdjust...
Input Variables: Elastic Modulus (E)
Wait: 0.01 sec
Assign Variables: CrackLengthAdjust = CrackLengthAdjust=0

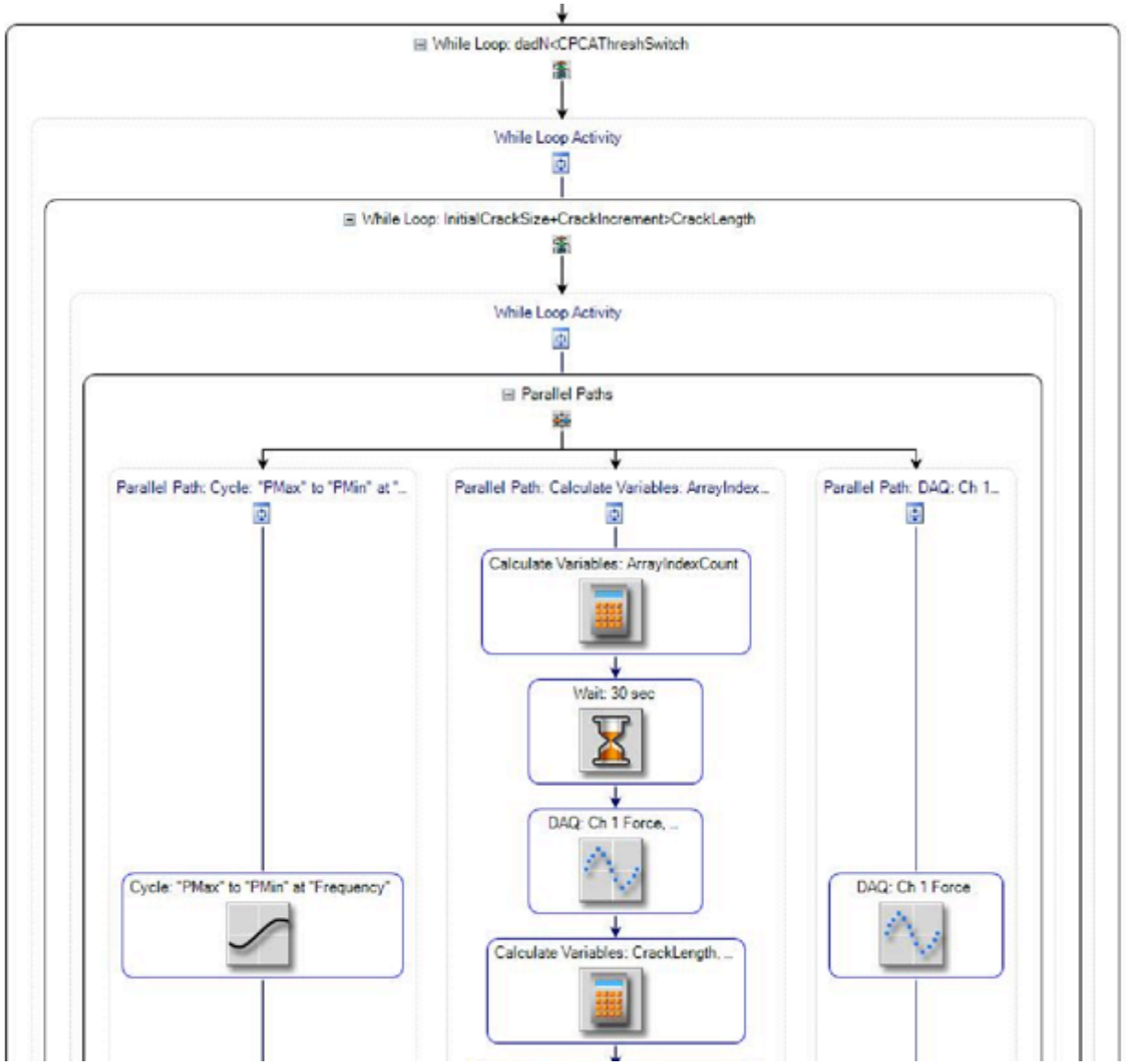
While Loop: dadN<CPCAThreshSwitch
While Loop Activity
While Loop: InitialCrackSize+CrackIncrement>CrackLength
While Loop Activity
Parallel Paths
Parallel Path: Cycle: "PMax" to "PMin" at "...
Parallel Path: Calculate Variables: ArrayIndex...
Parallel Path: DAQ: Ch 1...
Calculate Variables: ArrayIndexCount
Wait: 30 sec
DAQ: Ch 1 Force, ...
Cycle: "PMax" to "PMin" at "Frequency"
Calculate Variables: CrackLength, ...
DAQ: Ch 1 Force

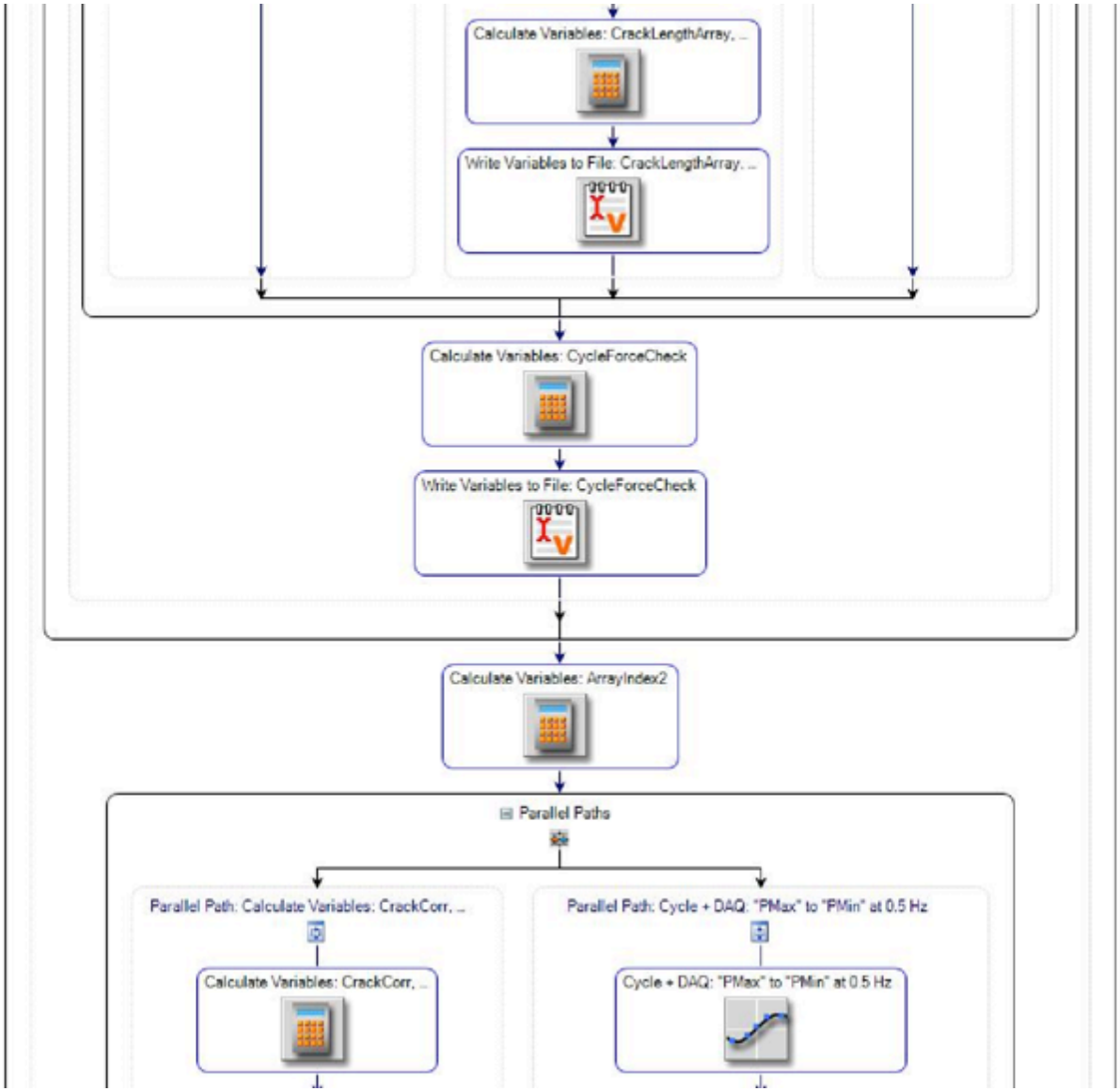
Calculate Variables: CrackLengthArray, ...
Write Variables to File: CrackLengthArray, ...
Calculate Variables: CycleForceCheck
Write Variables to File: CycleForceCheck
Calculate Variables: ArrayIndex2
Parallel Paths
Parallel Path: Calculate Variables: CrackCorr, ...
Calculate Variables: CrackCorr, ...
Parallel Path: Cycle + DAQ: "PMax" to "PMin" at 0.5 Hz
Cycle + DAQ: "PMax" to "PMin" at 0.5 Hz

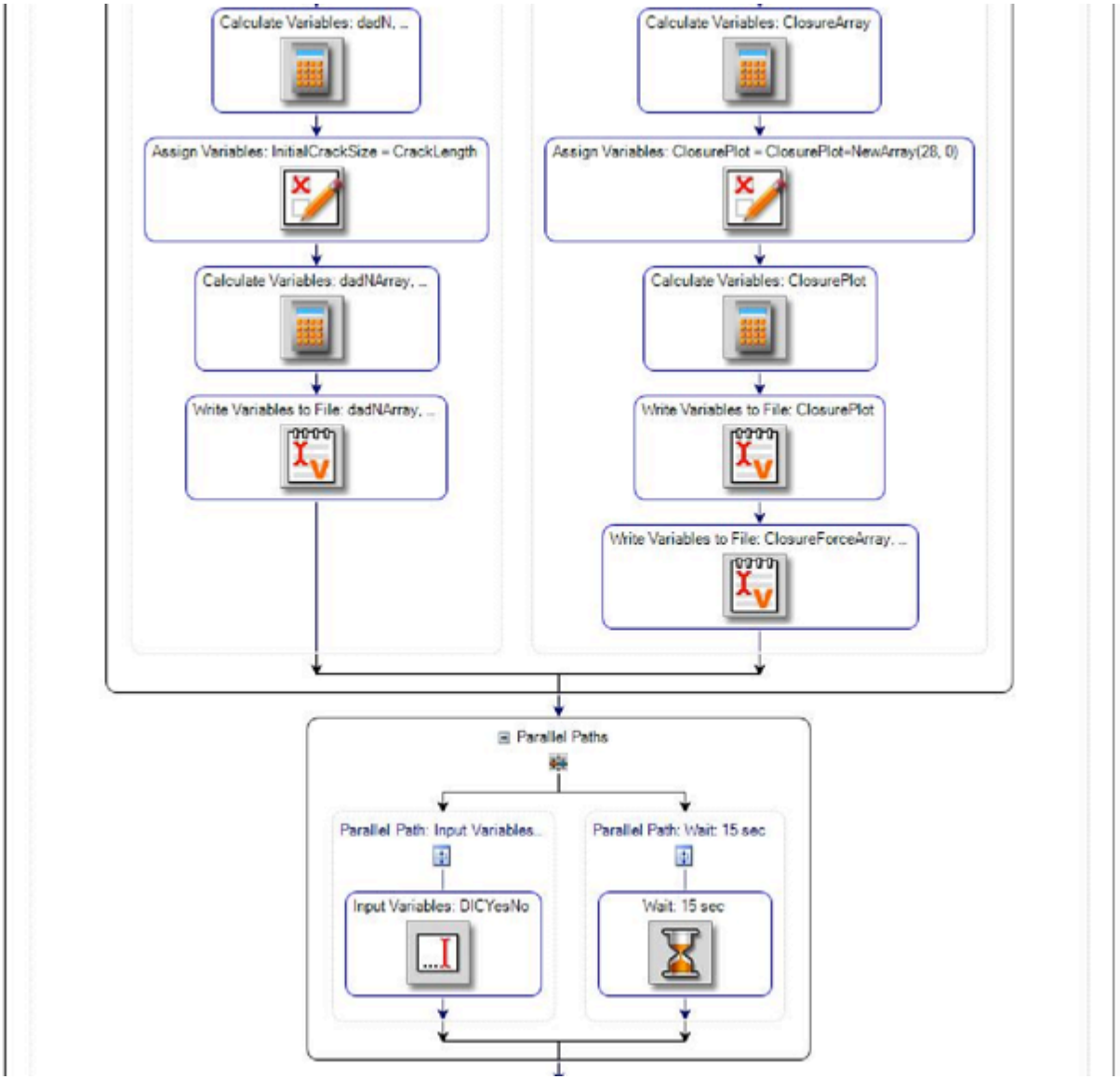
Calculate Variables: dadN, ...
Assign Variables: InitialCrackSize = CrackLength
Calculate Variables: dadNArray, ...
Write Variables to File: dadNArray, ...
Calculate Variables: ClosureArray
Assign Variables: ClosurePlot = ClosurePlot=NewArray(28, 0)
Calculate Variables: ClosurePlot
Write Variables to File: ClosurePlot
Write Variables to File: ClosureForceArray, ...
Parallel Paths
Parallel Path: Input Variables...
Input Variables: DICYesNo
Parallel Path: Wait: 15 sec
Wait: 15 sec

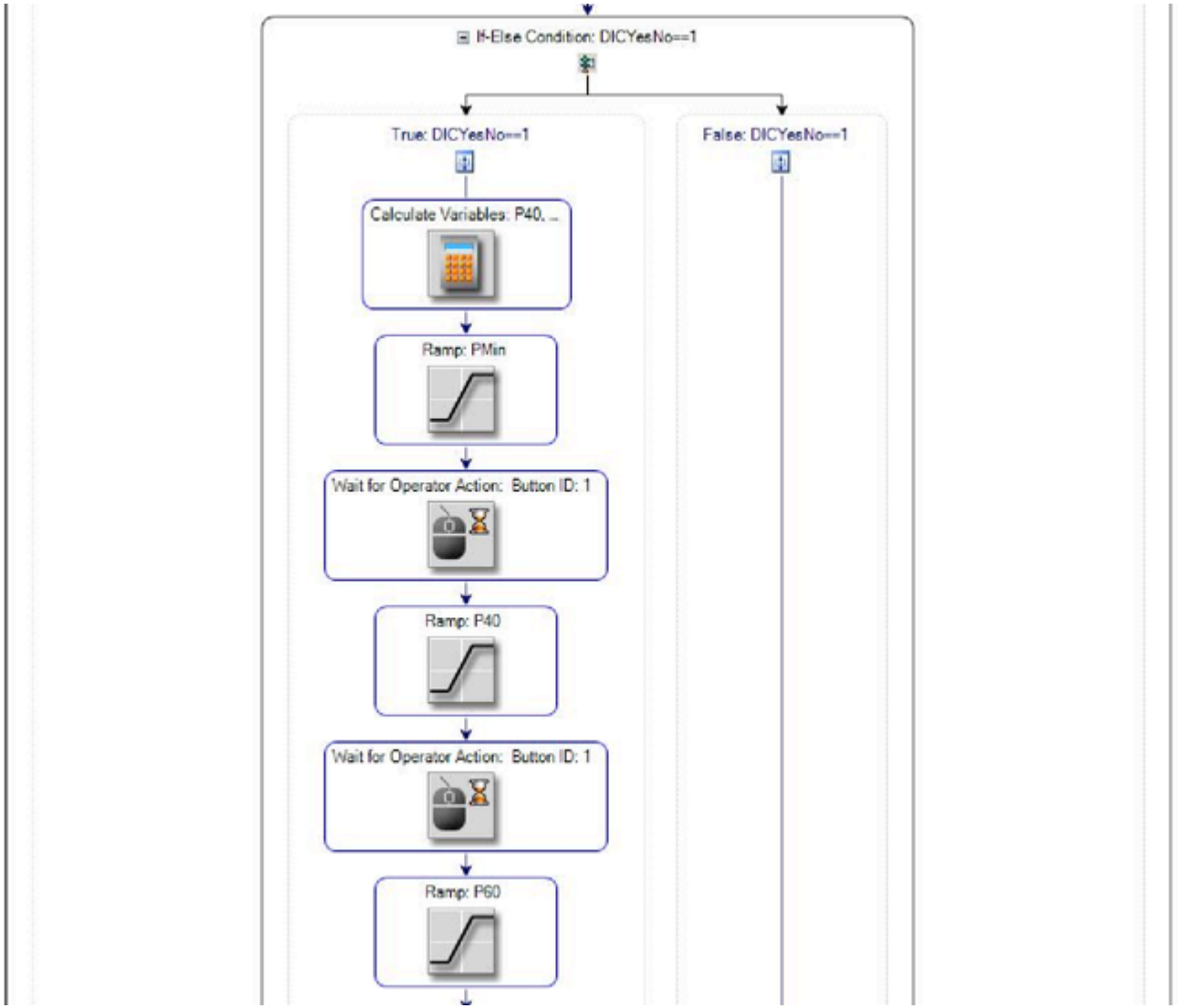
If-Else Condition: DICYesNo==1
True: DICYesNo==1
False: DICYesNo==1
Calculate Variables: P40, ...
Ramp: PMin
Wait for Operator Action: Button ID: 1
Ramp: P40
Wait for Operator Action: Button ID: 1
Ramp: P60

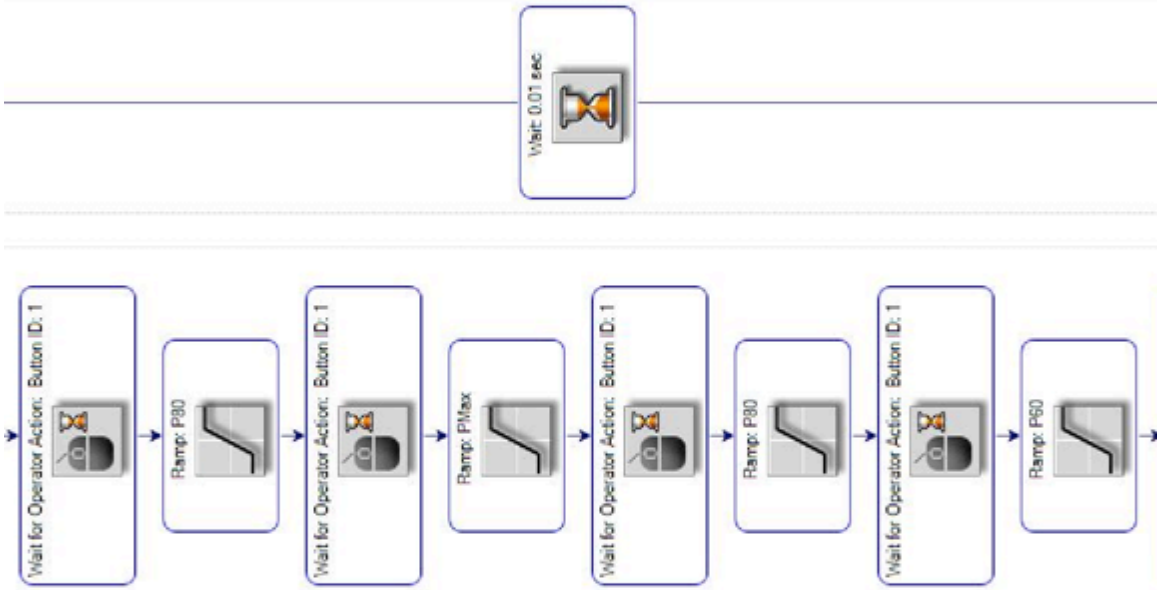
Wait 0.01 sec
Wait for Operator Action: Button ID: 1
Ramp: P80
Wait for Operator Action: Button ID: 1
Ramp: PMax
Wait for Operator Action: Button ID: 1
Ramp: P80
Wait for Operator Action: Button ID: 1
Ramp: P60

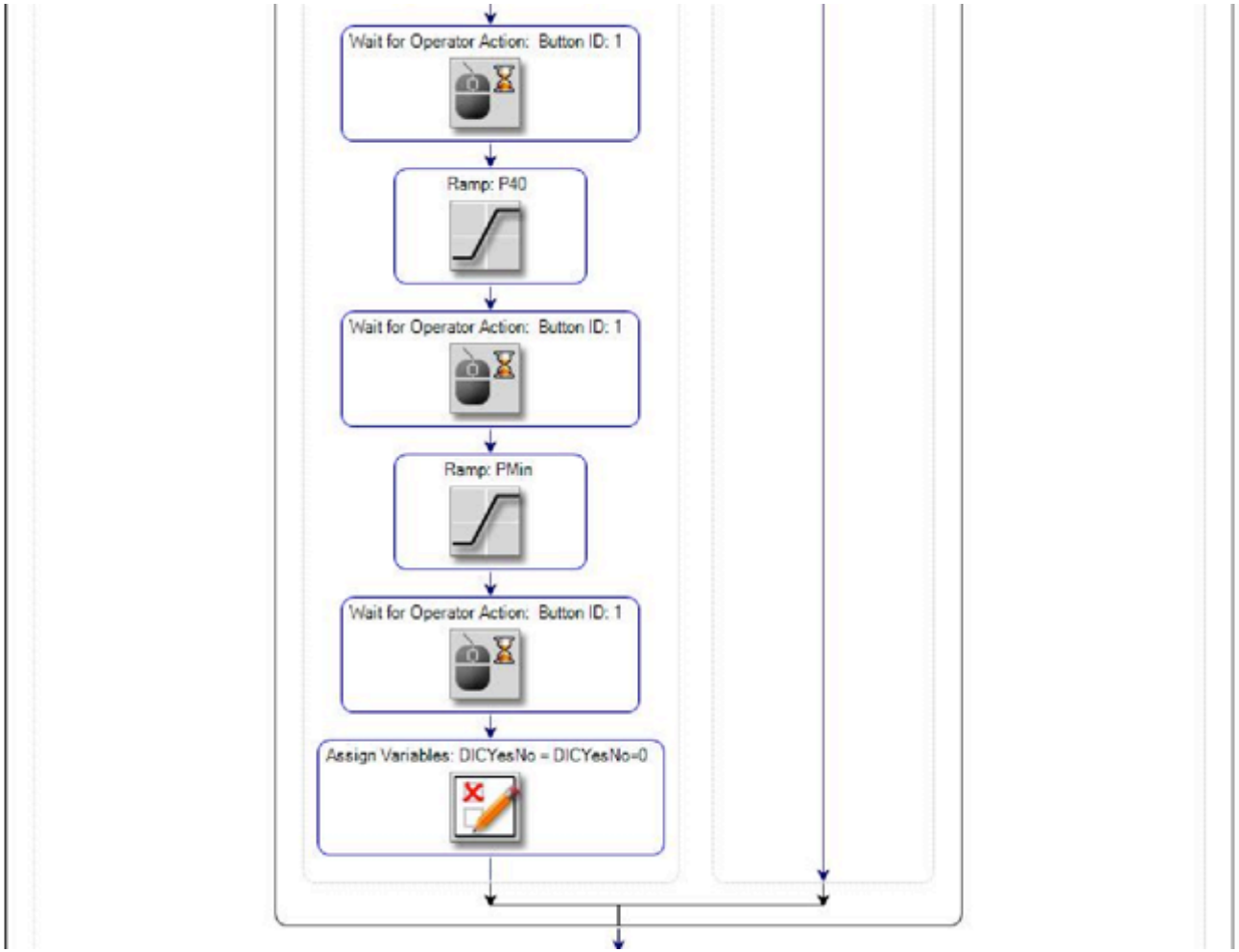
Wait for Operator Action: Button ID: 1
Ramp: P40
Wait for Operator Action: Button ID: 1
Ramp: PMin
Wait for Operator Action: Button ID: 1
Assign Variables: DICYesNo = DICYesNo=0

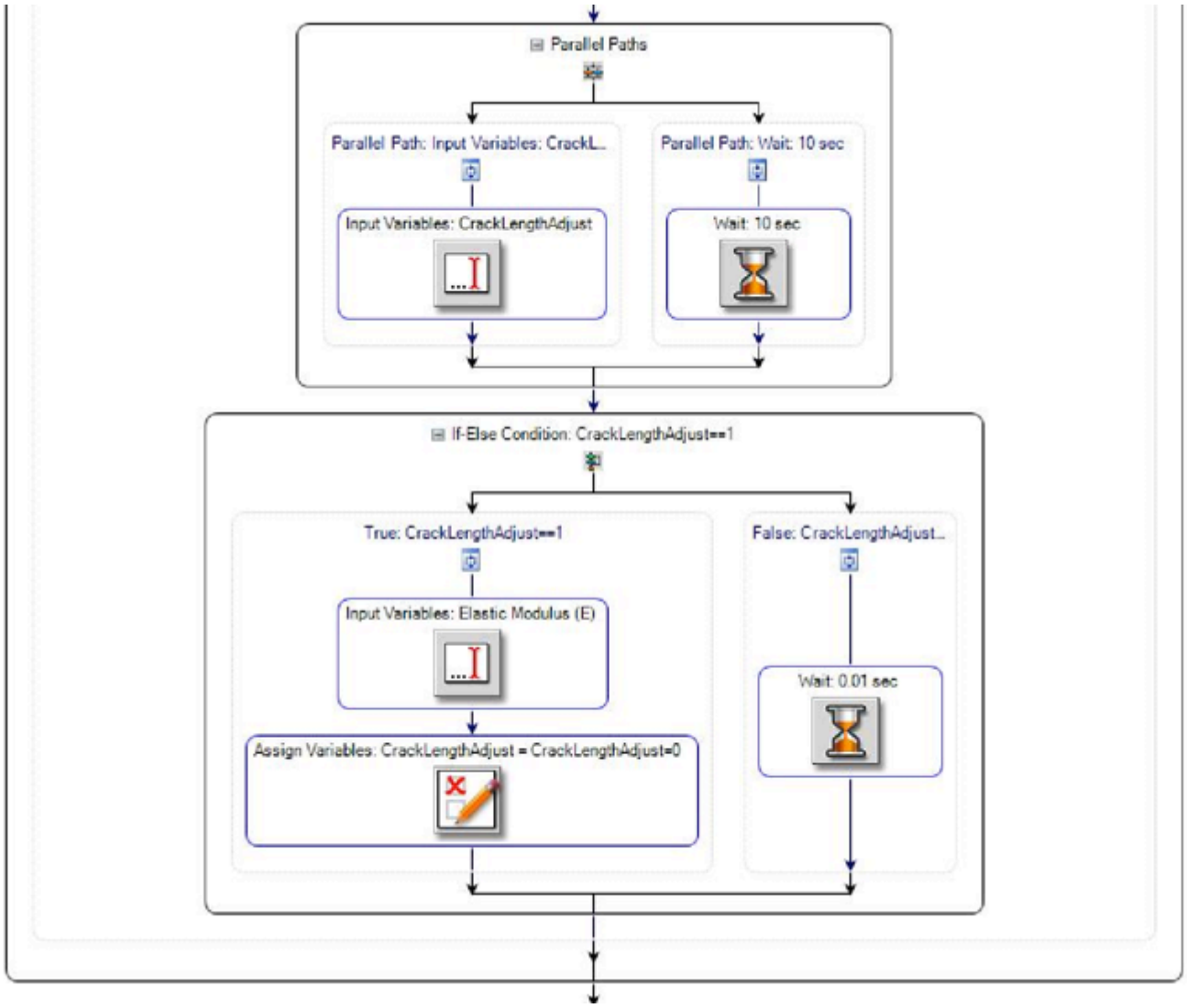
Parallel Paths
Parallel Path: Input Variables: CrackL...
Parallel Path: Wait: 10 sec
Input Variables: CrackLengthAdjust
Wait: 10 sec
If-Else Condition: CrackLengthAdjust==1
True: CrackLengthAdjust==1
False: CrackLengthAdjust...
Input Variables: Elastic Modulus (E)
Wait: 0.01 sec
Assign Variables: CrackLengthAdjust = CrackLengthAdjust=0

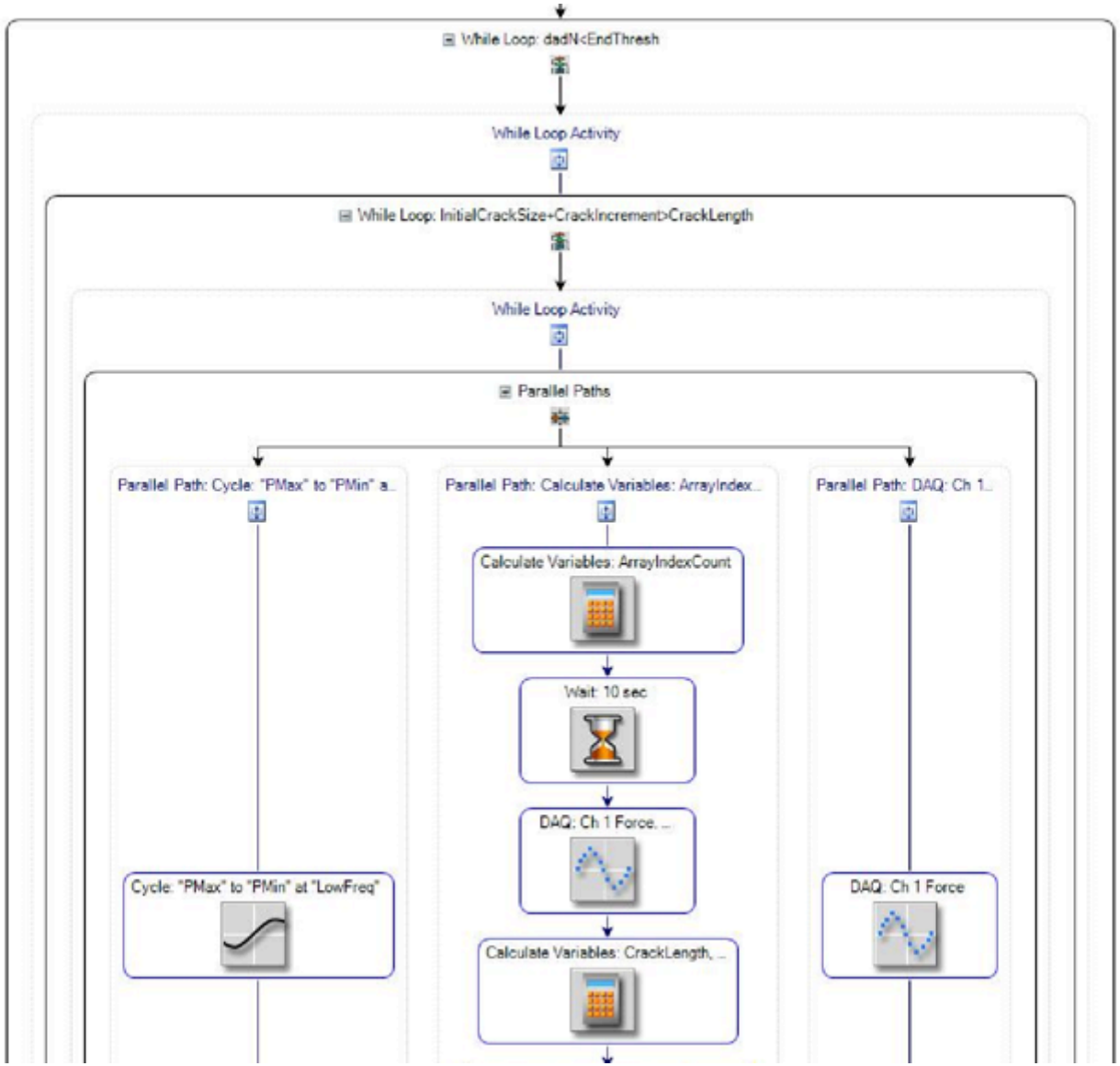
While Loop: dadN<EndThresh
While Loop Activity
While Loop: InitialCrackSize+CrackIncrement>CrackLength
While Loop Activity
Parallel Paths
Parallel Path: Cycle: "PMax" to "PMin" a...
Parallel Path: Calculate Variables: ArrayIndex...
Parallel Path: DAQ: Ch 1...
Calculate Variables: ArrayIndexCount
Wait: 10 sec
DAQ: Ch 1 Force, ...
Cycle: "PMax" to "PMin" at "LowFreq"
Calculate Variables: CrackLength, ...
DAQ: Ch 1 Force

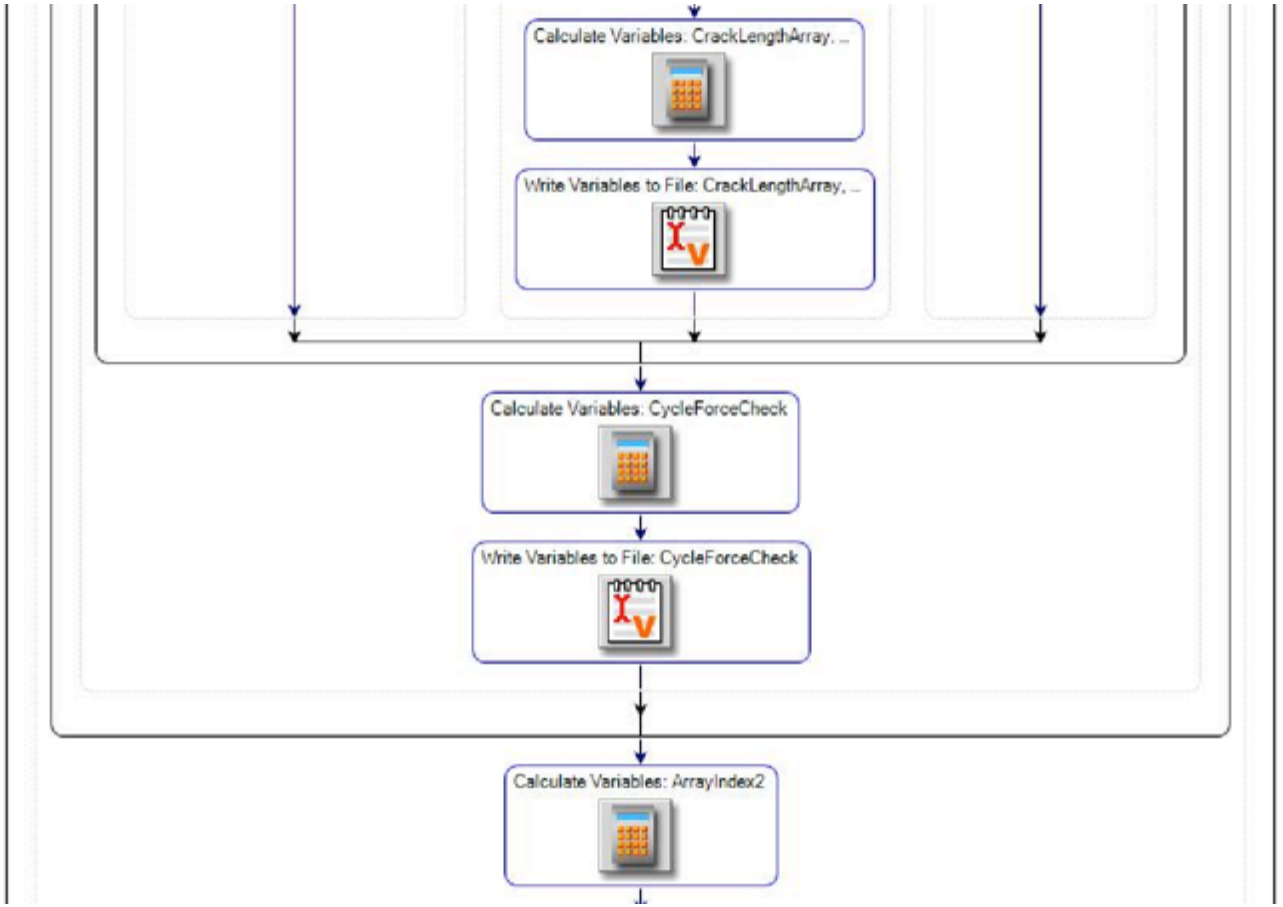
Calculate Variables: CrackLengthArray, ...
Write Variables to File: CrackLengthArray, ...
Calculate Variables: CycleForceCheck
Write Variables to File: CycleForceCheck
Calculate Variables: ArrayIndex2

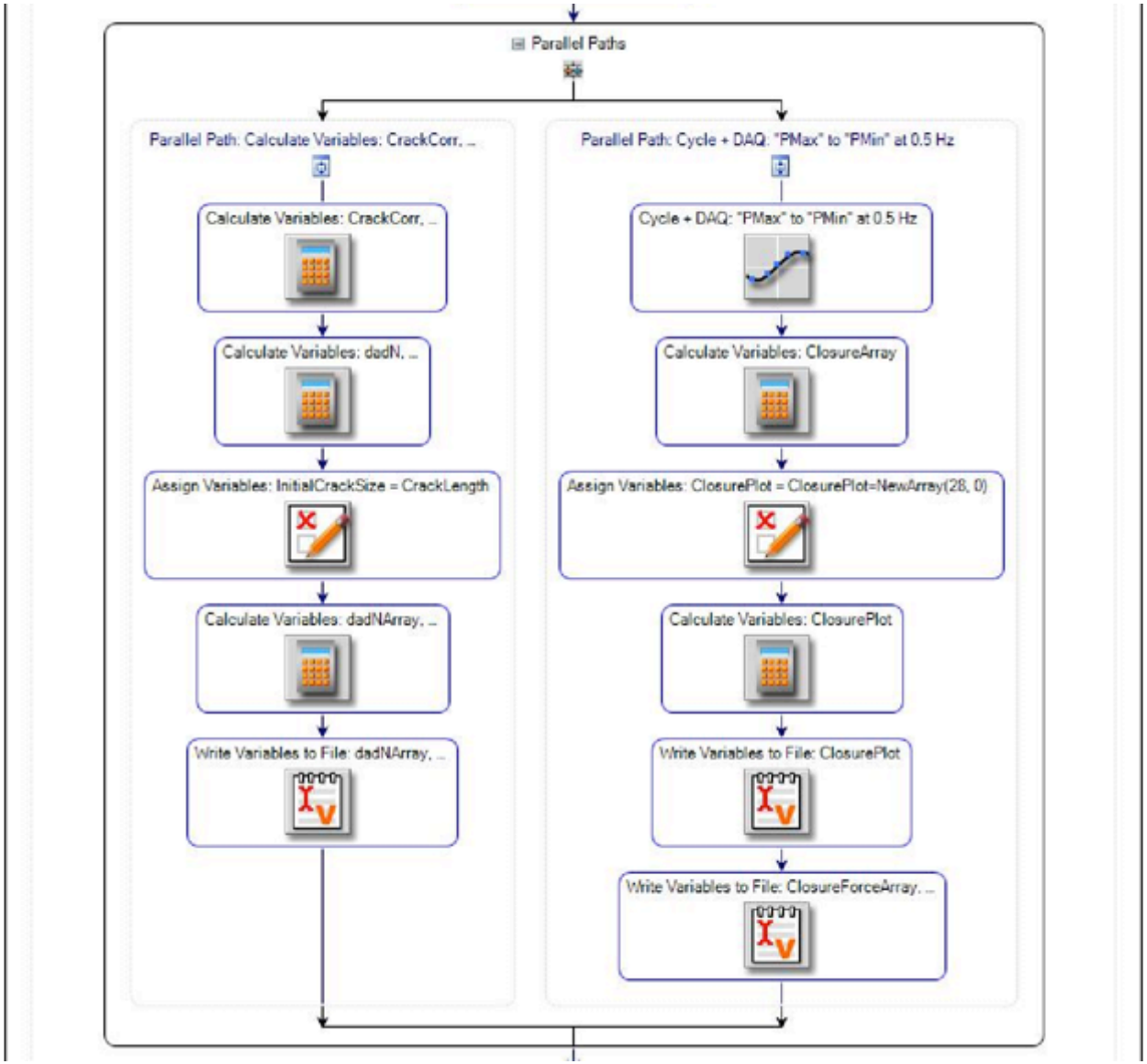
Parallel Paths
Parallel Path: Calculate Variables: CrackCorr, ...
Calculate Variables: CrackCorr, ...
Calculate Variables: dadN, ...
Assign Variables: InitialCrackSize = CrackLength
Calculate Variables: dadNArray, ...
Write Variables to File: dadNArray, ...
Parallel Path: Cycle + DAQ: "PMax" to "PMin" at 0.5 Hz
Cycle + DAQ: "PMax" to "PMin" at 0.5 Hz
Calculate Variables: ClosureArray
Assign Variables: ClosurePlot = ClosurePlot=NewArray(28, 0)
Calculate Variables: ClosurePlot
Write Variables to File: ClosurePlot
Write Variables to File: ClosureForceArray, ...

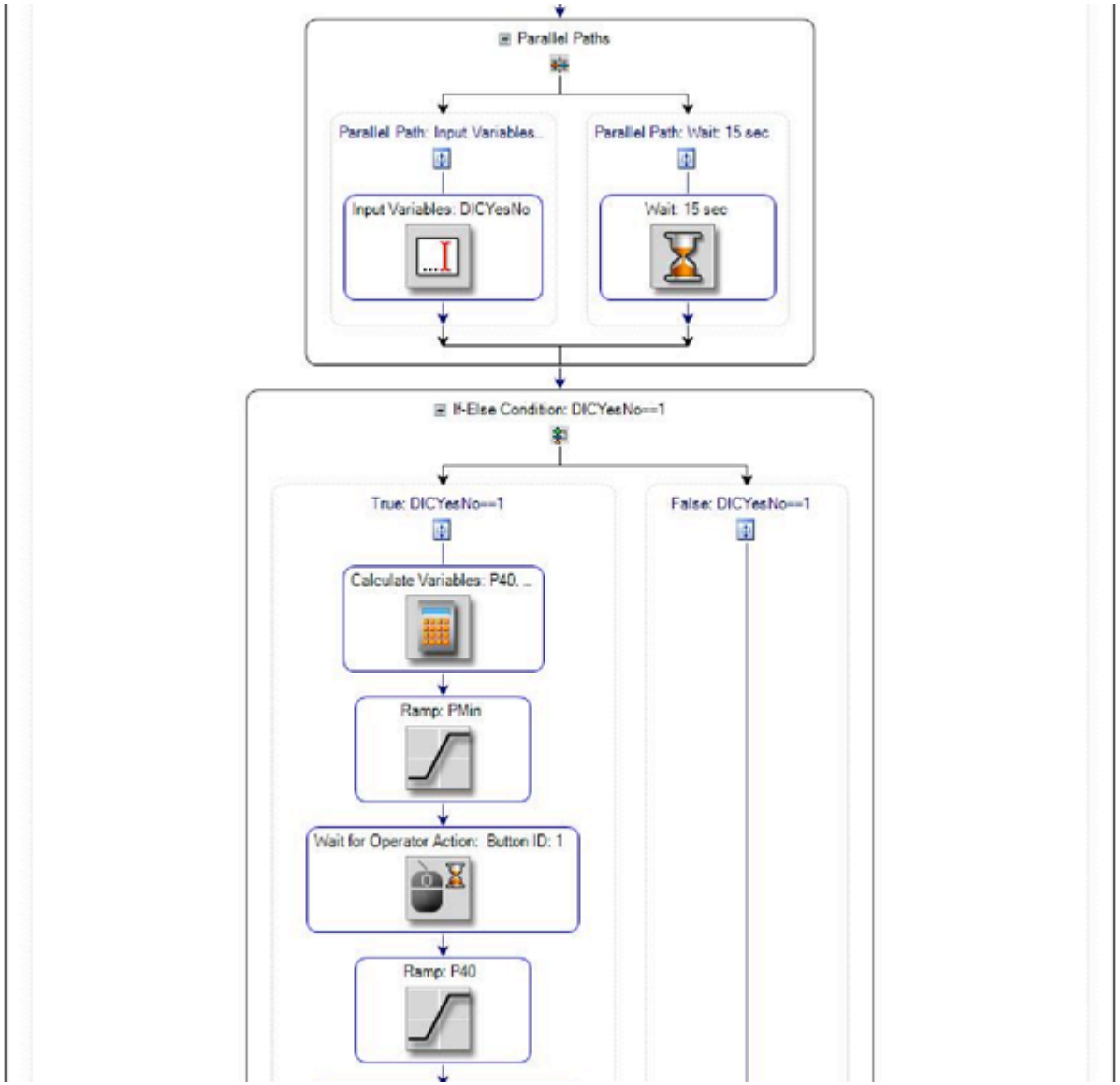
Parallel Paths
Parallel Path: Input Variables...
Parallel Path: Wait: 15 sec
Input Variables: DICYesNo
Wait: 15 sec
If-Else Condition: DICYesNo==1
True: DICYesNo==1
False: DICYesNo==1
Calculate Variables: P40, ...
Ramp: PMin
Wait for Operator Action: Button ID: 1
Ramp: P40

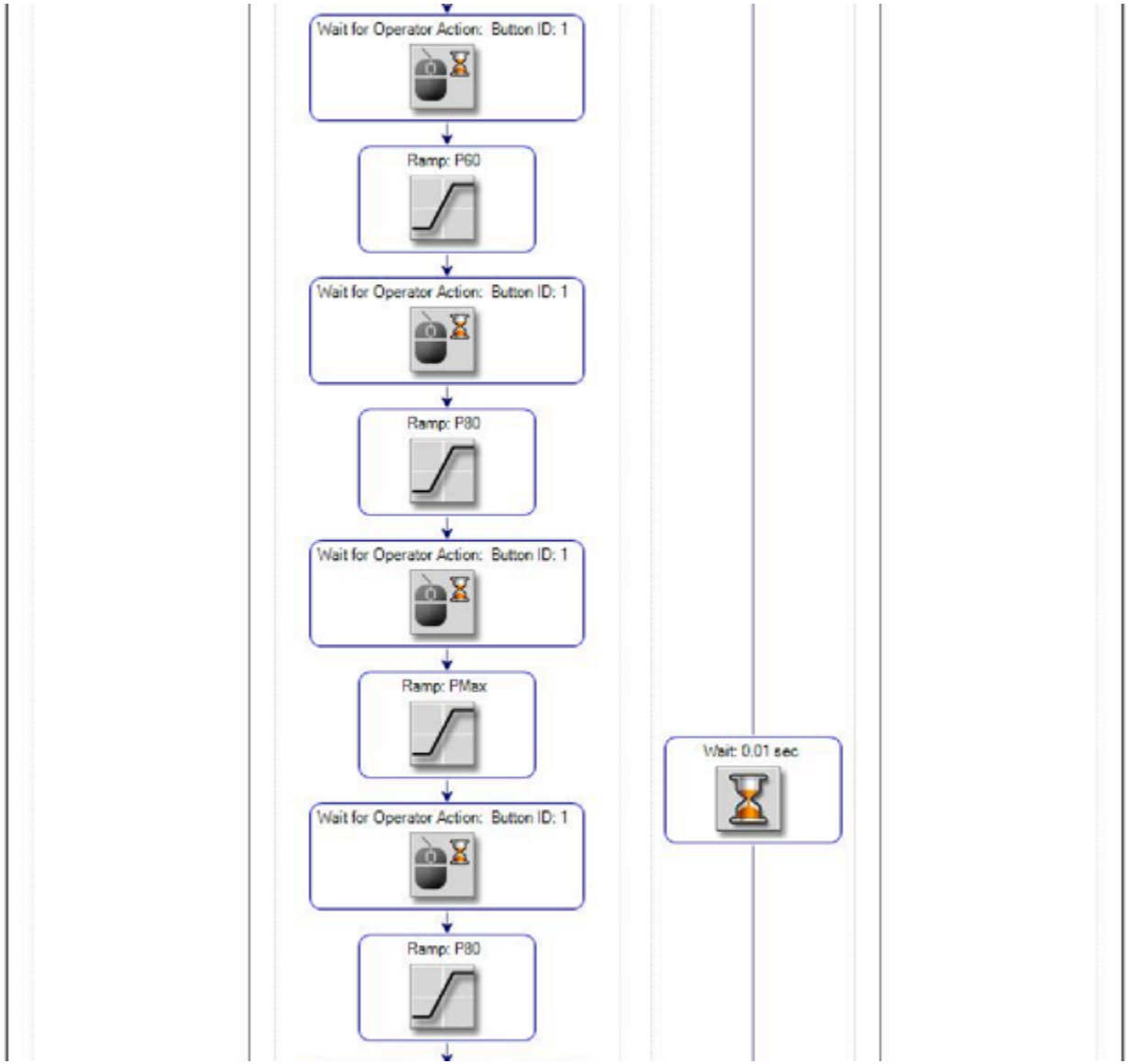
Wait for Operator Action: Button ID: 1
Ramp: P60
Wait for Operator Action: Button ID: 1
Ramp: P80
Wait for Operator Action: Button ID: 1
Ramp: PMax
Wait for Operator Action: Button ID: 1
Ramp: P80
Wait: 0.01 sec

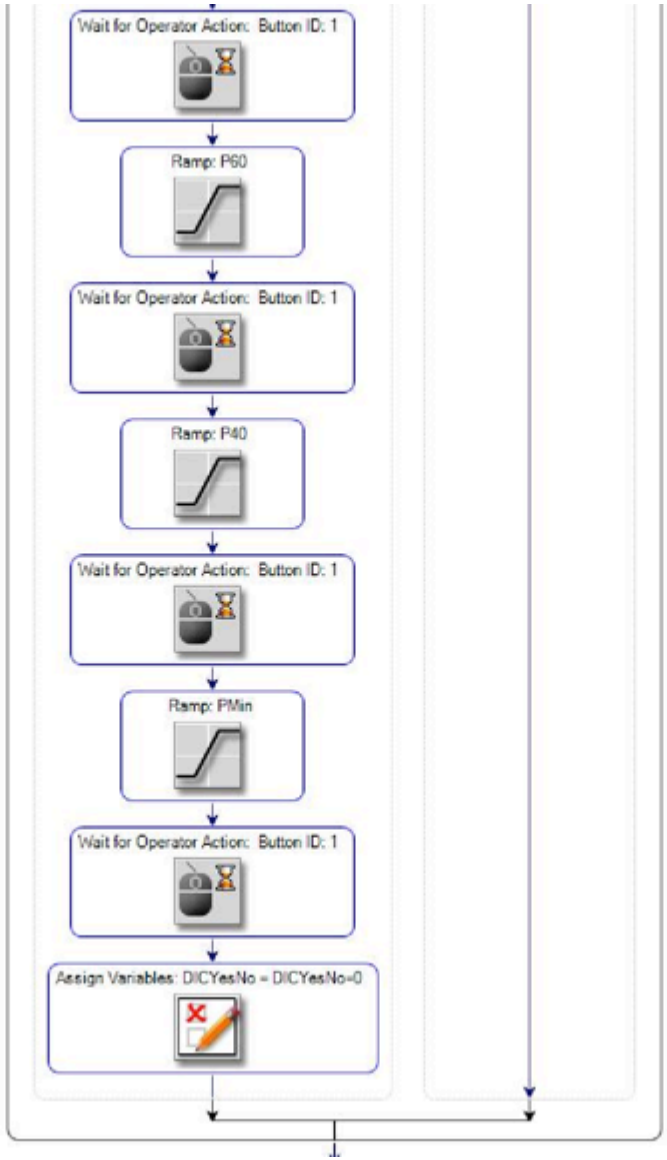
Wait for Operator Action: Button ID: 1
Ramp: P60
Wait for Operator Action: Button ID: 1
Ramp: P40
Wait for Operator Action: Button ID: 1
Ramp: PMin
Wait for Operator Action: Button ID: 1
Assign Variables: DICYesNo = DICYesNo=0

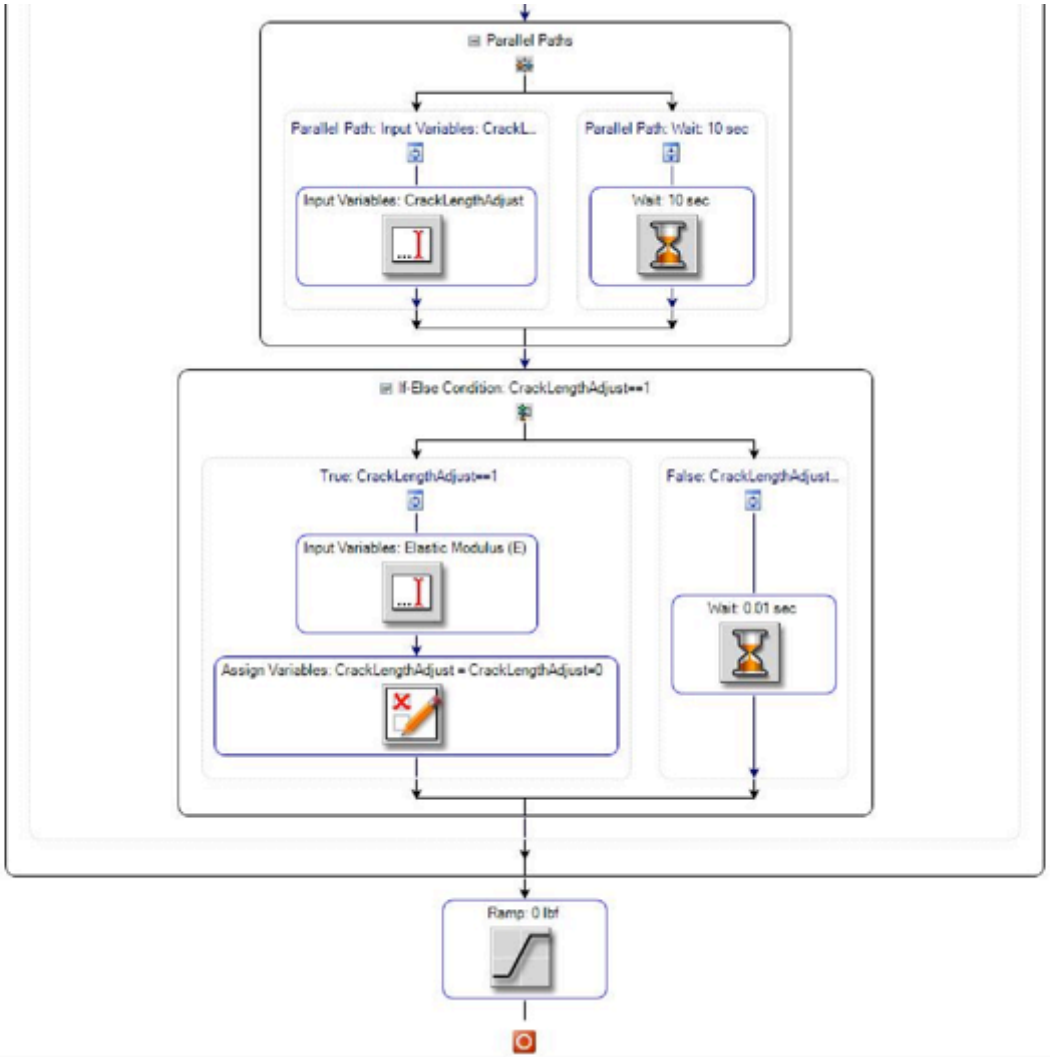
Parallel Paths
Parallel Path: Input Variables: CrackL...
Input Variables: CrackLengthAdjust
Parallel Path: Wait: 10 sec
Wait: 10 sec
If-Else Condition: CrackLengthAdjust==1
True: CrackLengthAdjust==1
Input Variables: Elastic Modulus (E)
Assign Variables: CrackLengthAdjust = CrackLengthAdjust=0
False: CrackLengthAdjust...
Wait: 0.01 sec
Ramp: 0 lbf

Appendix C – Embedded Code Functions

Closure Check – This function performs a quick check to ascertain if closure is above 50% of the maximum load.

```
def ClosureCalcFunc():
    ForceArray=ClosureForceArray.Value.ValueArray
    StrainArray=ClosureStrainArray.Value.ValueArray
    Max = MaxOfArray(ForceArray, 0, ForceArray.Length)
    Index1 = round(0.2*ForceArray.Length)
    Index2 = round(0.3*ForceArray.Length)
    for i in range(0, ForceArray.Length):
        if (ArrayValueAtIndex(ForceArray, i) == Max):
            MaxIndex = i
    Open = LeastSquaresFit(ForceArray, StrainArray, MaxIndex+20, MaxIndex + 180)
    Closure = LeastSquaresFit(ForceArray, StrainArray, Index1, Index2)
    Offset = abs(((Open - Closure)/Open)*100)
    if (Offset<2):
        Check = 1
    else:
        Check = -1
    return Check
```

Clousre Plot Data – This function determines the slopes of the incremental sections of load-strain data and records the opening load. This data is then used to in excel to accurately determine the opening load.

```
#Closure Calculations
def ClosurePlotData():
    FA = ClosureForceArray.Value.ValueArray
    SA = ClosureStrainArray.Value.ValueArray
    for p in range(0,SA.Length):
        SA[p]=SA[p] * -1
    L = FA.Length
    Max = MaxOfArray(FA, 0, L-2)
    Min = MinOfArray(FA, 0, L-2)
    Range = Max-Min
#Find Index of Max Value
    for i in range(0, L-1):
        if (ArrayValueAtIndex(FA, i) == Max):
            MaxIndex = i
            break
#Find Indexes for open condition
    for a in range(MaxIndex, L-1):
```

```
      if FA[a] < Max-(0.95*Range):

         StartIndexOpen = a
         break
   for b in range(MaxIndex, L-1):
      if FA[b] <Max-(0.75*Range):
         EndIndexOpen = b
         break
#Calculate Open Compliance Value
   OpenComp = (LeastSquaresFit(FA, SA, StartIndexOpen, EndIndexOpen))
   ForceOpen = MeanOfArray(FA, StartIndexOpen, EndIndexOpen)
#Calculate Compliance Indexes for Remaining Data
   StartIndexes = NewArray(14,0)
   EndIndexes = NewArray(14,0)
   for x in range(0, StartIndexes.Length):
      for y in range(0, MaxIndex):
         if FA[y] > ((Max-(0.025*Range))-(x*(0.05*Range))):
            StartIndexes[x] = y
            for z in range(0, MaxIndex):
               if FA[z] > (FA[y]-0.1*Range):
                  EndIndexes[x] = z
                  break
            break
#Calculate Compliance and Force Values
   CompData=NewArray(28,0.)
   for m in range(14):
      CheckCalc= (LeastSquaresFit(FA, SA, (EndIndexes[m]), (StartIndexes[m])))
      print CheckCalc
      CompData[m] = ((OpenComp - CheckCalc)/OpenComp)*100
      CompData[m+14] = (MeanOfArray(FA, (EndIndexes[m]), (StartIndexes[m])))/Max
   return CompData
```

Crack Length – This function determines crack length using BFS data.

```
def CrackLengthFunc():
   FA = Ch1ForceArray.Value.ValueArray
   ESET = AuxInput1Array.Value.ValueArray
   FAA = NewArray(0,0.)
   ESETA = NewArray(0,0.)
   for i in range(0, FA.Length):
     if(ArrayValueAtIndex(FA, i) > 0.5*MaxOfArray(FA,0,FA.Length)):
       FAA = AppendArrays(FAA, [ArrayValueAtIndex(FA, i)])
       ESETA = AppendArrays(ESETA, [ArrayValueAtIndex(ESET, i)])
   AS = LeastSquaresFit(ESETA, FAA, 0,
FAA.Length)*Width*Thickness*ElasticModulus*Polar
```

```
    U = 1/((AS**0.5)+1.)
    c = ComplianceCoefC0
    c+= (ComplianceCoefC1*U)
    c+= (ComplianceCoefC2*(U**2.))
    c+= (ComplianceCoefC3*(U**3.))
    c+= (ComplianceCoefC4*(U**4.))
    c+= (ComplianceCoefC5*(U**5.))
    c = c*Width
    return c
```

da/dN – This function calculates da/dN, two variations are included in case there are insufficient data points early in the test.

```
def dadNFunc():
    C = CrackLengthArray.Value.ValueArray
    Cy = TotalCyclesArray.Value.ValueArray
    C1 = CrackCorr.Value.ValueArray
    Cy1 = CountCorr.Value.ValueArray
    if(C1.Length<4):
        dadN = LeastSquaresFit(C, Cy, (C.Length)-50, C.Length-2)
    else:
        dadN = ((C1[C1.Length-2])-(C1[C1.Length-3]))/((Cy1[C1.Length-2])-
(Cy1[C1.Length-3]))
    return 2.*dadN
```

DelK – This function calculates the stress intensity factor range.

```
def DelKFunc():
    CrackL = (CrackLength+InitialCrackSize)/2
    alpha = CrackL/Width
    G = KCalibrationCoef0
    G+= (KCalibrationCoef1*alpha)
    G+= (KCalibrationCoef2*pow(alpha, 2.))
    G+= (KCalibrationCoef3*pow(alpha, 3.))
    G+= (KCalibrationCoef4*pow(alpha, 4.))
    G+= (KCalibrationCoef5*pow(alpha, 5.))
    F = G*(2.+alpha)*(1./(1.*pow((1-alpha), 1.5)))
    KP = F/(Thickness*sqrt(Width))
    dk = KP * (PMax-PMin)
    return dk
```

Force Check – This function works to ensure that force levels are being met throughout the test.

```
def ForceCheckFunc():
    FC = ForceCheckArray.Value.ValueArray
    Average = (PMax + PMin)/2
    Check = MeanOfArray(FC, 0, FC.Length)
    if (0.98*Average < Check < 1.02*Average):
        R = 1
    else:
        R = -1
    return R
```

New Load – This function determines the new max load during a load reduction test.

```
def NewLoadFunc():
    #Need to first determine initial DeltaK
    alpha = InitialCrackSize/Width
    G = KCalibrationCoef0
    G+= (KCalibrationCoef1*alpha)
    G+= (KCalibrationCoef2*(alpha**2.))
    G+= (KCalibrationCoef3*(alpha**3.))
    G+= (KCalibrationCoef4*(alpha**4.))
    G+= (KCalibrationCoef5*(alpha**5.))
    F = G*(2.+alpha)*(1./(1.*pow((1-alpha), 1.5)))
    KP = F/(Thickness*sqrt(Width))
    K = KP * PMax
    NewK=K*exp(CGrad*(CrackLength-InitialCrackSize))
    alpha = CrackLength/Width
    G = KCalibrationCoef0
    G+= (KCalibrationCoef1*alpha)
    G+= (KCalibrationCoef2*(alpha**2.))
    G+= (KCalibrationCoef3*(alpha**3.))
    G+= (KCalibrationCoef4*(alpha**4.))
    G+= (KCalibrationCoef5*(alpha**5.))
    F = G*(2.+alpha)*(1./(1.*pow((1-alpha), 1.5)))
    KP = F/(Thickness*sqrt(Width))
    P = NewK/KP
    if (P>PMax):
        P = PMax
    return P
```

Appendix D – Goal Seeking Function

Data Calculations
1. First insert the currently used elastic modulus in cell B7
2. Perform a goal seek on cell B9 varying cell I7, the crack length sought is what is given by BFS.
3. Perform a goal seel on cell C7 by varying cell C13, the crack length sought is what is measured by DIC.
4. The value given in cell C13 is the new elastic modulus to enter into the program.

Modulus	10250000	A0	1.007	A3	-7.615	U	0.347508735
Width	1.5	A1	-2.171	A4	22.181		
Thickness	0.25	A2	1.537	A5	-20.745	Astar	3.525477559
						Slope	9.17197E-07
Crack	0.505414739						

Modified Modulus	10152656.64
Astar	3.491996406
U	0.348591361
Crack	0.502735529